UNIVERSITY OF GRONINGEN

MASTER THESIS

Chemical trends in Hot Jupiter atmospheres

Author:
M. BRAAM

Supervisor:
Prof. Dr. F.F.S. VAN DER TAK

A thesis submitted in fulfillment of the requirements
for the degree of Master of Science in Astronomy

in the

Interstellar Medium and Star and Planet Formation Group
Kapteyn Astronomical Institute

July 7, 2020

university of
groningen

ii

UNIVERSITY OF GRONINGEN

Abstract

Chemical trends in Hot Jupiter atmospheres

by M. BRAAM

Exoplanetary science has entered the era of comparative characterisation of giant planet atmospheres. Such a characterisation can provide valuable insights into planetary processes and the formation and migration history of planetary systems. We investigate the possible existence of chemical trends in Hot Jupiter atmospheres, by comparatively analysing transmission spectra of 12 planets with coverage from $0.3-4.5\mu$m (HST and Spitzer) and 5 planets with coverage between $1.1-1.7\mu$m (HST WFC3 only). The spectra have been analysed using the Bayesian retrieval framework TauREx II. A statistically significant signature of H_2O is found for 11 of the planets, with at least 2.3σ confidence. Additionally, there are detections of the signatures of VO (2 planets), TiO (2), AlO (2), Na (5), K (5) and particle scattering following Mie theory (3). The first tentative hints towards the signatures of OH were found in WASP-19b, although the similarity with the absorption spectrum of water leaves it inconclusive for now. Furthermore, WASP-39b shows tentative evidence for CrH absorption, whereas the CrH signatures are clearly seen in WASP-31b. The CrH-only model for WASP-31b is $\sim4\sigma$ significant over the flat model and the addition of CrH to a water-only model is significant at $\sim3\sigma$. Retrieved water abundances seem to decrease with equilibrium temperature, contrary to expectations from thermal equilibrium chemistry. These disequilibrium abundances may be (partly) caused by photochemical processes since lower abundances are retrieved for planets receiving higher estimated FUV irradiation. Direct photodissociation is unlikely to have a considerable influence on transmission spectra, but the trend may be due to obscuration by photochemical haze. Another trend that is considered is the dependence of abundances on formation conditions, by determining planetary abundance ratios. Both stellar and substellar ratios are found, indicating different formation histories. Better estimates on the C/O ratio may shed light on this dependence, whereas an improved understanding of clouds/hazes and UV irradiances may further disclose abundance trends with these processes. Especially for the first two improvements, the enhanced wavelength coverage of JWST offers great potential.

Acknowledgements

I would like to thank my supervisor, Floris van der Tak. Your support in the choice of this topic, patience as I tried to fully comprehend the retrieval framework, interest in the results and insights in their implications, all of it has been essential in completing this work. The necessary transition to fully digital meetings about halfway through this work was as smooth and calm as it could have been. I also thank you for the feedback that has greatly enhanced my understanding of the topic and for the opportunity to make use of your scientific network.

In some aspects of this work, obstacles were encountered because of a lack of experience. Regarding this, I am grateful for the input of Michiel Min and Katy Chubb, both from SRON. Your expertise in the topic has been of great value in the progress of this work and my understanding. Besides that, presenting my work in your group has been a rewarding experience. I especially would like to thank Michiel for pinpointing the exact setup of retrievals and Katy for providing opacity data that allowed searching for species that had not yet been discovered in exoplanet atmospheres. I would like to thank Ingo Waldmann and his group at UCL for creating the publicly available TauREx code and for their availability in case of any questions.

I thank Kateryna Frantseva for her willingness to be the second reader of this thesis and also for giving me the opportunity to further develop my educational skills, it was a pleasure to be your tutorial assistant in this year's course on Astrobiology. Furthermore, I want to express gratitude to the Kapteyn Institute, for educating me in such a friendly and inspiring ambiance.

I thank my parents, brother and sister for their unconditional support. During the entire path leading up to this moment, you have always been there for me, both in times of peace and in times of doubt. Without you, this work would not have been possible. Lastly, my dear friends both in- and outside of the Kapteyn Institute I thank for emotional and social support, since sharing a memory or story makes it so much more valuable.

Contents

List of Figures

List of Tables

Chapter 1

Introduction

1.1 Solar System atmospheres

Exoplanetary science is a unique field of astronomy, because of the existence of nearby analogues in the form of the Solar System planets. The first discovery of an extraterrestrial atmosphere was made by Mikhail Lomonosov in 1761 when he reported the discovery of an atmosphere around Venus during its transit of that year (Shiltsev, 2014). The earliest spectroscopic observations were conducted in the first half of the twentieth century and initiated a wide variety of intriguing discoveries: from detecting methane (CH_4) in the atmospheres of the giant planets (Adel et al., 1934) and carbon dioxide (CO_2) on Venus (Adel, 1937) to the discovery of an atmosphere surrounding Titan (Kuiper, 1944), from sulfuric acid (H_2SO_4) clouds on Venus (Young, 1973) to ammonia (NH_3) clouds on Jupiter (Atreya et al., 2005), from hazes on Pluto (Gladstone et al., 2016) to variable levels of CH_4 on Mars (Webster et al., 2018). Finally and perhaps most importantly, there is the exceptional atmosphere of planet Earth and the crucial role it plays in the system as a whole. Despite the variations in their atmospheres, Solar System planets fall into a relatively tight temperature range of $\sim$70K for Neptune up to $\sim$700K for Venus. Besides that, three ranges can be identified for masses and radii: gas giants fall within $100-320 M_\oplus$, $8-11 R_\oplus$; ice giants within $14-17 M_\oplus$, $3.88-4.01 R_\oplus$; and terrestrial planets within $0.06-1 M_\oplus$, $0.38-1 R_\oplus$. An excellent review on Solar System atmospheres can be found in chapter 4 of De Pater et al. (2015).

Based on this understanding of atmospheric physics and chemistry and initiated by the first discovery of an exoplanet orbiting a solar-type star (Mayor et al., 1995), we can start the quest to search for and characterise the wide diversity of planets out there. As of June 2020, the confirmed number of exoplanets has exceeded 4000 and is expected to further increase with current search missions such as TESS (Transiting Exoplanet Survey Satellite). The cumulative number of planets and the most productive detection techniques so far are shown in Figure 1.1 and an excellent review on these (and other) techniques is provided by Fischer et al. (2014). Even more astonishing than the large number of discoveries itself is the wide parameter space in which these planets are being found. Equilibrium temperatures range from $\sim$100 to 4000K and, instead of the three ranges mentioned above for Solar System planets, masses and radii are found continuously within ranges of $0.1-10^{-4} M_\oplus$ and $0.3-25 R_\oplus$[1]. Although planets of all types have been detected in these ranges, it is important to note that an observational bias exists towards detecting large planets on a close-in orbit around their host star, accordingly named Hot Jupiters. The exact definition of a Hot Jupiter used here is a planet of mass $0.1-10^3 M_\oplus$ (Clanton et al., 2014), radius $6-22 R_\oplus$ (Borucki et al., 2011) and an orbital distance $\leq$0.1AU. (Gaudi et al., 2005). The wide ranges in which exoplanets have been detected, combined with the known diversity in Solar System atmospheres, naturally lead to an enormous expected diversity of exoplanet atmospheres.

1.2 Observing exoplanet atmospheres

Several methods are being used to uncover this expected atmospheric diversity and the observations of exoplanet atmospheres can be divided into three categories: Direct imaging

---

[1]Based on data in the NASA Exoplanet Archive.
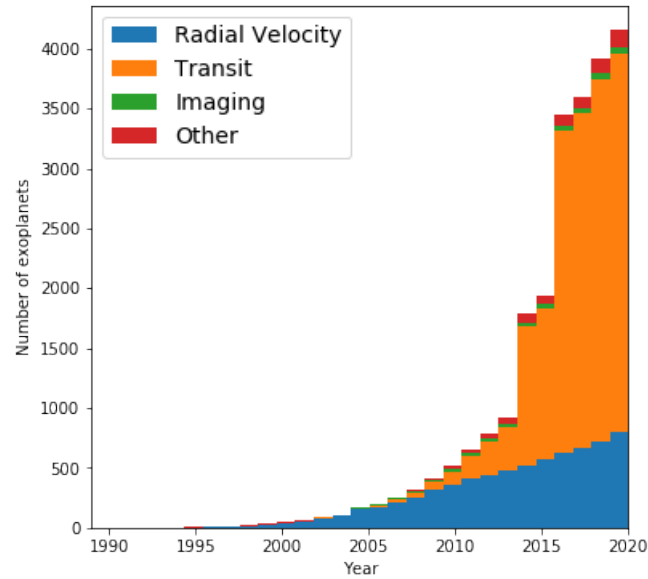
FIGURE 1.1: The cumulative number of confirmed exoplanets, with the color relating to different detection methods[2].

spectroscopy, High-resolution Doppler Spectroscopy and Transit spectroscopy (Crossfield, 2015).

Direct imaging means that an exoplanet is spatially resolved from its host star, using a coronagraph to block out the stellar light. This challenging endeavour is most feasible for planets on orbits far away from their host star. The limiting factor is the adjacent host star: the Sun is for example 10^6 to 10^9 times brighter than the Earth in the near-infrared and the optical respectively (Seager et al., 2010). This extreme flux contrast together with the limited occurrence of planets at far-out orbits results in an as of yet small number of observations with this method. However, spatially resolving a planet can provide high-quality spectra and next-generation facilities such as the Extremely Large Telescope (ELT) will lead to higher sensitivity as well as the ability to observe smaller planets orbiting closer to their host star (Quanz et al., 2015; Snellen et al., 2015).

High-resolution Doppler spectroscopy infers the Doppler motion of a planet through its spectral lines by high-resolution spectroscopy ($\lambda/\Delta\lambda\sim10^5$) of the star-planet system. During an observation, the stellar and telluric lines are relatively stable while the planetary spectral lines undergo strong Doppler shifts. After removing the stellar and telluric lines, the expected molecules and their spectroscopic signatures in template planetary spectra are used for cross-correlation to find the exact absorption lines.

Transit spectroscopy works best for large planets that orbit very close to their host star, since the probability of a transit $p\approx R_*/a$, where a is the planet's orbital radius. A spectroscopic transit measurement involves observing the combined light of the planet and star and this can be done in three distinct geometries, as shown in Figure 1.2. When the planet moves in front of its host star (the primary transit), the stellar light transverses the planetary day-night terminator region along the line of sight. This causes extinction of the stellar light and observations in this way are called transmission spectra. The secondary eclipse spectra can be observed because the planet moves behind its host star. Subtracting the star's spectrum from the combined star and planet spectrum provides us with a measure of the planet's thermal radiation and reflected light, or its dayside emission spectrum. Thirdly, a phase curve can be observed in between the other two geometries, providing a planetary spectrum at different phases throughout its orbit. By measuring brightness temperature maps, phase curves can teach us about atmospheric dynamics (see Heng et al. (2015) for an overview). So far, atmospheres have been observed most effectively by means of transmission spectra.

---

[2]Based on data in the NASA Exoplanet Archive.

Moreover, this geometry is particularly sensitive to the presence of chemical species and, hence, our study involves the analysis of transmission spectra.
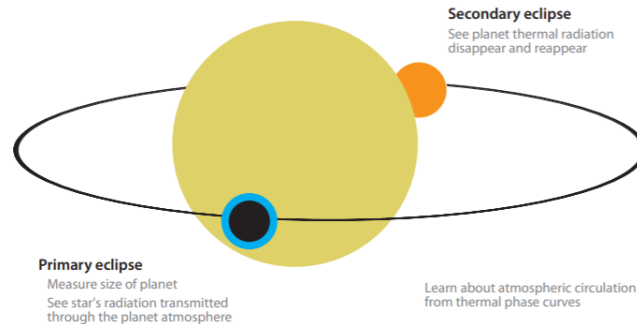
FIGURE 1.2: Illustration of the different orientations suitable for transit spectroscopy. Image taken from Seager et al. (2010).

1.2.1 Transmission spectra

As shown by the cyan annulus in Figure 1.2, part of the stellar light transverses the annulus of the planet's atmosphere at the day-night terminator regions when we observe a primary transit. This can be observed as a transit depth or a dip in the light from the host star that is received by us. The transit depth is equal to the flux that is intercepted and it can be described by:

$$\frac{\Delta F(\lambda)}{F} \simeq \left(\frac{R_{pl}(\lambda)}{R_*}\right)^2 \tag{1.1}$$

Where $\Delta F(\lambda)$ is the flux deficit as a function of wavelength, compared to the total flux F. R_{pl} and R_* denote the planetary and stellar radius respectively. This flux deficit would be $\sim 10^{-4}$ for Earth orbiting the Sun and increase to $1-2\%$ for a typical Hot Jupiter.

If the planet has an atmosphere, the opacity changes with wavelength (Seager et al., 2000). The cause of this change can be found in molecular and atomic spectroscopy, from which we know that a particular chemical species absorbs light more strongly at specific wavelengths. The presence of a particular chemical species in a planetary atmosphere can thus cause a significantly higher absorption of light at certain wavelengths, as is illustrated in Figure 1.3 for the penetration of solar light in Earth's atmosphere. It can be seen that ozone absorbs most of the incoming UV light and water has some strong absorption signatures in the near-infrared, such as around wavelengths of 1.4μm. In a primary transit geometry, this wavelength-dependent absorption increases the apparent radius of a planet and, consequently, increases the transit depth at that wavelength. Observing the transit depth at multiple wavelengths leads to a transmission spectrum and provides us with an opportunity to infer the presence of atoms, molecules or condensates in an atmosphere.

Going back to Figure 1.2, it can be seen that the geometry of a primary transit results in probing the atmosphere transversely along the line-of-sight and this is integrated over the annular area. This means that, compared to probing the atmosphere radially, we have a larger relevant optical depth. This naturally leads to more sensitivity to trace chemical species. Moreover, transmission spectra can be used to probe the opacities caused by scattering and absorption of light by small particles in the atmosphere. This is described by Mie theory for a spherical particle and can be approximated by Rayleigh scattering when the particles are much smaller than the wavelength of the light. The presence of opaque high altitude clouds can mute spectral features and can lead to a flat transmission spectrum (Seager et al., 2000). However, what we probe through this configuration are the morning as well as evening terminator regions. Therefore, transmission spectra do not probe the planet's day- or night-side directly, while differences in temperature, composition and scale height between or inside both terminator regions might complicate the interpretation of observations (e.g. Pluriel et al., 2020).
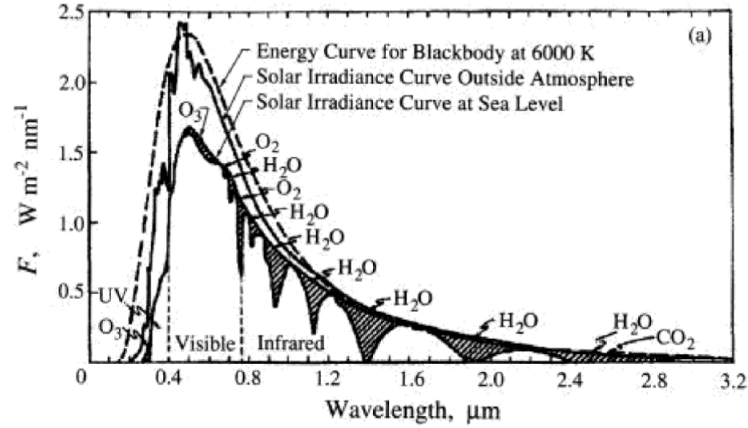
FIGURE 1.3: The solar irradiance that is received by Earth. The dashed curve represents a blackbody at 6000K, which agrees well with the solar irradiation curve on top of the atmosphere. From the solar irradiance curve at sea level, it can be seen that a significant fraction is absorbed by the atmospheric constituents: the relevant absorber for each of the shaded regions is indicated. Image taken from Seinfeld et al. (1998).

1.2.2 Hot Jupiters

Besides the geometrical preference for large planets orbiting close to their host star, the choice to look for trends in Hot Jupiter atmospheres is motivated by the relative accessibility of their transmission spectra (Sing, 2018). The characteristic length scale of a planetary atmosphere is the scale height H:

$$H = \frac{k_B T}{\mu_m g_p} \tag{1.2}$$

Where k_B denotes Boltzmann's constant, T the atmospheric temperature, μ_m is the mean molecular weight and g_p is the surface gravity of the planet. The absorption signal δ of corresponding to an annular area of $1H$ during the transit can be calculated by:

$$\delta = \frac{(R_{pl} + H)^2}{R_*^2} - \left(\frac{R_{pl}}{R_*}\right)^2 \tag{1.3}$$

Under the assumption that $H << R_{pl}$:

$$\delta \approx \frac{2R_p H}{R_*^2} \tag{1.4}$$

As seen from Formula 1.4, the planetary absorption signal is proportional to H and therefore it is easier to probe the atmospheres of hot planets with low molecular weight and/or low gravity. The area of the atmosphere in a primary transit can be approximated as an annulus extending radially for $\simeq 5H$ (Seager et al., 2009). Following their definition in Section 1.1, this is another reason why Hot Jupiters are good for characterisation: their close-in orbits provide high temperatures, their atmospheres are dominated by light species (H, He) and their gravity is relatively small compared to denser, rocky exoplanets.

1.3 Atmospheric characterisation

At a time when only around 90 exoplanets were confirmed, the first detection of an exoplanet atmosphere was the discovery of the sodium doublet during a transit of the Hot Jupiter HD

209458b (Charbonneau et al., 2002). It was made using STIS[3] on the Hubble Space Telescope (HST), like other detections such as Rayleigh scattering in HD 189733b (Lecavelier Des Etangs et al., 2008a) and titanium oxide (TiO) in HD 209458b (Désert et al., 2008). These transit measurements in the optical and ultraviolet (UV) were complemented by Spitzer measurements in the infrared (IR) (e.g. Deming et al., 2006). Furthermore, the commissioning of WFC3[4] at HST enabled the near-infrared (NIR) detection of water signatures in a number of planets (e.g. Deming et al., 2013, Kreidberg et al., 2014). This has led all the way to the recent spectroscopic evidence of water in a Super-Earth (Tsiaras et al., 2019). Although the majority of detections from transmission spectroscopy involve water or one of the alkali metals sodium (Na) and potassium (K), detections of a wide range of chemical species in an exoplanet atmosphere have been reported. These include H_2O, CH_4, CO, CO_2, HCN, TiO, Na and K: an extensive overview of all chemical detections that were made as of 2019 is given by Madhusudhan (2019). While atmospheres have been detected around nearly 100 exoplanets, the high-precision spectra needed to derive robust inferences on atmospheric properties have been observed for a few tens of giant exoplanets.

The ability to infer statistical constraints on atmospheric properties was greatly improved by the introduction of retrieval methods (e.g. Irwin et al., 2008, Madhusudhan et al., 2009, Waldmann et al., 2015). Retrievals are based on a so-called Forward Model, which generates a planetary spectrum based on a combination of underlying parameters. The retrieval (or inverse) method aims to determine the best-fit parameters from the observed spectrum and hence is based on the Forward Model. A more in-depth explanation of this method is provided in Section 2.2. The combination of observations, theoretical modelling and retrieval techniques has enabled constraints on many key atmospheric properties such as chemical abundances, temperature profiles, clouds and/or hazes, circulation patterns and exospheres (Madhusudhan, 2019).

Furthermore, instead of focusing on individual planets, retrieval methods have enabled us to conduct comparative analyses of samples of exoplanets (e.g. Sing et al., 2016, Barstow et al., 2017, Tsiaras et al., 2018, Fisher et al., 2018, Welbanks et al., 2019). To conduct a comparative analysis it is essential to constrain the atmospheric properties in a homogeneous procedure: thus, both in the data analysis as well as in the atmospheric modelling (Tsiaras et al., 2018). Homogeneously constraining the atmospheric properties of several planets, may offer us an opportunity to relate these properties to initial conditions and/or planetary parameters.

Besides space-based telescopes, transit spectroscopy with ground-based facilities has led to the detection of thermal emission of exoplanets as well as spectroscopic signatures of TiO, Na and K. Around ten atmospheres have now been observed through direct imaging and detections of H_2O, CH_4, CO and NH_3 have been reported. High-resolution Doppler spectroscopy has been used to constrain temperature profiles and atmospheric wind speeds as well as to detect signatures of Hot Jupiter constituents such as CO, H_2O, TiO, HCN. However, transit spectroscopy is currently the best method to infer quantitative constraints on, for example, chemical abundances (Madhusudhan, 2019).

1.4 Physics and chemistry of exoplanet atmospheres

1.4.1 Atmospheric processes

The state of an atmosphere strongly depends on macroscopic parameters such as the stellar irradiation, the planet's gravity and the elemental abundances. A distinction between atmospheres can be made based on their chemical composition. Primary atmospheres result from direct accretion from the protoplanetary disk and consist mainly of H_2 and He. The atmospheres of the giant planets in the Solar System are examples of these primary atmospheres. The Solar System terrestrial planets lost this initial inventory of light H_2 and He and instead formed secondary atmospheres through the outgassing of volatiles from their interior and

---

[3]Space Telescope Imaging Spectrograph
[4]Wide Field Camera 3
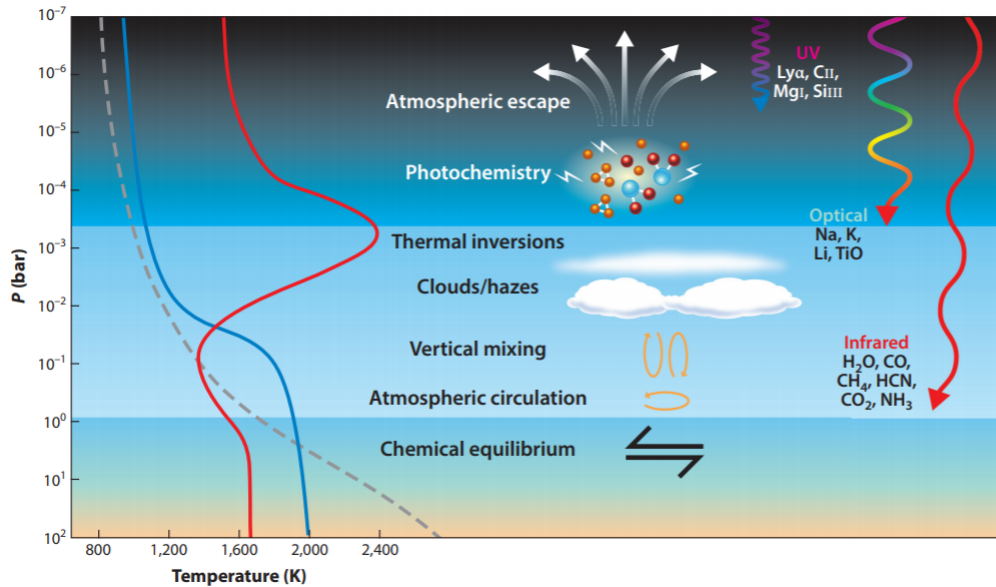
FIGURE 1.4: As a function of pressure (and thus altitude), the different pro-
cesses active in a planetary atmosphere are indicated at the approximately
relevant location. The depths that are probed using different parts of the
electromagnetic spectrum are shown on the right together with some chem-
ical species having signatures in the respective spectral regions. The lines
on the left show examples of temperature-pressure profiles: note that the red
profile contains a thermal inversion. Figure taken from Madhusudhan (2019).

delivery by minor bodies. Therefore, the atmospheres of Earth, Mars and Venus are domi-
nated by heavier species such as N_2, O_2 and CO_2. The atmosphere of Titan is another Solar
System example of a secondary atmosphere and also contains a significant fraction of CH_4.

Figure 1.4 shows that atmospheric compositions are controlled by a complex interplay
between several physical and chemical processes. In the lower atmospheric layers of high
temperature and pressure, a composition can be assumed to be in thermochemical equilib-
rium: an atmosphere is sufficiently hot and dense such that chemical reactions occur faster
than other processes (such as kinetics or photochemistry) and, independent of location, the
composition is determined only by the bulk elemental composition, the pressure and the
temperature. The expected atomic and molecular abundances are predicted for solar initial
elemental composition by equilibrium chemistry models such as GGChem (Woitke et al.,
2018).

As seen in Figure 1.4, chemical equilibrium can be expected in the lower regions of a
planetary atmosphere. Moreover, for the hottest exoplanets (T>2000K), thermochemical
equilibrium is a valid assumption for the visible and infrared photosphere (Moses, 2014).
For T≤2000K and in the upper atmospheric layers of the hottest planets, disequilibrium
chemical processes can significantly influence atmospheric properties and this is also ob-
served in most of the Solar System planets. The upper regions of planetary atmospheres
receive high UV fluxes and have low densities, which leads to disequilibrium caused by
photochemistry. An example of such a disequilibrium is the production of ozone in Earth's
upper atmosphere via the Chapman mechanism (Chapman, 1930). Even higher up, another
driver to disequilibrium of (exo)planet atmospheres is atmospheric escape (Owen, 2019). In
the intermediate regions, the composition is dominated by dynamical processes. Examples
in Hot Jupiters are vertical mixing (Cooper et al., 2006) and the strong equatorial jets that
are caused by the huge temperature difference between the day- and nightside (e.g. Knut-
son et al. (2007), Showman et al. (2011). This huge temperature gradient is caused by the
expected tidal locking of Hot Jupiters: at orbital distances ≤0.1AU the planets are expected
to face their host star with the same hemisphere at all times (Guillot et al., 1996). The result-
ing strong horizontal winds can transport parcels of gas from the dayside to the nightside

(Steinrueck et al., 2019). Vertical mixing can transport a parcel of gas to another atmospheric layer. In both cases, the transport quenches or enhances the abundance of a particular constituent when this mixing is faster than the chemical reaction timescale (Moses, 2014). As an example, the high tropospheric CO abundance in Jupiter is explained by vertical mixing from deeper (and thus hotter) layers of the atmosphere (Prinn et al., 1977).

The existence of aerosols, which are particles suspended in a gas, is also a common feature of atmospheres and can strongly influence atmospheric processes and observed spectra. Clouds and hazes both consist of aerosols and they absorb and scatter light differently than gases. Clouds are created by the condensation of atmospheric gases, forming liquid droplets and/or solid particles suspended in an atmosphere. As mentioned in Section 1.1, clouds in the Solar System are usually made up of volatile species such as H_2O, CO_2 and NH_3. The high temperatures of exoplanets allow for a wide range of more refractory condensates, examples include metal oxides such as MgO[s] and FeO[s]; silicates such as $MgSiO_3$ and Mg_2SiO_4; and high-temperature condensates such as TiO_2[s] and Al_2O_3 (Helling, 2019). Hazes are involatile solid particles that are produced by chemical pathways in the atmosphere. An example of such a pathway is the photolysis of CH_4 producing hydrocarbon hazes (Kawashima et al., 2019). Therefore, the formation of hazes is a one-way trip, whereas clouds can move through cycles of condensation and evaporation.

Lastly, Figure 1.4 shows some examples of possible temperature-pressure profiles in Hot Jupiter atmospheres. Such profiles are a result of the incoming radiation and the interplay with chemistry and dynamics and thermal emission spectra can provide a window into these profiles. The red profile shows a thermal inversion, which is an increase of the temperature with altitude and is a common feature of Solar System atmospheres. Evidence for an inversion was found in WASP-121b, with UV/optical absorption by TiO/VO proposed as the possible cause (Evans et al., 2017).

1.4.2 Chemical abundances

In addition to the chemical detections mentioned earlier, a limited amount of exoplanets have robust constraints on the exact abundances or Volume Mixing Ratios (VMR) of detected species. These measurements are possible from transit spectroscopy via both transmission and emission spectra as well as thermal emission spectra from direct imaging (Madhusudhan, 2019). As described in Section 1.2.1, the geometry associated with transmission spectra further enhance their sensitivity to chemical abundances. To remove degeneracies between retrieved abundances and clouds, coverage from UV to NIR is needed (e.g. Griffith, 2014; Heng et al., 2017). The majority of retrieved abundances concern H_2O in Hot Jupiters and have been derived using the coverage offered by WFC3 (Fisher et al., 2018; Tsiaras et al., 2018) or the combination of STIS, WFC3 and Spitzer's IRAC (e.g. Barstow et al., 2017; Madhusudhan et al., 2014; Pinhas et al., 2019; Welbanks et al., 2019). These retrievals generally hint towards substellar abundances, which might have important implications.

As said, photochemistry is expected to strongly influence exoplanet atmospheres, and the close-in orbit of Hot Jupiters exposes them to high (UV) irradiation from the host star (Line et al., 2010; Moses et al., 2011). A substellar H_2O abundance might result from its UV photodissociation into the hydroxyl radical (OH):

$$H_2O + h\nu \longrightarrow OH + H$$
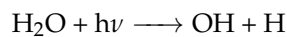
This photodissociation is not particularly prominent on Earth, because most of the radiation in this regime is absorbed by higher atmospheric layers due to the presence of molecular oxygen and ozone (Liou, 2002). On Jupiter, water is not abundant in the upper atmospheric layers due to its low temperatures. In contrast, Hot Jupiters are expected to have water vapour existent high up in the atmosphere, which could lead to significant contributions of this photodissociative process. However, in an H_2-dominated atmosphere, the resulting species are expected to quickly recycle back into H_2O (Moses, 2014), possibly decreasing the effectiveness of photodissociation.

Another possible cause for disequilibrium chemistry can be transport-induced quenching due to vertical mixing (Cooper et al., 2006; Moses, 2014) and/or strong equatorial winds leading to cold traps, depleting species via condensation and gravitational settling on the

much colder night sides of Hot Jupiters (Parmentier et al., 2013). At the temperatures of Hot Jupiters, these cold traps are most likely responsible for the depletion of refractory species such as TiO and VO (vanadium oxide).

Clouds and/or hazes can influence the retrieved abundances by muting the strength of spectral features (Deming et al., 2013; Sing et al., 2013). The resulting subdued features might imply lower retrieved abundances. Sing et al. (2016) detect clouds but find no evidence for H_2O depletion, while other studies report substellar H_2O abundances accompanied by varying levels of clouds (Barstow et al., 2017; Pinhas et al., 2019).

1.4.3   Initial conditions

Besides these physical and chemical processes, an important factor in determining atmospheric compositions is the elemental composition from which an atmosphere results. Since Hot Jupiters have primary atmospheres the final compositions may contain clues about the accretion history (Madhusudhan, 2012). Under the assumption that the protoplanetary disk and the star formed from the same protostellar cloud, it can then be inferred that they had the same initial elemental composition. Subsequently, the thermodynamic evolution of the protoplanetary disk determines the locations of the various snow lines, where volatile species condense out to form ice grains in the order H_2O ($\sim$135K) - CO_2 ($\sim$47K) - CH_4 ($\sim$30K) - CO ($\sim$20K) (Öberg et al., 2011). The chemical compositions of the gas and solids in a protoplanetary disk thus evolve as a function of time as well as location relative to the snow lines. For example, in between the snowlines of H_2O and CO (carbon monoxide), most oxygen is present in solids, while most carbon remains in CO gas (Öberg et al., 2011), leading to a high $(C/O)_{gas} \sim 1$ as compared to the solar C/O=0.54. This implies that, following the core accretion scenario of planet formation (Pollack et al., 1996), a wide range of planetary C/O ratios and overall Z/H abundance ratios are possible, depending on the formation location and the relative accretion of gas versus solids. A possible explanation for the H_2O underabundance and alkali enrichment that is found by Welbanks et al. (2019) is the accretion of primarily high C/O gas beyond the CO_2 snow line.

1.5   Aims

Keeping in mind the complex interplay between processes determining the atmospheric state, this thesis investigates the following question: *what chemical trends can be found in Hot Jupiter atmospheres and how can these be explained?*

Based on the knowledge that can be gained from transmission spectra, three possible directions were put forward. Firstly, a possible thermochemical trend can be investigated by the dependence of chemical abundances on atmospheric temperature. Although a trend is not necessarily expected, the comparison between retrieved abundances and those predicted by equilibrium chemistry calculations can offer many insights, as introduced in Section 1.4.1. A second possibility for a trend is the dependence of chemical abundances on the host star irradiation, because a photochemical trend may be caused by UV irradiation in particular. Finally, abundances may be strongly influenced by the initial elemental compositions. Relating planetary to stellar abundance ratios may show some of this dependence on formation and accretion history.

In quantifying the possible influence of any of these processes, we need to have a representative sample of Hot Jupiters and their atmospheric properties. Hence, the first step is to homogeneously analyse a sample of exoplanet transmission spectra. The spectra have been analysed using the Bayesian retrieval framework TauRex II (Waldmann et al., 2015). The sample and the retrieval framework are described in Chapter 2, followed by the general setup for this investigation. The results of the retrievals will be presented in Chapter 3, by first illustrating the general procedure in detail for a single planet (WASP-39b). Afterwards, some peculiar retrieval results are shown and the results for the full sample are described. Chapter 4 provides a comparison with earlier retrieval results as well as theoretical predictions and discusses the importance of the processes influencing the atmospheric composition. Furthermore, an overview of systematic errors as well as propects for JWST are given, before drawing the conclusions in Chapter 5.

Chapter 2

Methodology

2.1 Sample

As mentioned in the previous chapter, the focus in this analysis will be on the class of Hot Jupiters. Taking the definition of Hot Jupiters (see Section 1.1) into account, the majority of the transmission spectra were taken from the NASA Exoplanet Archive[1] and supplemented by spectra from David Sing's spectral library[2]. The planets in the sample and their spectral coverage are shown in Table 2.1, using the observations made with space-based instruments such as the HST spectrographs WFC3 ($R=\lambda/\Delta\lambda=30-200$) in the NIR and STIS ($R=530-1040$) in the UV and optical. Additionally, a large fraction of the sample has mid-IR photometric measurements using the Spitzer IRAC 1 and 2 bands. Finally, HD 189733b was also observed using HST NICMOS[3] (at 1.9 and 2.3μm) by Sing et al. (2016). The reanalysis of the spectra, as well as the use of only space-based observations, is done for the purpose of homogeneity: this is a key requirement in our search for any possible chemical trends.

TABLE 2.1: Wavelength coverage of Hot Jupiters in the sample as well as reference to the primary source of the data.

Planet	STIS $(0.3 - 1.1\mu$m)	WFC3 $(1.1 - 1.7\mu$m)	SPITZER (3.6 and 4.5μm)	Reference
HAT-P-1b	Yes	Yes	Yes	Sing et al., 2016
HAT-P-12b	Yes	Yes	Yes	Sing et al., 2016
HAT-P-26b	Yes	Yes	Yes	Wakeford et al., 2017b
HD 189733b	Yes	Yes	Yes	Sing et al., 2016
HD 209458b	Yes	Yes	Yes	Sing et al., 2016
WASP-6b	Yes		Yes	Nikolov et al., 2015
WASP-12b	Yes	Yes	Yes	Sing et al., 2013; Sing et al., 2016
WASP-17b	Yes	Yes	Yes	Sing et al., 2016
WASP-19b	Yes	Yes	Yes	Huitson et al., 2013; Sing et al., 2016
WASP-31b	Yes	Yes	Yes	Sing et al., 2015; Sing et al., 2016
WASP-39b	Yes	Yes	Yes	Sing et al., 2016; Wakeford et al., 2018
WASP-52b	Yes		Yes	Alam et al., 2018
WASP-43b		Yes		Kreidberg et al., 2014
WASP-101b		Yes		Wakeford et al., 2017a
WASP-107b		Yes		Kreidberg et al., 2018
WASP-121b		Yes		Evans et al., 2016
XO-1b		Yes		Deming et al., 2013

Figure 2.1 illustrates the class of planets that we are dealing with in this analysis. The planets, indicated with an abbreviation of their name, can be found in sizes ranging between $0.5R_J < R_p < 2.0R_J$, which is proposed as the size range of Hot Jupiter planets by Borucki et al. (2011). The radii of Earth and Jupiter are indicated vertically by the blue and purple

---

[1]NASA Exoplanet Archive
[2]https://pages.jh.edu/~dsing3/David_Sing/Spectral_Library.html
[3]Near Infrared Camera and Multi-Object Spectrometer

line respectively: their separations from the Sun are 1 and 5.2 AU, greatly exceeding the orbital distances of Hot Jupiters. As explained in the previous chapter, these Hot Jupiters are indeed planets around the size of Jupiter that orbit close to their host star. The 12 planets accompanied by green labels have coverage by multiple instruments, whereas the 5 with blue labels have coverage by WFC3 only. The triangles in Figure 2.1 indicate the reported presence of H_2O, Na, K and/or H for a planet. Next to these as of yet most frequently discovered species, other species that have been detected are discussed in Section 1.3. Some examples of transmission spectra that have been analysed as part of this investigation are shown in Figure 2.2. These spectra demonstrate the varying and limited spectral coverage that we are dealing with, while they also indicate a few clearly distinguishable spectral features. The colors illustrate the spectral ranges that are covered by the instruments and it can be seen that HD 189733b (the only planet in our sample) has some additional NIR observations by NICMOS.
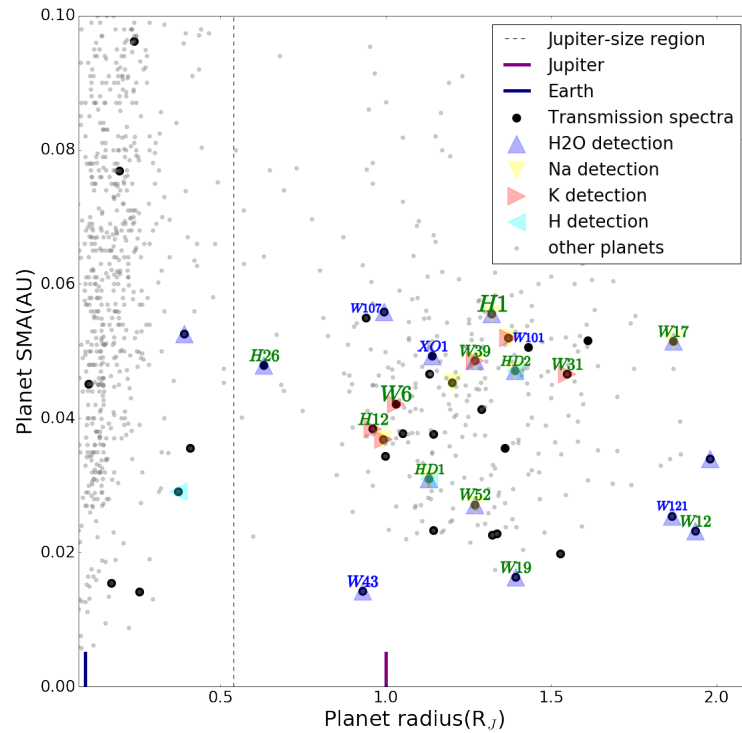
FIGURE 2.1: Locations of the planets of Table 2.1 in the radius versus semi-major axis plane, as taken from the NASA Exoplanet Archive. For example, HD2 stand for HD 209458b which refers to the point right below it. The dashed vertical line indicates the lower radius boundary of the Hot Jupiter class according to Borucki et al. (2011), while the solid blue and purple lines indicate the radii of Earth and Jupiter respectively. Besides that the as of yet 4 most detected chemical species using transmission spectroscopy are imposed on the specific planet of discovery with a triangle (Madhusudhan, 2019).
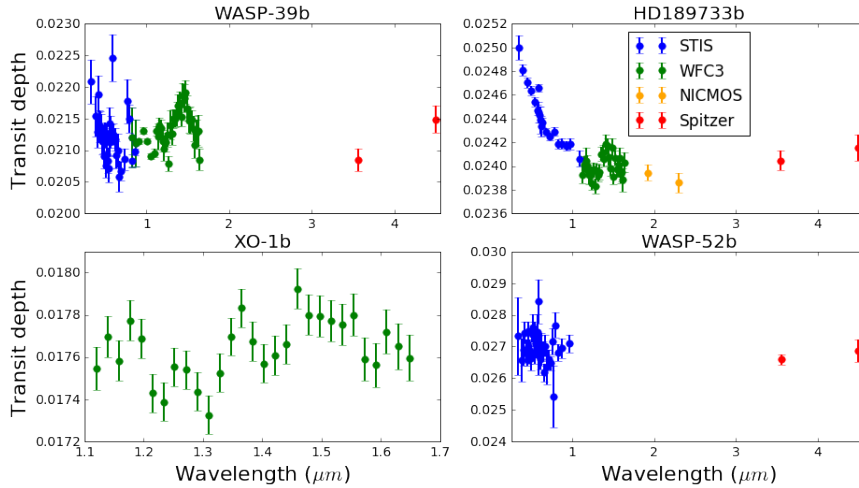
FIGURE 2.2: The observations of some of the planets as taken from the sources as indicated in Table 2.1. The corresponding planet names are indicated and the instruments used for the observations are indicated by the colors.

2.2 TauREx II

The retrieval of atmospheric parameters for this sample has been performed using TauREx II (Waldmann et al., 2015), which is a line-by-line radiative transfer Bayesian retrieval framework and is publicly available[4]. TauREx maps the correlations between atmospheric parameters and provides statistical estimates on their values. In the course of this work, the framework was upgraded to TauREx III with an associated decrease in retrieval times (Al-Refaie et al., 2019). After a brief description of the underlying model representing the atmosphere, an overview of retrieval theory and its procedures will be given. The final part of this chapter provides the general setup of our analysis.

2.2.1 Forward Model

As introduced in Section 1.2.1, the transmission spectrum tells us about the absorption of stellar light by the planetary atmosphere. To understand these observations, a Forward Model(FM) provides a line-by-line integration scheme to model the transmission of radiation of a host star through the atmosphere of an orbiting planet (Hollis et al., 2013). This FM output is then compared to the observations to estimate absorber abundances.

When radiation passes through a medium (e.g. an atmosphere) along a path ds, its intensity I_λ suffers from absorption and scattering:

$$\frac{dI_\lambda}{I_\lambda} = -\sigma_\lambda n ds = -\rho k_\lambda ds \tag{2.1}$$

The usage of the wavelength-dependent extinction or absorption cross-section σ_λ in m^2 together with the number density n of the material (m^{-3}) is equivalent to using the extinction or absorption coefficient k_λ in m^{2}kg^{-1} together with the density ρ of the material in kgm^{-3}. The unitless optical depth τ_λ describes the attenuation of radiation passing through a material and is defined as:

$$\tau_\lambda = \int \sigma_\lambda n ds = \int \rho k_\lambda ds \tag{2.2}$$

---

[4]https://exoai.github.io/software/taurex/

Integrating Equation 2.1 we obtain the Beer-Bouguer-Lambert Law, describing the monochromatic intensity of radiation passing through a gas as a function of the altitude z:

$$I_\lambda(z) = I_\lambda(0)exp(-\tau_\lambda(z)) \tag{2.3}$$

Where $I_\lambda(0)$ is the incident radiation on top of the atmosphere (i.e. the 'fresh' starlight), λ is the wavelength of the radiation and $\tau_\lambda(z)$ is the optical depth of the medium. Usually, the assumption of a plane-parallel atmosphere is made: the atmosphere consists of a specified number of homogeneous atmospheric layers (in T, P, properties of a given species, etc.).
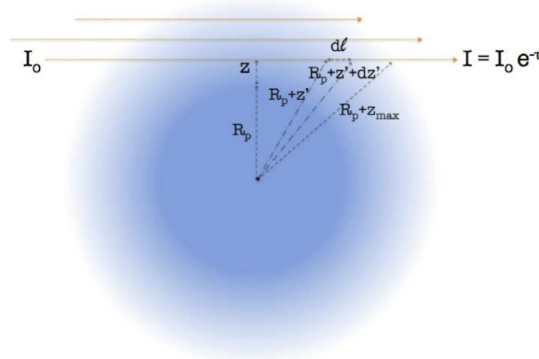
FIGURE 2.3: Illustration showing the paths of stellar photons that are passing through a planetary atmosphere in a transverse manner (Hollis et al., 2013).

As opposed to attenuation as a function of altitude, in transmission geometry the radiation transverses the atmosphere along our line of sight: Figure 2.3 demonstrates the path *dl* of a photon through the planetary atmosphere. The optical path depends on the amount of a particular molecule *i* that the photon will encounter during its passage. However, a particular volume can be a mixture of several species that influence the radiation. The total optical depth is then given by the sum of *N* individual molecules present using Equation 2.2 and integrating over the path *dl*:

$$\tau_\lambda(z) = 2\sum_{i=1}^{N}\int_0^{l(z)} \sigma_{i,\lambda}(z')\chi_i(z')n(z')dl \tag{2.4}$$

In here the factor 2 results from the assumed symmetric geometry and the abundance of a particular molecule is expressed as the Mixing Ratio χ_i: its abundance relative to that of all the other components of the atmosphere or:

$$\chi_i = \frac{n_i}{n_{tot}} \tag{2.5}$$

The path *dl* can be deduced from the geometry in Figure 2.3 and is given by:

$$dl = \sqrt{(R_p + z' + dz')^2 - (R_p + z)^2} - \sqrt{(R_p + z')^2 - (R_p + z)^2} \tag{2.6}$$

And for the transverse pathlength as a function of altitude:

$$l(z) = \int dl = \sqrt{(R_p + z_{max})^2 - (R_p + z)^2} \tag{2.7}$$

The equivalent atmospheric depth (area) can then be calculated by integrating over all viewing paths, illustrated by the different lines crossing the atmosphere in Figure 2.3:

$$A(\lambda) = 2\int_0^{z_{max}} (R_p + z)(1 - e^{-\tau_\lambda(z)})dz \tag{2.8}$$

This can be translated into a total transit depth via:

$$\delta_\lambda = \frac{R_p^2 + A_\lambda}{R_*^2} \tag{2.9}$$

Molecular absorption reduces the transmitted flux by a factor $(1 - e^{-\tau_\lambda(z)})$, which is equivalent to the transit of an opaque body of slightly larger radius. This represents the wavelength-dependent transit depth (see Section 1.2.1) that is observed in a transmission spectrum and allows us to quantify the observed spectrum.

2.2.2 Opacities

The propagation of radiation through an atmosphere is thus strongly dependent on the atmospheric state (temperature, pressure) and composition. An important interaction is the one between radiation and the gases in the atmosphere: all gases scatter and many also absorb (and emit) radiation. The ability of an atmospheric gas to absorb a photon of a particular wavelength λ depends on its structure. Atomic species can only emit or absorb photons when an electron makes a transition between energy levels. Molecular absorption defines the interaction between the gas molecules and the electromagnetic radiation and consists of several components that specify the transitions between energy levels:

$$E = E_{rot} + E_{vib} + E_{el} \tag{2.10}$$

- E_{rot} is the energy of rotation of the molecular structure ($\sim 10^{-3}$eV: transitions in (sub)-millimeter)

- E_{vib} is the energy of a molecule vibrating around its equilibrium structure (~ 0.1eV: in infrared)

- E_{el} is the energy associated with the electron arrangement of a molecule (~ 10eV: in optical/UV)

The energies E_{rot}, E_{vib} and E_{el} are quantized and take only discrete values. The transitions between these energy states are generally subject to selection rules, which means that a molecule can have many transitions between these different energy states causing absorption and emission lines that may be at wavelengths specific to that molecule. This gives us an opportunity to identify a particular species according to its spectral signatures. A more extended description of molecular spectroscopy can be found in Liou (2002) (in the context of atmospheric transmission) and in Atkins et al. (2014) (a more general description). For the molecular opacities, TauREx relies heavily on the ExoMol project (Tennyson et al., 2016). ExoMol is a database of molecular line lists, which are comprehensive lists containing the spectroscopic transitions of a particular species and may consist of up to 10^{10} lines. These lists provide the transition frequencies and probabilities for a particular molecule, while the addition of degeneracy factors and partition functions gives the dependence on temperature and pressure-broadening parameters give the specific line shape. The linelists relevant to our analysis are shown in Table 2.2.

There is a threefold motivation for the choice of chemical species. Firstly, equilibrium chemistry models can predict the presence and expected abundances for species as a function of temperature, assuming an initial elemental composition (e.g. Woitke et al. (2018)). This predicts the main element-bearing species at the temperatures of Hot Jupiters, which are, for example, H_2O and CO for oxygen, CO, CO_2 and CH_4 for carbon and TiO for titanium. Besides that, a possible detection requires the species to have signatures in the observed spectral regime. Knowledge of absorption signatures of e.g. AlO, CaH, CrH, FeH, TiO and VO is informed by their detections in brown dwarfs (e.g. Kirkpatrick et al. (1999)), whereas the prominent signatures of Na and K are identifiable in the optical regime (e.g. Charbonneau et al. (2002)). Most of the nitrogen is expected to be present in N_2. Being a diatomic molecule (see section 2.2.3), N_2 has no signatures in the infrared. NH_3 is the next main nitrogen-bearing species and does have signatures, motivating its inclusion. Lastly, species such as C_2H_2, HCN and OH are expected to be produced by photochemical processes (e.g. Kawashima et al. (2019), Line et al. (2010)).

Molecule	Wavelength range	Number of lines	Line list data
AlO	$0.285-100\mu m$	4,945,580	ExoMol: Patrascu et al. (2015)
C_2H_2	$1-100\mu m$	4,347,381,911	ExoMol: Chubb et al. (2020b)
CaH	$0.456-100\mu m$	19,095	Li et al. (2012), Bernath (2020)
CH_4	$0.82-100\mu m$	34,170,582,862	ExoMol: Yurchenko et al. (2017)
CO	$0.451-100\mu m$	752,976	Li et al. (2015)
CO_2	$1.036-38.75\mu m$	11,167,618	HITEMP: Rothman et al. (2010)
CrH	$0.667-1.667\mu m$	13,824	Burrows et al. (2002), Bernath (2020)
FeH	$0.667-6.667\mu m$	93,040	Wende et al. (2010)
H_2O	$0.243-100\mu m$	5,745,071,340	ExoMol: Polyansky et al. (2018)
HCN	$0.569-100\mu m$	34,418,408	ExoMol: Barber et al. (2014)
K	$\sim 0.59\mu m$	634	NIST: Allard et al. (2016), Kramida et al. (2013)
Na	$\sim 0.77\mu m$	869	NIST: Allard et al. (2019), Kramida et al. (2013)
NH_3	$0.435-100\mu m$	16,941,637,250	ExoMol: Coles et al. (2019)
OH	$0.230-100\mu m$	54,276	Yousefi et al. (2018)
TiO	$0.333-100\mu m$	59,324,532	ExoMol: McKemmish et al. (2019)
VO	$0.286-100\mu m$	277,131,624	ExoMol: McKemmish et al. (2016)

TABLE 2.2: Properties and references for the line lists used in this analysis.

These line lists have been converted into cross-sections and k-tables to feed them to Tau-REx by Chubb et al. (2020a) and in this study we have used the k-tables with $R=\frac{\Delta\lambda}{\lambda}=300$. A k-table provides the absorption coefficient as a function of wavelength for a certain temperature and pressure and an example of this is shown in Figure 2.4 for H_2O. From this figure, it is evident that while most of the signatures of H_2O fall outside the spectral regimes of the current instruments STIS and WFC3 at HST, there is a clear signature around $1.4\mu m$ that usually leads to water detections (e.g. Sing et al., 2016; Tsiaras et al., 2018). Furthermore, Figure 2.4 provides a glance into the enhanced wavelength coverage offered by future facilities such as the James Webb Space Telescope (JWST) (Stevenson et al., 2016) and ARIEL (Tinetti et al., 2018). This will be further discussed in Section 4.6.
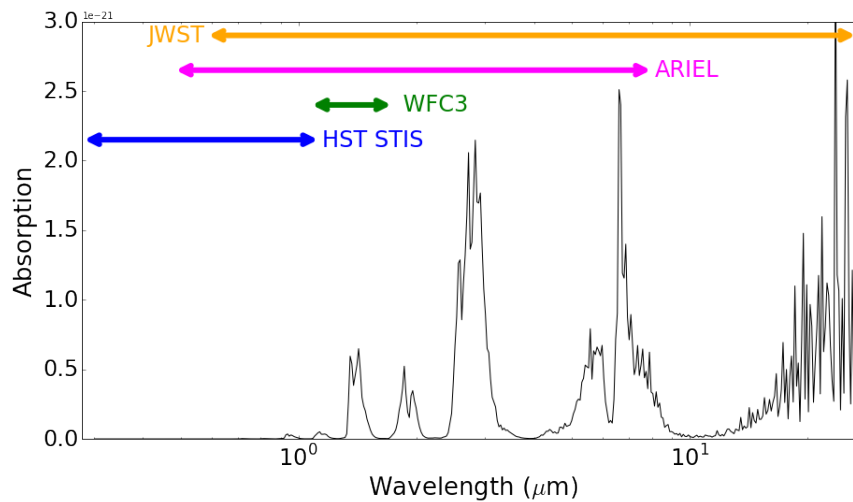
FIGURE 2.4: The absorption spectrum of H_2O at R=300 for a temperature of 1200K and pressure of 4.64 mbar, as calculated from the ExoMol project line lists (Tennyson et al., 2012). The spectral regimes of current (STIS, WFC3) and future (ARIEL, JWST) instruments are shown with arrows of different color.

2.2.3 Collision Induced Absorption

Contrary to molecules such as H_2O, diatomic molecules (e.g. H_2 and N_2) lack a permanent dipole moment due to their symmetry. Therefore, the rotational and vibrational energy levels can not be excited by the absorption of radiation and the molecules do not absorb in the infrared. However, inelastic collisions in high-pressure environments (such as the lower layers of an atmosphere) may induce a dipole moment and thus quantum transitions, causing

the absorption of infrared light. The opacity caused by CIA of pairs of H_2-H_2 and H_2-He is included in the calculation of the optical depth, using the relative abundances of each species and cross-sections from HITRAN and Borysow (Richard et al., 2012) (Borysow, 2002).

2.2.4 Particle Scattering

Clouds and hazes both consist of aerosols and therefore two distinct mechanisms exist to form aerosols: clouds are equilibrium condensates, forming when a gaseous species condenses out into liquid phase and produce layers of increased optical depth. Hazes have a non-thermodynamic origin and are produced by chemical pathways that are usually initiated by UV photolysis (e.g. Kawashima et al. (2019)). These particles will also interact with the stellar light that enters an atmosphere: when a beam of light impinges on a particle, the light will be scattered in all directions and partly absorbed as thermal energy. Hence, both clouds and hazes lead to weak absorption features and strong scattering slopes in transmission spectra. Mathematically, this particle scattering is described by Mie theory (e.g. Seinfeld et al. (1998)). On top of the scattering process, even more complexity can be expected based on the variety of clouds that we see on Earth. The cloud optical depths depend on the thickness of clouds, the relative content in water droplets versus ice crystals and the size distribution of particles. Naturally, the optical depths can differ greatly between the different types of clouds that are found (e.g. high-z cirrus clouds with low optical depth, low-z stratus clouds with very high optical depth).

In TauREx clouds/hazes are parameterized as consisting of spherical enstatite ($MgSiO_3$) particles (Lee et al., 2013), because this is one of the species expected to condense out at the temperatures of Hot Jupiters (Lodders, 2010). Following Lee et al. (2013), the cloud optical depth can be written as:

$$\tau_{c1,\lambda} = \int_0^{l(z)} Q_{ext,\lambda} \pi a^2 \chi_c(z) \rho_N(z) dl \tag{2.11}$$

Where a is the size of the cloud or haze particle, $\chi_c(z)$ is the cloud mixing ratio, dl is the path length through the atmosphere and $Q_{ext,\lambda}$ is the cloud extinction coefficient, describing the extinction efficiency for the particle. This extinction efficiency quantifies the absorption and scattering (first order only) and it is mainly governed by the λ of the incoming light and the size of the particle, usually expressed together as the size parameter $x = \frac{2\pi a}{\lambda}$ (Lee et al., 2013). Approximations for the scattering processes exist in three regimes:

- $x \gg 1$: for large particles compared to the wavelength there is a flat or gray dependence on λ.

- $x \approx 1$: particles that are approximately the same size as the wavelength scatter preferably in the forward direction and lead to a weak dependence on wavelength, following the theories of Mie scattering.

- $x \ll 1$: for small particles compared to the wavelength there is the strong λ^{-4} dependence of Rayleigh scattering.

In the regime of Rayleigh scattering, the pattern of scattered light is basically symmetric in the forward and backward direction. The intensity of the scattered light is proportional to λ^{-4}, so the shorter the wavelength of the radiation, the more intensely it is scattered. Therefore, the blue component of sunlight is scattered more intensely by the atmospheric molecules causing the blue appearance of the skies on Earth. The opacity caused by Rayleigh scattering is included in the calculation of the optical depth by using pre-computed cross-sections and relative abundances (Hollis et al., 2013). When the scattering slope has a weaker wavelength dependence, it is described by Mie scattering in our atmospheric model, leading to an additional three free parameters a, $\chi_c(z)$ and $Q_{ext,\lambda}$ in the retrieval (see Equation 2.11).

Furthermore, the model has a parameterization of an optically thick gray-cloud cover:

$$\tau_{c2,\lambda} = \begin{cases} > 1 & \text{if } P > P_{cloud-top} \\ 0 & \text{otherwise} \end{cases} \tag{2.12}$$

This means that below the cloud-top pressure (thus at higher pressures) all radiation will be absorbed and that the skies above the cloud-top pressure are clear. This cloud-top pressure is included in all of the atmospheric models as P_{cl}.

2.3 Retrieval Theory

The observations were conducted without making direct physical contact with the object and, thus, are remote measurements. In such a measurement, the quantity that is measured is usually a non-trivial function of the underlying parameters of the object, as is also illustrated by the Forward Model in the previous section. If we wish to acquire the underlying parameters from the observations, we speak of the inversion or retrieval problem. In studies of exoplanet atmospheres, the retrieval problem signifies: given the planetary spectrum that is observed, what is the most likely composition and state of the planetary atmosphere? (Benneke et al., 2012)

2.3.1 Bayesian Parameter Estimation

As said before, the retrieval or parameter estimation in TauREx is fully Bayesian. As the first step in Bayesian statistics, a model has to be constructed that is believed to be an adequate description of the physical phenomenon under study. This is the Forward Model as described in Section 2.2.1. Then a prior distribution is formulated before analysing the actual observation. This is based on our understanding of the system and is preferably as 'flat' as possible, to prevent the inclusion of human biases. In other words, a wide parameter space needs to be explored in the retrievals. Thirdly, the observations are analysed and, through the usage of Bayes' theorem, posterior distributions of the underlying parameters are derived. A more extensive review of the applications of Bayesian statistics in cosmology and astrophysics can be found in Trotta (2008).

Given a Forward Model $\mathcal{M}$ consisting of atmospheric parameters $\boldsymbol{\theta} = [\theta_1, ..., \theta_n]$, the posterior probability distribution of the model parameters $\boldsymbol{\theta}$ given the dataset $\mathbf{x}$ can be computed using Bayes' theorem (Waldmann et al., 2015):

$$P(\boldsymbol{\theta}|\mathcal{M}, \boldsymbol{x}) = \frac{P(\boldsymbol{\theta}, \mathcal{M})\mathcal{L}(\boldsymbol{x}|\mathcal{M}, \boldsymbol{\theta})}{P(\boldsymbol{x}|\mathcal{M})} \tag{2.13}$$

In this equation, $P(\boldsymbol{\theta}, \mathcal{M})$ is the Bayesian prior probability density function of the atmospheric state and $\mathcal{L}(\boldsymbol{x}|\mathcal{M}, \boldsymbol{\theta})$ the likelihood function. The likelihood function represents the probability of measuring the data $\boldsymbol{x}$ given that the atmospheric parameters are $\boldsymbol{\theta}$ and this estimates the uncertainty in the observations. $P(\boldsymbol{x}|\mathcal{M})$ is known as the Bayesian evidence. It represents the probability of the data given the model and can, therefore, describe the adequacy of the model itself.

2.3.2 Nested Sampling

In TauREx, Equation 2.13 can be solved using Nested Sampling through the MultiNest implementation (Feroz et al., 2008; Feroz et al., 2009; Skilling, 2004). Nested sampling searches the whole multidimensional parameter space for solutions that fit the data and also provides us with the Bayesian evidence, allowing the determination of a statistically robust confidence of our atmospheric detections.

The multimodal Nested Sampling algorithm computes the Bayesian evidence of retrieval models and produces the joint probability distribution functions of atmospheric parameters. What follows is an overview of the algorithm, a more elaborate description can be found in Feroz et al. (2008) and Feroz et al. (2009). Besides allowing us to state detection confidences in a statistical manner, Nested Sampling has the advantage of searching the full multi-dimensional parameter space for regions providing a good fit to the data. The Bayesian Evidence as seen in 2.13 is given by:

$$E = P(x|\mathcal{M}) = \int P(\boldsymbol{\theta}, \mathcal{M})\mathcal{L}(\boldsymbol{x}|\mathcal{M}, \boldsymbol{\theta})d\mathbf{x} \tag{2.14}$$

In Nested Sampling, this integral is transformed into a 1-dimensional integral by using the relationship between the likelihood $\mathcal{L}$ and prior volume V. The prior volume $V(\mathcal{L}^*)$ is the total prior probability mass contained within the iso-likelihood contour $\mathcal{L}(x|\mathcal{M}, \theta) = \mathcal{L}^*$. As the likelihood increases the restriction on the likelihood becomes tighter and thus the prior volume decreases. To illustrate, the extreme values are:

- $V = 1$ for $\mathcal{L}^*$=0, since we consider the entire prior parameter space

- $V = 0$ for $\mathcal{L}^* \to \infty$

The inverse $\mathcal{L}(V)$ is then also a monotonically decreasing function (Feroz et al., 2008). At a set of decreasing prior volumes, Equation 2.14 can then be approximated by standard quadrature methods and using the trapezium rule we have:

$$E = \sum_{i=1}^{M} w_i \mathcal{L}_i \qquad (2.15)$$

Where the weight $w_i = \frac{1}{2}(V_{i-1} - V_{i+1})$ and $\mathcal{L}_i$ is the likelihood limit $\mathcal{L}^*(V_i)$ at iteration i. A sequence of $\mathcal{L}^*(V_i)$ values is generated by randomly drawing a user-specified number of samples or 'live points' from the prior distribution $P(x|\mathcal{M})$ and computing their likelihood. The following steps are then taken in Nested Sampling:

- In the first iteration, for a prior volume $V_0 = 1$, the samples are ordered according to their likelihood.

- The sample with the lowest likelihood $\mathcal{L}_1$ is the worst fit to the data and this sample is then replaced by a newly generated sample with the likelihood constraint $\mathcal{L} > \mathcal{L}_1$.

- A new iso-likelihood contour of $\mathcal{L}_1 = \mathcal{L}^*$ is specified such that all samples have $\mathcal{L}(\theta) > \mathcal{L}_1$ and this results in a new prior volume $V_1 < V_0$.

- In subsequent iterations, the sample with the lowest $\mathcal{L}_i$ is repeatedly replaced and the corresponding prior volume further tightened. This is repeated until the regions of highest likelihood are localized, which happens when the change in Bayesian evidence of a sample doesn't change by more than 0.5 (user-specified).

In the end, the values for the Bayesian evidence can then be used to construct the joint posterior distributions of the model parameters, by assigning the discarded samples at each iteration with a weight:

$$W_i = \frac{w_i \mathcal{L}_i}{E_i} \qquad (2.16)$$

The main challenge is the efficient generation of random samples in the iso-likelihood $\mathcal{L}^* = \mathcal{L}_i$, especially if we keep drawing the random samples from the full prior probability distribution in every iteration. To circumvent this, at each iteration all the livepoints are partitioned via local clustering and an optimum number of ellipsoids encompass all samples. As we advance in iterations, the ellipsoids start to encompass only regions of high likelihood and new samples are drawn from within these ellipsoids. Hence, the new random samples have intrinsically high likelihoods and this results in higher efficiency.

2.3.3 Model Selection

Nested Sampling allows us then to compare models of different complexity and the next step in retrieval would be to choose the best model to fit the data: for example, which molecular species definitely has to be included in the model? The noisy observations complicate easily detecting spectral signatures while different molecules often have overlapping signatures. There is a twofold requirement in choosing the best model (Waldmann et al., 2015):

- Parameter adequacy: is a parameter required to describe the underlying physics? If not, we may be overfitting the data and hence not obeying Occam's razor.

- Model adequacy: are there any parameters missing in the model? If yes, the data is fitted by an under-complete model.

Therefore, it is essential to choose the model that provides the best balance between quality of the fit and model complexity. Bayesian retrieval offers a rational way of model comparison by the calculation of the Bayesian evidence (see Equation 2.14). This can be seen as a quantification of the adequacy of the model $\mathcal{M}$, consisting of a set of atmospheric parameters $\boldsymbol{\theta}$ with probability distribution $P(\boldsymbol{\theta}, \mathcal{M})$, considering the data $\boldsymbol{x}$. Following Occam's razor, that added complexity in a model is only appropriate when the model gives a significantly better fit than the simpler model, then provides a procedure to quantify the detection confidence of an atmospheric constituent. When comparing two models, $\mathcal{M}_2$ having an extra atmospheric parameter and thus more complexity than $\mathcal{M}_1$, the ratio of the model probabilities or Bayes factor can be calculated (Kass et al., 1995) using:

$$\mathcal{B}_{21} = \frac{E_2}{E_1} \tag{2.17}$$

Or, defining the Detection Significance:

$$DS = ln(\mathcal{B}_{21}) = ln(E_2) - ln(E_1) \tag{2.18}$$

The empirically calibrated Jeffrey's scale (Jeffreys, 1998) as seen in Table 2.3 can then be used to quantify the preference of an additional atmospheric parameter, with a logarithmic Bayes factor $\mathcal{B}_{21} > 1$ providing evidence in favour of the more complex model. We can refer to this as the detection significance DS, since more complexity will usually be represented by addition of a particular chemical species to our model.

$ln\mathcal{B}_{21}$	Probability	σ	p-value	Category
< 1.0	< 0.750	< 2	> 0.04	Inconclusive
1.0	0.750	2.1	0.04	Weak evidence
2.5	0.923	2.7	0.006	Moderate evidence
5.0	0.993	3.6	0.0003	Strong evidence
11.0		5.0	6×10^{-7}	

TABLE 2.3: Empirically calibrated Jeffrey's scale with translation to frequentist values, from Trotta (2008).

Whereas the Bayes factor actually quantifies the evidence for a more complex model, the frequentist p-value should be treated with caution. The p-value gives the probability of the data, assuming that the null hypothesis (e.g. the simpler model) is true. Hence, it can only be used to reject the null hypothesis that a simpler atmospheric model without the chemical species can reasonably explain the data. Although helpful in exploratory analysis, what we actually want is the probability of a model given the data and use this to compare two models of different complexity. The sigma value corresponds to the number of standard deviations away from the mean for a normal distribution and also specifies the probability of the observed data assuming that the null hypothesis is true.

2.4   General retrieval setup

In this analysis, the atmospheres were modelled as consisting of 100 layers ranging in pressures from 10^6 to 10^{-5} Pa. The atmospheres are assumed to be isothermal because the limited spectral coverage and the geometry of transmission spectroscopy do not allow the recognition of a more complex profile. The calculation of the prior temperature and fitting boundaries is explained in Appendix B.1. Besides that, we assume a Hydrogen-dominated atmosphere with an approximately Jupiter-like ratio of $He/H_2 = 0.15/0.85$, which is the default in TauREx (Waldmann et al., 2015). Table 2.4 gives an overview of the planetary parameters that have been used in the analysis.

TABLE 2.4: The planetary parameters used.

Planet	$R_p(R_J)$	$M_p(M_J)$	SMA(AU)	T_{eq} (K)[a]	T_l	T_u	Reference
HAT-P-1 b	1.242	0.525	0.056	1200	748	1533	Bonomo et al. (2017)
HAT-P-12 b	0.959	0.208	0.038	843	525	1077	Bonomo et al. (2017)
HAT-P-26 b	0.63	0.07	0.048	927	578	1185	Stassun et al. (2017)
HD 189733 b	1.138	1.123	0.031	1093	682	1397	Bonomo et al. (2017)
HD 209458 b	1.359	0.682	0.047	1321	824	1688	Bonomo et al. (2017)
WASP-6 b	1.224	0.483	0.042	1225	764	1566	Bonomo et al. (2017)
WASP-12 b	1.825	1.39	0.02	2242	**500**	2865	Bonomo et al. (2017)
WASP-17 b	1.991	0.512	0.052	1507	940	1926	Bonomo et al. (2017)
WASP-19 b	1.392	1.069	0.016	1857	1158	2373	Wong et al. (2016)
WASP-31 b	1.549	0.489	0.047	1393	869	1780	Bonomo et al. (2017)
WASP-39 b	1.270	0.275	0.049	1015	633	1297	Bonomo et al. (2017)
WASP-52 b	1.270	0.459	0.02	1023	**400**	1307	Bonomo et al. (2017)
WASP-43 b	1.036	2.050	0.014	1233	769	1575	Bonomo et al. (2017)
WASP-101 b	1.410	0.497	0.051	1421	**400**	1816	Bonomo et al. (2017)
WASP-107 b	0.94	0.12	0.055	671	418	857	Anderson et al. (2017)
WASP-121 b	1.865	1.183	0.025	2200	1372	2810	Delrez et al. (2016)
XO-1 b	1.206	0.913	0.049	1073	669	**3000**	Bonomo et al. (2017)

[a] The prior values for the isothermal atmospheric temperature (Bond Albedo $A = 0.34$, redistribution factor $f = 1$) and lower and upper boundaries for the temperature assuming $A = 0.9$, $f = 1$ and $A = 0.12$, $f = 0.5$ respectively, a more extensive description can be found in Appendix B.1. Where retrievals gave indications of atmospheric temperatures outside the calculated range, the newly adopted value is indicated in bold.

2.4.1 Free parameters

Having specified our atmospheric model, the next step is to define the parameters that will be included in the retrieval and their associated prior boundaries. The planetary radius (see Table 2.4) is fitted as part of the retrieval, with boundaries at $R_p \pm 0.1R_p$. The prior boundaries for retrieving the temperature can be found in the same Table and the gray cloud deck was fitted at pressures ranging from 10^6 to 10^{-5} Pa. The chemical abundances are retrieved with prior Volume Mixing Ratios between 10^{-10} and 10^{-1} and provide specific opacities (based on the line lists shown in Table 2.2) in addition to the pre-computed Rayleigh scattering and CIA. From the retrieved abundances, the atmospheric molecular weight is then calculated. Finally, the inclusion of the opacity that is caused by Mie scattering provides 3 additional free parameters (Q_0, a, χ_c: see Section 2.2.4) for which we follow the log-uniform prior boundaries of Tsiaras et al. (2018). In the end, up to 22 free parameters can thus be retrieved in the procedure. However, to explain the limited spectral coverage only a small fraction of these parameters will statistically be required. Together with the feasibility of quantifying the importance of individual molecules, this is one of the main reasons for a bottom-up approach.

2.4.2 Bottom-up approach

This bottom-up approach is useful in determining the parameters that are needed to describe a particular transmission spectrum. The retrieval was first performed assuming the simplest atmospheric Forward Model consisting of 3 free parameters (R_p, T, P_{cl}), which is equivalent to an atmosphere completely lacking spectral signatures. Afterwards, retrievals were done by adding parameters to the atmospheric model, in the form of either the abundance of a chemical species or the 3 parameters describing the opacity of Mie scattering. In doing so, the spectrum of each planet was retrieved by assuming the 33 different atmospheric models of Table 2.5.

With the Bayesian evidence as an output of TauREx, a comparison between each of these models can then be made to quantify the Detection Significance (DS) of a particular chemical species, as described in Section 2.3.3. The first stage is to compare the models with a single

chemical species to the flat model (R_p, T, P_{cl} only). As opposed to the flat model, the opacity caused by Rayleigh scattering and CIA is from now on also included. If the addition of a chemical species leads to an improved fit to the data, this results in a higher evidence and the significance of such a detection is specified by Jeffreys' scale in Table 2.3. As a second stage, we tried the inclusion of H_2O plus another species, mainly because H_2O has a prominent absorption feature in the relatively well-covered NIR (see Figure 2.4). The evidences of these models can be compared to the models containing a single species as well as to the flat model. Lastly, for the planets with optical coverage by STIS (see table 2.1), the model with the highest evidence was expanded by adding the absorption features of the alkali metals Na and K. This results in strong absorption features due to the Na doublet at 5895.92 Å and 5899.95 Å respectively and the K doublet at 7664.90 Å and 7698.96 Å respectively (Kramida et al., 2013). In the end, for each planet, the atmospheric parameters of the model with the highest evidence were used for further investigation in possible chemical trends.

TABLE 2.5: The free parameters included in models that were fitted to the data, on top of P_{cl}, R_p and T. Note that the models with K and/or Na were not fitted to the planets without optical coverage.

Model parameters
No molecules, Rayleigh nor CIA
AlO
C_2H_2
CaH
CH_4
CO
CO_2
CrH
FeH
H_2O
HCN
NH_3
OH
TiO
VO
Mie scattering opacity
H_2O + AlO
H_2O + CaH
H_2O + C_2H_2
H_2O + CH_4
H_2O + CO
H_2O + CO_2
H_2O + CrH
H_2O + FeH
H_2O + HCN
H_2O + NH_3
H_2O + OH
H_2O + TiO
H_2O + VO
H_2O + Mie scattering opacity
Best Model + K
Best Model + Na
Best Model + Na + K

2.4.3 Towards chemical trends

The existence of a thermochemical trend can be investigated by using the atmospheric temperature and chemical abundances as resulting from the retrievals. To explore the possible existence of a photochemical trend, we need knowledge on the host star irradiance that is received by the planets and a trend with initial abundances would require host star abundance ratios. Table 2.6 provides an overview of the stellar parameters used in this study.

TABLE 2.6: Stellar parameters

Star	$R_*(R_\odot)$	$L_*(log_{10}(L_\odot))^a$	Age(Gyr)	$[Z/H](dex)^b$	T_{eff} (K)	$I_{FUV}(W/m^2)$
HAT-P-1	1.135	0.209	$2.7^{+2.5}_{-2}$	0.210 ± 0.030*	5980	1131
HAT-P-12	0.701	-0.727	2.5^{+2}_{-2}	-0.290 ± 0.050*	4650	18.33
HAT-P-26	0.87	-0.368	$9^{+3}_{-4.9}$	0.010 ± 0.040*	5079	77.29
HD 189733	0.756	-0.460	$6.8^{+5.2}_{-4.4}$	0.070 ± 0.036^o	5052	126.1
HD 209458	1.155	0.232	$3.1^{+0.8}_{-0.7}$	0.090 ± 0.036^o	6091	2092
WASP-6	0.87	-0.308	11^{+3}_{-7}	-0.140 ± 0.030*	5450	205.7
WASP-12	1.619	0.536	$2^{+0.7}_{-2}$	0.330 ± 0.036^o	6360	29532
WASP-17	1.572	0.539	$2.65^{+0.25}_{-0.25}$	0.080 ± 0.036^o	6550	7012
WASP-19	1.004	-0.096	$5.5^{+8.5}_{-4.5}$	0.180 ± 0.036^o	5568	3516
WASP-31	1.252	0.315	$1^{+3}_{-0.5}$	0.060 ± 0.036^o	6302	3689
WASP-39	0.895	-0.199	9^{+3}_{-4}	-0.120 ± 0.100*	5400	205.3
WASP-52	0.79	-0.377	$10.7^{+1.9}_{-4.5}$	0.030 ± 0.120*	5000	154.1
WASP-43	0.667	-0.866	7^{+7}_{-7}	0.050 ± 0.17	4400	37.42
WASP-101	1.290	0.421	$1.14^{+0.7}_{-0.65}$	0.200 ± 0.12	6380	4030
WASP-107	0.66	-0.811	$8.3^{+4.3}_{-4.3}$	0.020 ± 0.1	4430	3.409
WASP-121	1.458	0.583	1.5^{+1}_{-1}	0.130 ± 0.09	6459	23141
XO-1	0.934	-0.089	$1^{+3.1}_{-0.9}$	-0.040 ± 0.036^o	5750	473.4

^{a} luminosity derived from Gaia (Gaia Collaboration et al., 2018)
^{b} in terms of Solar: values with ^{o} are [O/H] ratios (Brewer et al., 2016), asterisk(*) are [Fe/H] (Santos et al., 2013), else [Fe/H] from the source in Table 2.4.

By combining the host star luminosity L_* and the planet's semi-major axis d, we can calculate the irradiance received at the planet's orbit:

$$I = \frac{L_*}{4\pi d^2} \tag{2.19}$$

Alternatively, the luminosity can also be derived from the stellar effective temperature by assuming it radiates as a blackbody. This has been done for our stellar sample and the resulting blackbody curves $B_\lambda(\lambda, T)$ are shown in Figure 2.5.
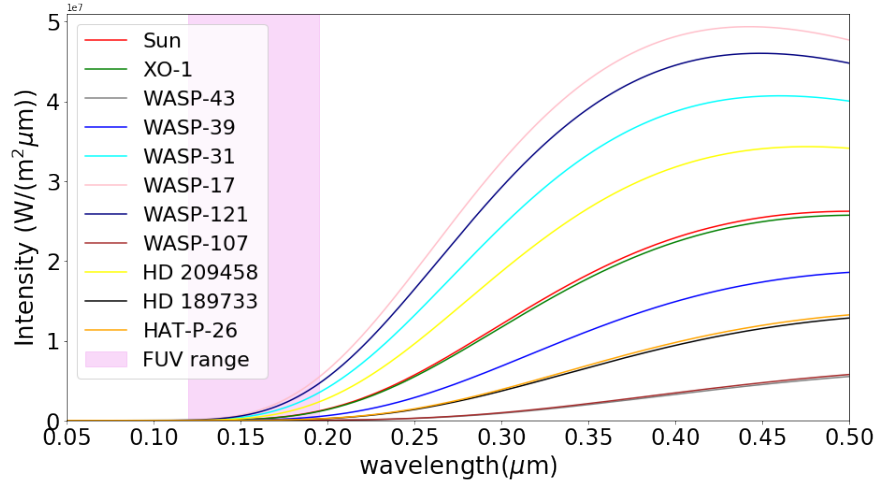
FIGURE 2.5: The blackbody curves for different stars in our sample.

The advantage of this estimation is that the stellar flux can be calculated for a specific wavelength range, giving us a means to estimate the stellar flux in the UV regime. Relating the resulting irradiance to the retrieved abundances may offer some insights into photochemistry, as described in Section 1.4.2. The stellar flux or total energy radiated per unit surface area in a specific spectral range can be calculated by integrating the area underneath the curve between this range:

$$F_\lambda = \pi \int_{\lambda_{low}}^{\lambda_{upp}} B_\lambda(\lambda, T) d\lambda \tag{2.20}$$

Where the factor π originates from the solid angle. Integrating the equation across all wavelengths will result in the Stefan-Boltzmann Law $F = \sigma T^4$. Combining Equations 2.20 and 2.19, the irradiation in a specific wavelength range received by a planet orbiting a star of radius R_* at a distance d is given by:

$$I_\lambda = F_\lambda \frac{R_*^2}{d^2} \tag{2.21}$$

To look for possible hints for the photodissociation of water, the UV irradiation as calculated in Table 2.6 has been limited to lower wavelengths ranging from 120 to 195nm (Heays et al., 2017), or the FUV regime[5]. Photons in this wavelength range might cause water photodissociation by creating OH and comparing the UV irradiation with retrieved abundances might provide clues towards this photodissociation. Using an effective temperature of 5772K, the blackbody method results in the expected Solar irradiance of 1361 W/m^2 and a Solar FUV irradiance $I_{120-195nm}$ of 1.565 W/m^2 at Earth's orbit.

---

[5]ISO standard, https://www.iso.org/standard/39911.html

Chapter 3

Results

This chapter presents the results from feeding the planetary spectra (see Table 2.1) to the TauREx II retrieval framework (Waldmann et al., 2015) under the assumption of the different atmospheric models of Table 2.5. This results in a total of 576 retrievals that had to be run and compared. With the aim of presenting the results in a clear way, the general procedure will first be described extensively for WASP-39b. Then a few noteworthy results for individual sources will be discussed before presenting the results of the sample as a whole.

3.1 The procedure in detail: WASP-39b

As described in Section 2.4 we are following a bottom-up approach. We start by fitting a flat model spectrum (i.e. one with no chemical features) of the least possible complexity to the data and subsequently add more free parameters (i.e. chemical species) to this model. The Bayesian Evidence (see Section 2.3.3) describes the adequacy of a fit and Figure 3.1 shows this Evidence for all of the models that have been fitted to the spectrum of WASP-39b.
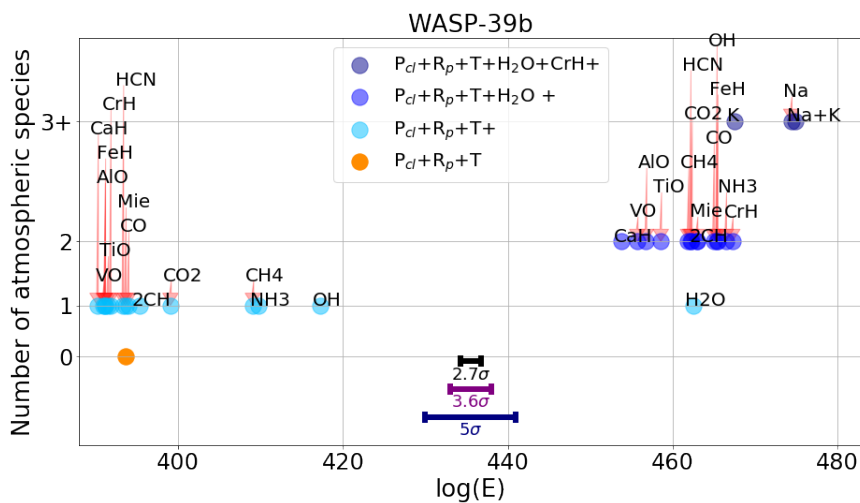

FIGURE 3.1: Model comparison for WASP-39b using the Bayesian evidence for different atmospheric models. The flat model is shown as the orange dot, while cyan dots indicate more complexity in the form of a chemical species or Mie scattering, specifically indicated by the label accompanying each dot. One level higher, blue dots represent H_2O and an additional parameter, again specified by the label accompanying the dot. For the fourth level, the highest evidence model from lower complexities is complemented by Na and/or K, as shown by the dark blue dots. The scale bars indicate the statistical preference for a more complex model over a simpler one and are based on the difference in Bayesian Evidence between models (see Table 2.3).

Starting from the lower left of the Figure, it can be seen that the flat model without any signatures (only R_p, T and P_{cl}; represented by the orange dot) leads to a Bayesian evidence of

394. We can increase a level in complexity by adding one atmospheric species, these models are shown as the cyan dots and specified by their accompanying label. A glance makes it evident that out of these models the inclusion of H_2O would give the best fit. The statistical preference of this model over the flat and the other cyan models can be read out from the positive difference between their evidences using the scale bars at the bottom of the Figure. The lengths of the bars are based on Jeffreys' Scale as shown in Table 2.3. The Detection Significance of 68.87 indicates that the model including H_2O is statistically preferred over the other cyan models with a significance greatly exceeding 5σ. We can ascend to a higher stage by including H_2O and adding another free parameter, specified again by the labels accompanying the blue dots in the middle of the plot. Since the model including H_2O and Chromium Hydride (CrH) has DS=73.63 over the flat model, we can conclude with over 3σ confidence that the inclusion of CrH would provide a more adequate fit to the data as compared to only H_2O. It should, however, be noted that there is only weak evidence (DS=0.79) that H_2O+CrH provides a better fit to the data than H_2O+NH_3.

Since the presence of Na (near $0.59\,\mu$m) and K (near $0.77\,\mu$m) provides clear absorption lines in the optical part of spectrum, the next stage is to add Na and/or K to the best-fitting atmospheric model of the earlier stages, so in this case R_p, T, P_{cl}, H_2O and CrH. The resulting evidences can be seen as the dark blue dots in the upper right corner of Figure 3.1 and their inclusion is preferred with a DS of 7.15 corresponding to $\sim 4\sigma$ confidence, as compared to the simpler models of one level below. Comparing the dark blue dots amongst themselves, the addition of K to the model including H_2O, CrH and Na only has a $\sim 2\sigma$ confidence. Since the Na and K absorption lines have such a specific shape, we can however easily identify them in a spectrum, as shown in Figures 3.2a and 3.2b (the strong absorption peaks near $0.59\,\mu$m and $0.77\,\mu$m). Because the line shapes are so specific, they can be represented by just a single measurement. This means that we might see only weak evidence for their inclusion according to Jeffreys' Scale. To ensure their inclusion as much as possible, the Na and K absorption lines will be seen as significant even when they lead to a statistical evidence that is below the 2.1σ threshold. We can then state our finding that, under this simplified representation of the atmosphere and out of the models fitted in this study, the spectrum of WASP-39 b is best represented by a model including H_2O, CrH, Na and K.

The spectrum of WASP-39b and the corresponding best-fitting atmospheric model are shown in Figure 3.2a. Clearly visible are the signatures of H_2O in the NIR (around 1.4μm) and Na and K in the visible part of the spectrum. The signatures can be seen even more clearly in Figure 3.2b, which shows the individual contributions to the opacity (or absorption) by each of the atmospheric constituents. Furthermore, the discovery of CrH is interesting and causes some absorption signatures between 0.7 and 1.5μm. The gray cloud-deck increases the transit depth equally at every wavelength, while CIA can be seen as another source of continuum absorption. Finally, the characteristic slope of Rayleigh scattering contributes to the optical part of the spectrum. Figure 3.3 shows the posterior distributions of the different parameters included in the retrieval for WASP-39 b, providing statistical estimates for the exact values of the atmospheric parameters according to the retrieval. The posteriors show that for WASP-39b, TauREx clearly converges to a solution in the multi-dimensional parameter space. The chemical abundances seem reasonable, the retrieved temperature is slightly lower than the equilibrium temperature and a gray cloud deck is only retrieved in the deep layers of the atmosphere. The statistical estimates on atmospheric parameters can be used for further analysis.

(A) Transmission spectrum of WASP-39b.
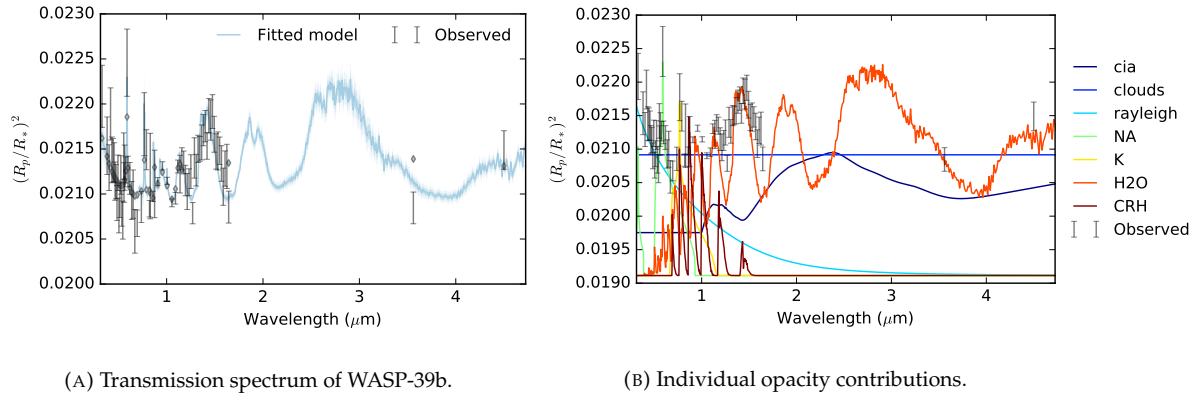
(B) Individual opacity contributions.

FIGURE 3.2: On the left the transmission spectrum and model fit of WASP-39b is shown. The vertical error bars indicate the transit observations and the overlaying lines are the best-fitting models with the different shadings corresponding to 1 and 2σ regions. The right panel shows the individual contributions to the opacity (or absorption) by the atmospheric constituents.

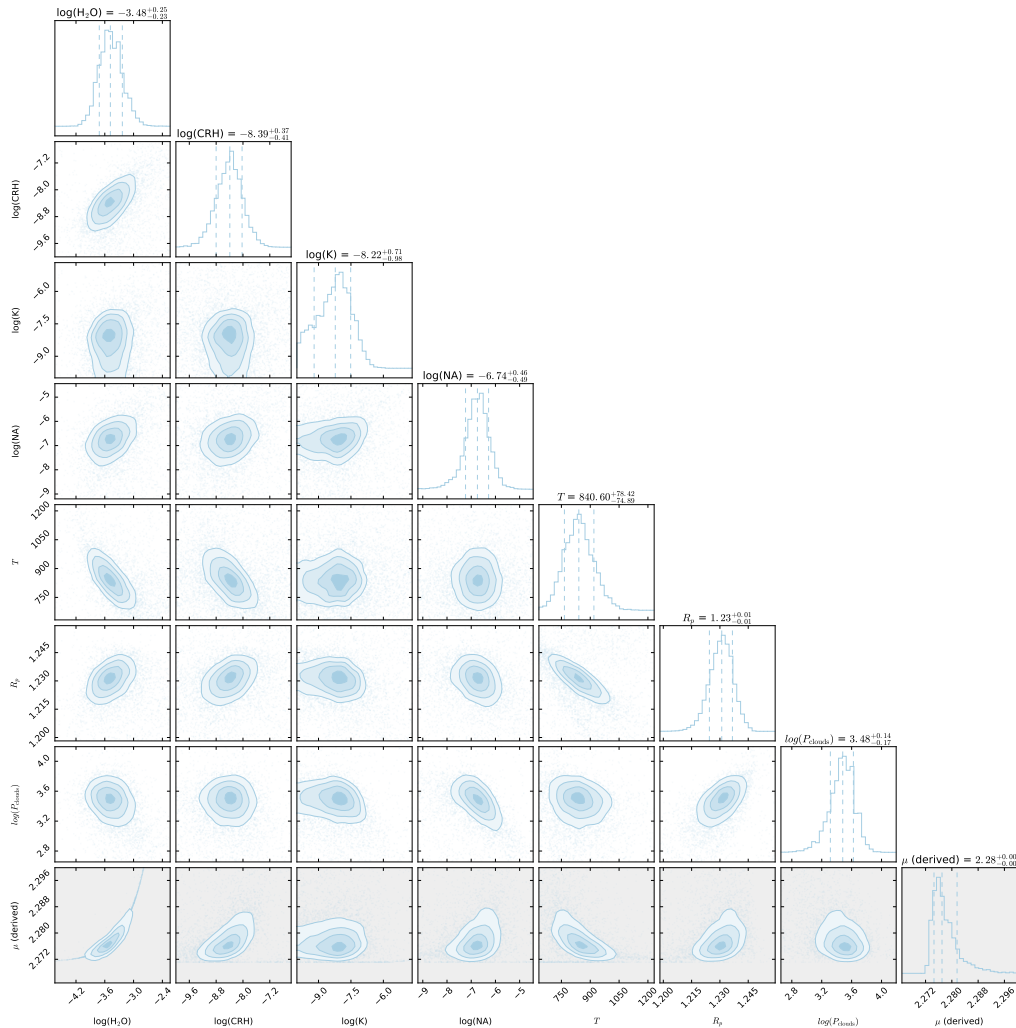
FIGURE 3.3: Posterior distributions of the retrieval for WASP-39b.

3.2 Other spectral signatures

For each planet in our sample, the same procedure has been followed to determine the best-fitting model out of the trials done here. The resulting model fits and the spectra they are describing can be seen in Figure 3.4 for the planets with coverage by STIS, WFC3 and Spitzer (but note that WASP-52 b and WASP-6b lack coverage by WFC3) and in Figure 3.5 for the planets with observations from WFC3 only. The spectra of the majority of the planets in our sample show a statistically significant signature of at least one atmospheric species and the wide diversity of exoplanetary spectra is also evident. In what follows, some noteworthy outcomes will be discussed individually, before summarizing the retrieval outcomes for the complete sample. When a plot for a specific planet (model comparisons, posterior distributions or individual opacity contributions) is not included in this Chapter, it can be found in Appendix A.
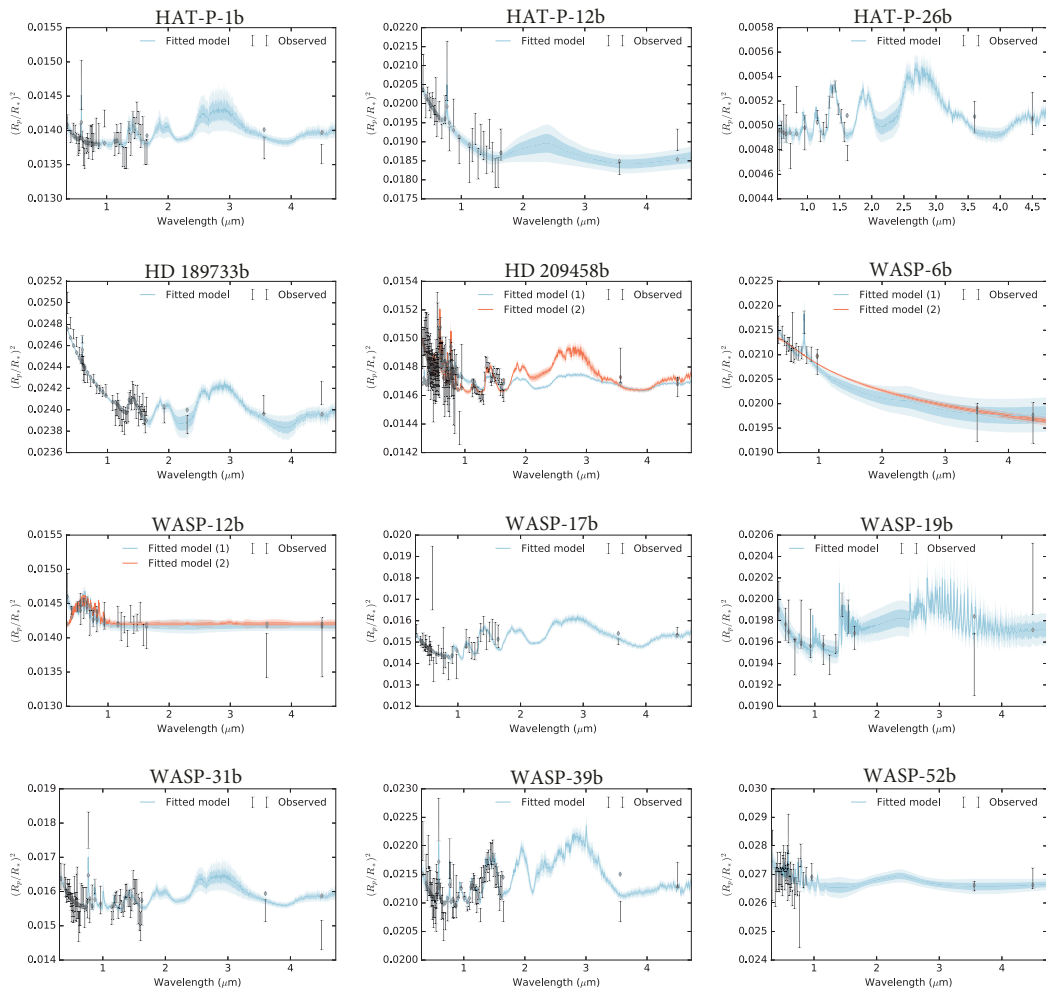

FIGURE 3.4: Spectra and model fits of the planets for planets observed by STIS, WFC3 and Spitzer. Note that WASP-52b and WASP-6b lack observations by WFC3.
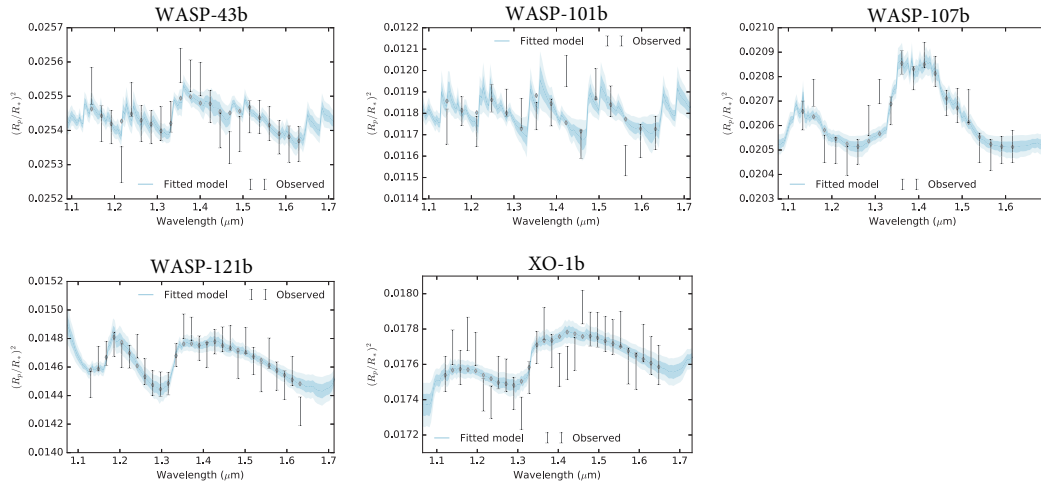
FIGURE 3.5: Spectra and model fits of the planets that are only observed by WFC3.

3.2.1 WASP-19b

The retrieval of WASP-19b resulted in a preference to include either OH or H_2O, as can be seen from the cyan dots in the model comparison in Figure 3.6. The exact Detection Significances over the flat model are 5.77 for OH and 4.67 for H_2O. The fact that both OH and H_2O have a signature around $1.4\mu m$ combined with the limited coverage of WASP-19b (Figure 3.4) make distinguishing between the chemical species difficult in this case. Furthermore, the inclusion of both OH and H_2O is not statistically significant as can be seen from the middle row in Figure 3.6. Although the evidence is weak at only $\sim 2.1\sigma$ according to Jeffreys' scale, there is a preference for the model containing only OH and this model was chosen for further analysis. WASP-19b's spectrum in Figure 3.4 then illustrates the absorption signatures of OH and the feature showing similarities to water absorption is seen around $1.4\mu m$.
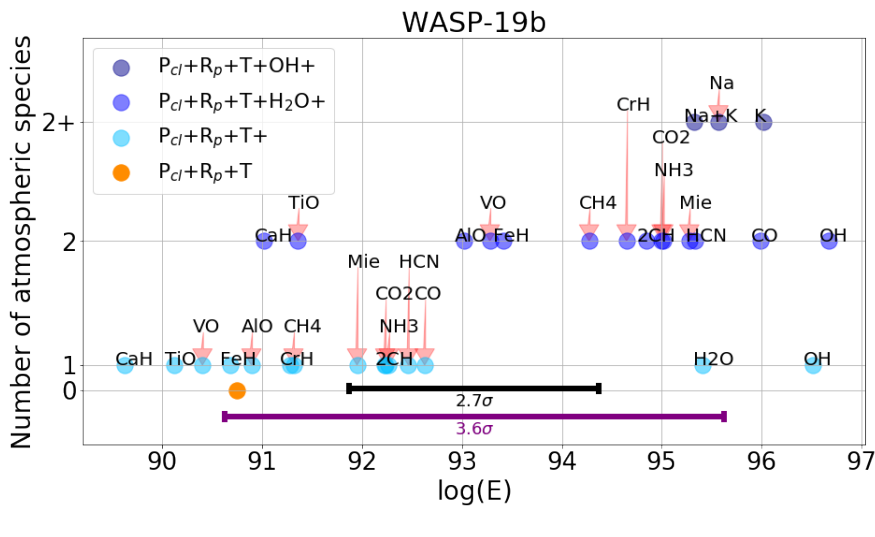

FIGURE 3.6: Model comparison WASP-19b, see caption of Figure 3.1.

3.2.2 WASP-31b

WASP-31b offers better coverage in especially the optical and NIR part, which makes the characterisation a bit more detailed. The comparison between different models can be seen in Figure 3.7 and leads to some interesting results. Including only a single molecule (cyan

dots) gives the highest evidence for H_2O (DS=5.16) and CrH (DS=6.04). Choosing between them on a statistical basis is therefore difficult but, in this case, we are saved by more complexity. The blue dots in the third row of Figure 3.7 illustrate that a model including both H_2O and CrH leads to an even higher evidence, being $\sim 2.7\sigma$ and $\sim 3\sigma$ significant over the CrH-only and H_2O-only models respectively. Increasing one more stage in complexity it can be seen from the dark blue dots that adding K has a Detection Significance of 1.34 as compared to the model without K. Therefore, these observations of WASP-31b show statistically significant signatures of H_2O, K and CrH. Especially the latter molecule is an interesting outcome which will be further discussed in the next chapter.
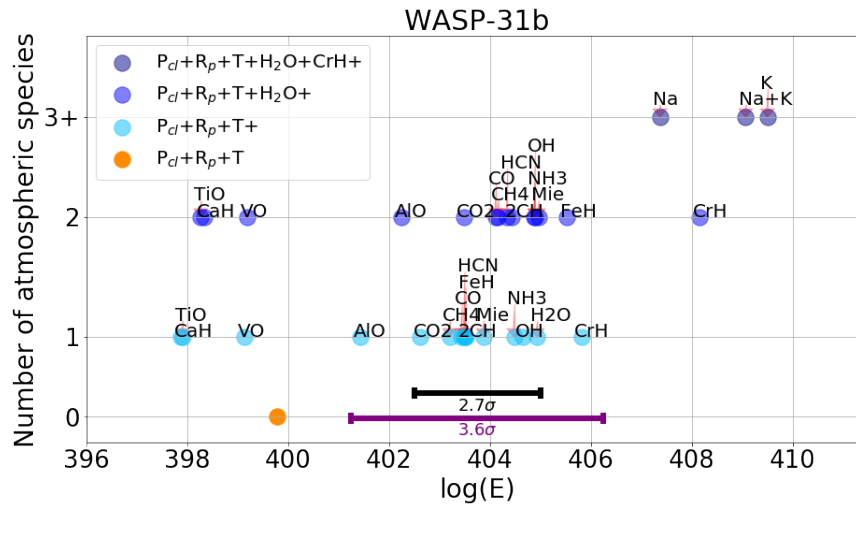
FIGURE 3.7: Model comparison WASP-31b, see caption of Figure 3.1.

3.2.3   WASP-43b

Recently, the first aluminium oxide (AlO) detection was made in WASP-43b (Chubb et al., 2020c). The analysis done here confirms this result: the signature of AlO is found with Detection Significances of 4.64 while the addition of H_2O leads to an even higher DS=7.00 as compared to the flat model. The spectrum of WASP-43b shows the clear signatures that are caused by the presence of AlO. Since this is one of the planets only observed by WFC3, the signatures of Na and K fall outside its covered wavelength range and thus are not included in the retrievals.

FIGURE 3.8: Model comparison WASP-43b, see caption of Figure 3.1. Note that the retrievals including Na and K are absent since this planet lacks optical coverage.

3.2.4 WASP-101b
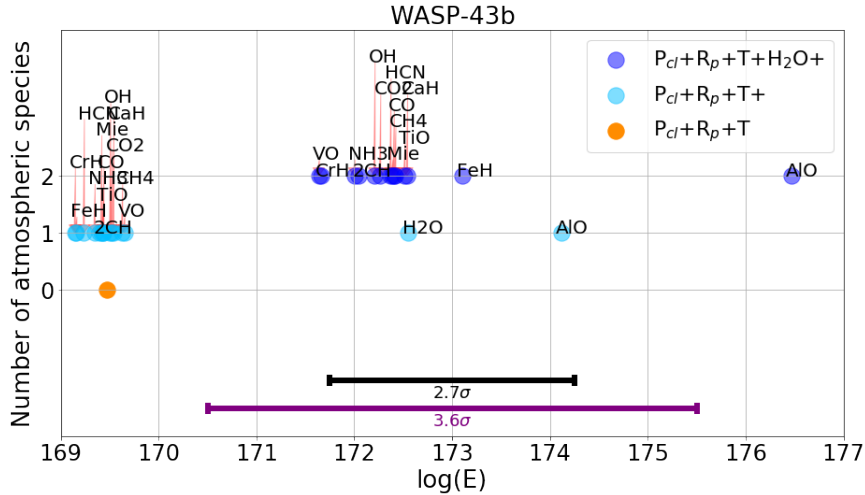
On top of this confirmation of the presence of AlO in WASP-43b we found the first tentative evidence for AlO signatures in WASP-101b, as the model comparison in Figure 3.9 shows. Since the posterior distributions of the initial retrievals indicated that the temperature of WASP-101b was lower than the initial boundary of 886K, the prior was changed to allow the retrieval to converge to a lower temperature. The resulting evidences then led to a slightly higher DS=1.21 for the inclusion of AlO, as denoted by the 'low T' points in Figure 3.9. Although this corresponds to weak evidence for a detection, with only 2.2σ confidence, out of the trials done here it offers the best fit to the data. This highest evidence retrieval resulted in T=660^{+430}_{-176}K, which confirmed the suspicion that the initial prior was not flat enough to include the temperature of the planet.
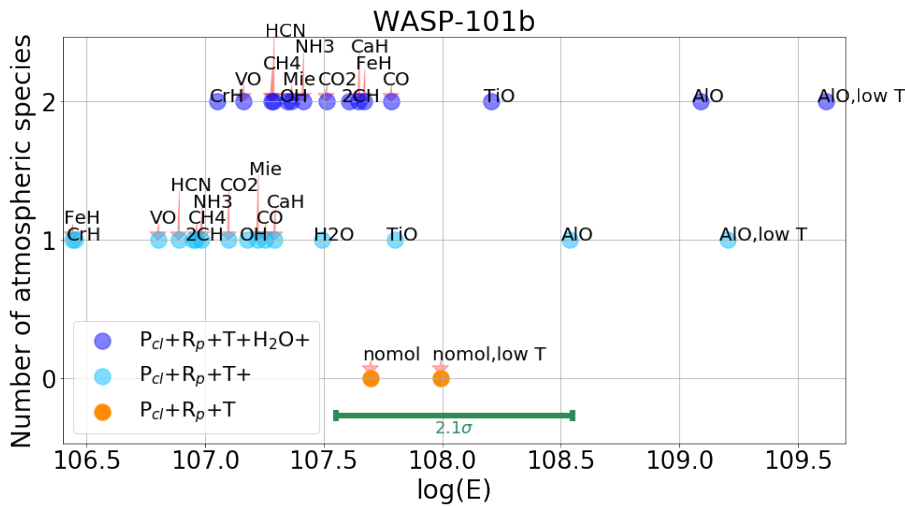

FIGURE 3.9: Model comparison WASP-101b, see caption of Figure 3.1. The labels with 'low T' indicate additional retrievals performed using a lower temperature boundary in the prior. Note that the retrievals including Na and K are absent since this planet lacks optical coverage.

3.2.5   WASP-121b

Even though WASP-121b has only been observed using WFC3, the spectrum seems to include some distinctive signatures of multiple chemical species already. For the single molecule models, the cyan dots in Figure 3.10 shows that the inclusion of H_2O gives a DS=9.64, corresponding to a confidence in the detection of about 4.6σ. The models containing two chemical species are shown in the upper row and illustrate the preference for a model including both H_2O and VO with DS=15.31, as compared to the flat model. The inclusion of H_2O and VO is also preferred over all the other models, with at least 2.5σ.
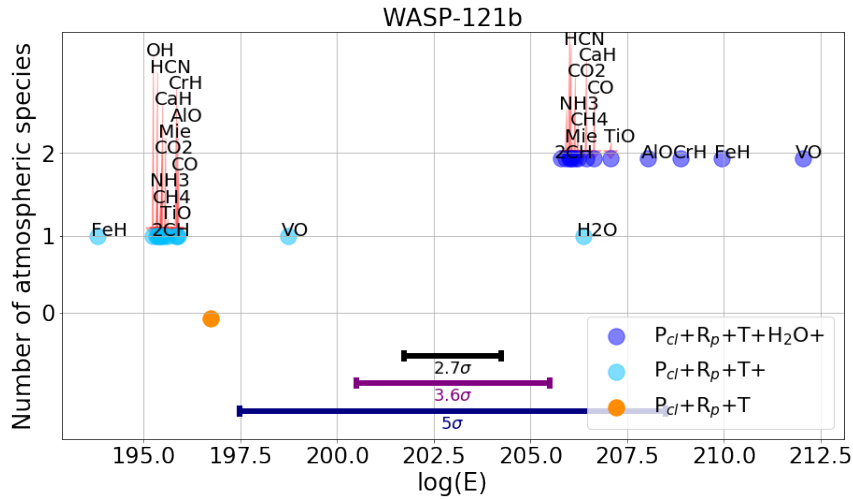
FIGURE 3.10: Model comparison WASP-121b, see caption of Figure 3.1. Note that the retrievals including Na and K are absent since this planet lacks optical coverage.

3.2.6   XO-1b

For XO-1b the upper temperature boundary for the prior was calculated at 1371K. However, the posterior distributions of the initial retrievals seemed to converge to values that were exceeding the upper temperature boundary. Increasing the upper boundary to 3000K resulted in higher evidences, as can be seen from the points with 'hiT' labels in Figure 3.11. After trying several of the apparently highest evidence models, it can be concluded that the model including only H_2O provides the best fit to the data, with a DS=10.90 or ~5σ confidence over the flat model. The final retrieved temperature of 2120K confirmed the suspicion of a temperature exceeding the initial boundary. With a DS=0.95 there is a hint for the addition of CrH to the H_2O only model but, following Jeffreys' scale, this is inconclusive as of now.

FIGURE 3.11: Model comparison XO-1b, see caption of Figure 3.1. The labels denoting 'hiT' represent the additional retrievals that were performed under a higher upper temperat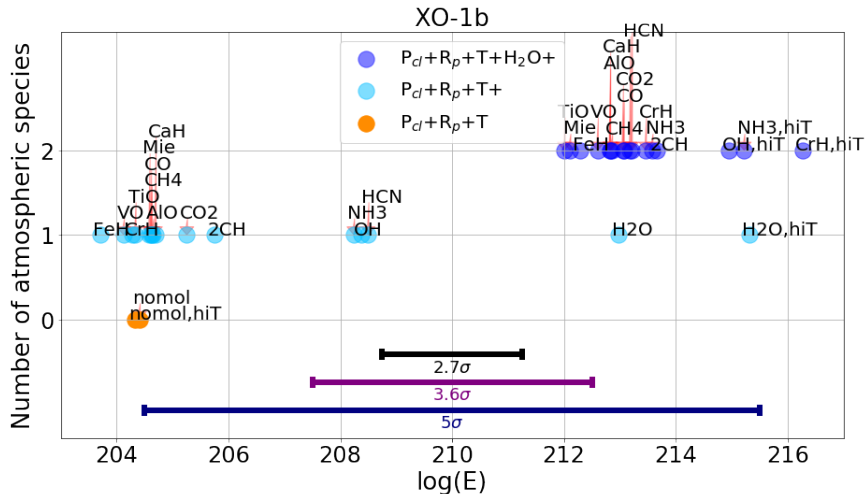ure boundary in the prior. Note that the retrievals including Na and K are absent since this planet lacks optical coverage.

3.2.7 Mie Scattering

The spectra of HAT-P-12b, HD 189733b and WASP-6b in Figure 3.4 have in common that they show an increasing transit depth at shorter wavelengths. As explained in Section 2.2.4, such a slope can be caused by the scattering of light by atmospheric particles that are much smaller than the wavelength of the light and is known as Rayleigh scattering, causing a λ^{-4} dependence. However, the slopes in these spectra are less dependent on wavelength and seem to be better explained by a λ^{-2} to $\lambda^{-0.5}$ dependence. It can be seen from the model comparison for HD 189733b in Figure 3.12 that its spectrum results in a high preference for the inclusion of Mie scattering. Mie scattering and its parametrization in TauREx were also introduced in Section 2.2.4. It is caused by atmospheric particles of about the same size of the wavelength of the incoming light and can be seen as a consequence of clouds/hazes. For particles that have about the same size as the wavelength, scattering is more enhanced in the forward direction. This is described by Mie theory and has a weaker dependence on wavelength than Rayleigh scattering.

The Mie scattering slope in the spectrum of HAT-P-12b is preferred with DS=68.68 over the flat model, even though earlier studies ruled out the presence of a scattering slope (Mallonn et al., 2015). For WASP-6b, the inclusion of Mie scattering is preferred with a DS=11.65 as compared to the flat model, but the detection is debatable since the absence of NIR data points gives a very strong dependence of the slope on the Spitzer data points at 3.6 and 4.5μm. The slope caused by Mie scattering in HD 189733b is found with a high statistical confidence (DS=488.17) and has been detected before (Lecavelier Des Etangs et al., 2008b). For all of these planets, Mie scattering is a part of the models that are chosen for further analysis. To illustrate the effect of Mie scattering, Figure 3.13 shows the individual opacity contributions of the different components included in the atmospheric model of HD 189733b. It can be seen from the purple line that the addition of Mie scattering provides an adequate fit to the observed slope in the spectrum and shows stronger absorption than the brown slope caused by Rayleigh scattering.
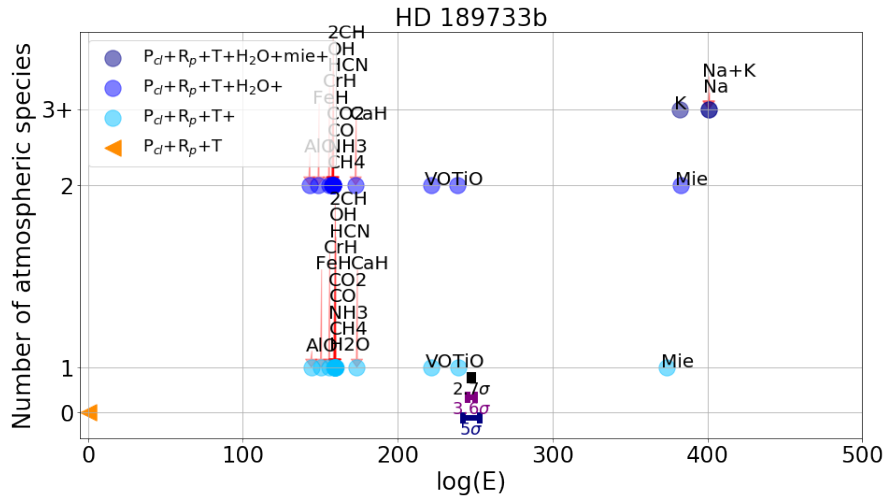
FIGURE 3.12: Model comparison HD 189733b, see caption of Figure 3.1. From its high evidence it can clearly be seen that Mie scattering is an important opacity source to explain the spectrum.
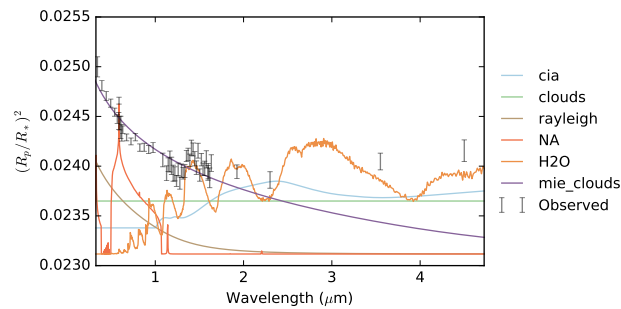

FIGURE 3.13: Individual opacity contributions HD 189733b. The slope caused by Mie scattering is prominently visible as the purple line.

3.2.8 Multimodal solutions

The spectrum of HD 209458b stands out compared to the other spectra in Figure 3.4, due to the fact that a purely statistical analysis results in two models giving an equally adequate fit to the observations. The posterior distribution shown in Figure 3.14 shows us that these models have a large difference in the retrieved abundances. For the purpose of searching for chemical trends, a reliable estimate of the abundance is needed and, therefore, we need to make an informed decision on which of the retrieval outcomes to use. This can be done by comparing them to the expectations that follow from models of equilibrium chemistry (Woitke et al., 2018). In the case of HD 209458b the decision can be based on the retrieved abundances of Na and K. The blue model is retrieved with mixing ratios equal to $\log(Na)=-0.15$ and $\log(K)=-0.63$, which greatly exceeds the expected abundances from equilibrium chemistry of up to 10^{-6} and 10^{-7} for Na and K respectively. Even though deviations from this are possible in H-poor planetary atmospheres, Hot Jupiters are assumed to be H-dominated. Therefore, the extremely high abundances of the blue model can be seen as unrealistic and the red model can be chosen as the best fit to the observations.
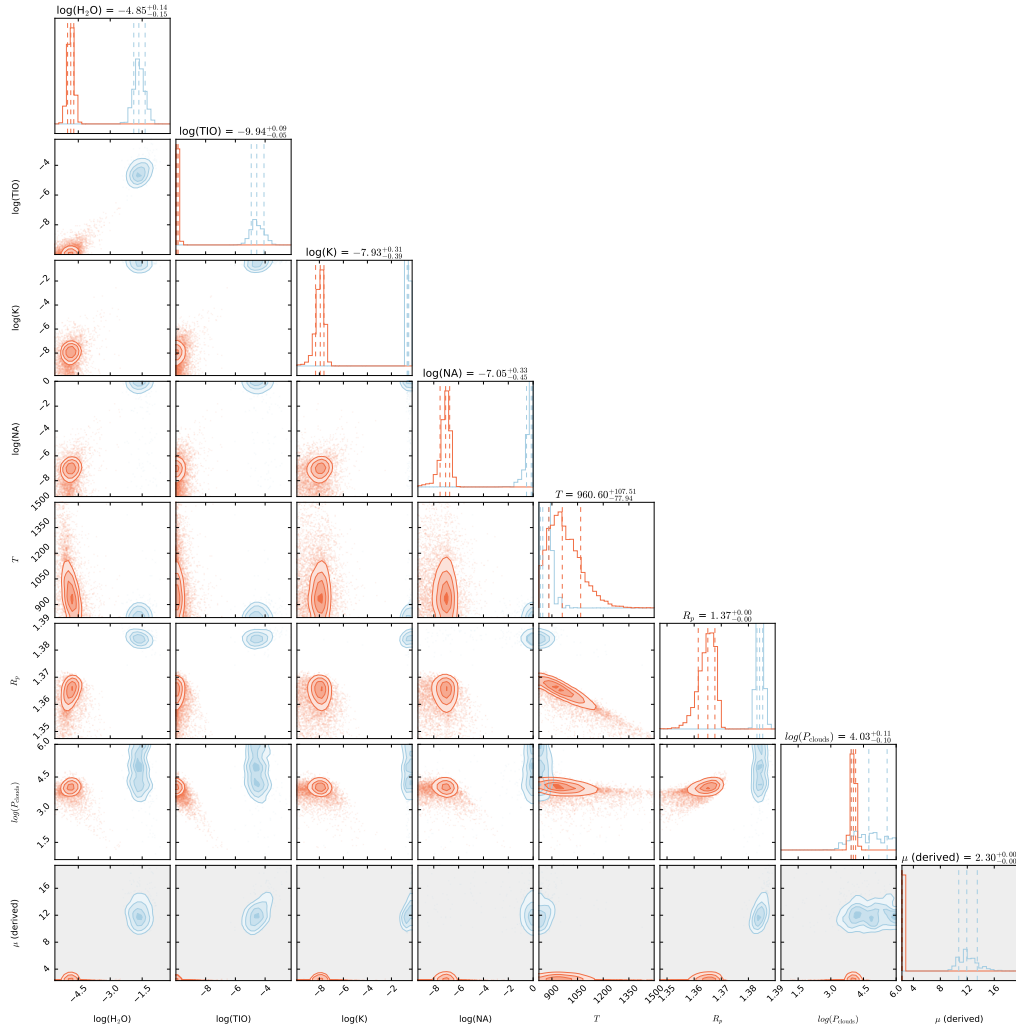
FIGURE 3.14: Posterior distributions of the retrieval for HD 209458b.

The same argument can be used to decide between the retrieved models for WASP-6b. For this planet, mixing ratios of respectively $\log(K)=-3.30$ and -7.08 are found as solutions of the best-fitting atmospheric model, as can be seen in Figure A.14. Based on the equilibrium chemistry predictions it can be said that the latter of these models provides the most realistic abundance and therefore, the outcomes of this model will be used in further analysis.

Lastly, a multimodal solution is also found for WASP-12b. To determine the most realistic solution its posterior distributions in Figure A.17 are used. Around the temperatures of WASP-12b, Woitke et al. (2018) show that TiO is not the main Ti-bearing species and that, regardless of the exact temperature, the expected abundance of TiO never exceeds values of $\sim 10^{-7}$. Hence, it can be said that the high mixing ratio of $\log(\text{TiO})=-1.20$ from the red model is physically unrealistic and the blue model is chosen as the best fit. Further discussion on the spectrum of WASP-12b can be found in Section 5.1.

3.3 Atmospheric chemistry

Having determined the model with the highest evidence for each of our planets, Table 3.1 summarizes per planet the detected molecules along with their retrieved abundances and Detection Significance DS (Equation 2.18). DS is given with respect to the flat model without chemical signatures. For example, the DS of HAT-P-1b illustrates that the inclusion of H_2O is preferred with a confidence of DS=1.52 or $\sim 2.2\sigma$ as compared to a model without any chemical species. Further to the right in the table, we can see that the model containing H_2O

as well as Na is preferred with a confidence of DS=2.22 or $\sim2.5\sigma$ as compared to the flat model. This statistical preference for the addition of Na over the H_2O-only model is too small to be significant according to Jeffrey's scale. Nevertheless, as said before, the alkali metals Na and K have such specific signatures that this is still regarded as a significant detection. Note that whenever the Table gives multiple chemical detections for a planet, the Detection Significance is given for the model containing the specific species, in addition to any other species that is already specified in columns that are more to the left.

TABLE 3.1: Retrieved chemical abundances: planets below the line only have WFC3 coverage, planets above also have Spitzer and/or STIS.

Planet	log(H_2O)	DS^a	Other molecule i^b	log(i)	DS^a	log$(Na)^c$	DS^a	log$(K)^c$	DS^a	T(K)
HAT-P-1 b	$-4.87^{+0.77}_{-1.94}$	1.52	-	-	-	$-7.65^{+1.18}_{-1.24}$	2.22	-	-	1120^{+332}_{-260}
HAT-P-12 b	-	-	-	-	-	-	-	$-6.54^{+1.53}_{-1.43}$	68.91^d	925^{+104}_{-101}
HAT-P-26 b	$-3.10^{+1.19}_{-0.65}$	40.60	-	-	-	-	-	-	-	657^{+87}_{-52}
HD 189733 b	$-4.63^{+0.73}_{-0.46}$	265.11	-	-	-	$-5.40^{+1.51}_{-0.90}$	506.65^d	-	-	1469^{+6}_{-13}
HD 209458 b	$-4.85^{+0.14}_{-0.15}$	92.16	TiO	$-9.94^{+0.09}_{-0.05}$	115.62	$-7.05^{+0.33}_{-0.45}$	116.15	$-7.93^{+0.31}_{-0.39}$	122.70	961^{+107}_{-78}
WASP-6 b	-	-	-	-	-	-	-	$-7.08^{+1.72}_{-1.80}$	12.48^d	902^{+100}_{-67}
WASP-12 b	-	-	TiO	$-9.07^{+1.28}_{-0.61}$	8.29	-	-	-	-	1179^{+1023}_{-454}
WASP-17 b	$-3.99^{+0.28}_{-0.23}$	25.04	-	-	-	-	-	-	-	1315^{+71}_{-94}
WASP-19 b	-	-	OH	$-2.37^{+0.75}_{-0.79}$	5.77	-	-	-	-	1534^{+380}_{-253}
WASP-31 b	$-5.40^{+0.37}_{-0.42}$	5.16	CrH	$-8.49^{+0.62}_{-0.62}$	8.38	-	-	$-7.63^{+0.75}_{-0.87}$	9.72	1483^{+264}_{-344}
WASP-39 b	$-3.48^{+0.25}_{-0.23}$	68.88	CrH	$-8.39^{+0.37}_{-0.41}$	73.63	$-6.74^{+0.46}_{-0.49}$	80.78	$-8.22^{+0.71}_{-0.98}$	81.23	841^{+78}_{-75}
WASP-52 b	-	-	VO	$-9.18^{+1.07}_{-0.49}$	3.41	$-7.61^{+1.58}_{-1.27}$	4.05	-	-	752^{+295}_{-222}
WASP-43 b	$-3.58^{+1.22}_{-1.23}$	3.08	AlO	$-5.16^{+1.66}_{-1.56}$	7.00	n/a^e	n/a	n/a	n/a	957^{+226}_{-129}
WASP-101 b	-	-	AlO	$-6.23^{+2.46}_{-1.30}$	1.21	n/a	n/a	n/a	n/a	1141^{+325}_{-182}
WASP-107 b	$-2.089^{+1.31}_{-1.76}$	40.94	-	-	-	n/a	n/a	n/a	n/a	533^{+133}_{-76}
WASP-121 b	$-1.36^{+0.31}_{-2.59}$	9.64	VO	$-4.22^{+0.58}_{-2.54}$	15.31	n/a	n/a	n/a	n/a	1476^{+162}_{-75}
XO-1 b	$-0.82^{+0.18}_{-0.21}$	10.90	-	-	-	n/a	n/a	n/a	n/a	2120^{+433}_{-391}

^{a} Detection Significance over flat model

^{b} If the planet has a significant H_2O detection, molecule i is in addition to it

^{c} If the planet has other chemical detection(s), alkali Na and/or K is in addition to it

^{d} Also opacity due to mie scattering included (see Section 3.2.7)

^{e} n/a due to lack of optical coverage

3.3.1 H_2O

H_2O is the most frequently detected signature in our sample, which is not surprising given the fact that it has a prominent signature inside the spectral regime (around 1.4μm; shown in Figure 2.4). As can be seen in Table 3.1, the signature has been found to be significant for 11 of the 17 planets. The Detection Significance greatly varies over our sample, ranging from $\sim2.2\sigma$ to greatly exceeding 5σ, and part of this range might also be explained by the opacity caused due to the inclusion of Rayleigh and CIA. The effect of these sources of opacity is briefly explained in Section 3.1. Our results then indicate a contrast: the planets with coverage by STIS, WFC3 and Spitzer generally show lower abundances, compared to those derived from WFC3-only observations. For the latter group, most notably for WASP-121b and XO-1b, the abundances are relatively high. A broader wavelength coverage, especially the inclusion of both optical and IR, allows us to break degeneracies between cloud properties and/or temperatures on one hand and gas abundances on the other (Griffith, 2014; Heng et al., 2017) and, therefore, the abundances retrieved from WFC3-only spectra have to be interpreted with great caution.

3.3.2 Alkali metals

The alkali metals Na and K have a strong absorption signature in the optical, as said in Section 2.4.2. Both for Na and K, signatures have been detected in the spectra of 5 planets that have optical measurements available from STIS. HD 209458b and WASP-39b show signs of the presence of both Na and K, while the other planets hint towards the signature of

one of them. HAT-P-12b, HD 189733b and WASP-6b have a particularly high DS for the inclusion of Na and/or K over the flat model, but a large fraction of this DS is also resulting from the inclusion of the optical slope caused by Mie scattering (see Section 3.2.7). Table 3.2 shows the Detection Significances of the Mie scattering opacities in these planets and it can be seen that the addition of the alkali metals in the best model only results in slightly higher evidences. Nevertheless, for the alkali metals, even a small decrease in evidence is regarded as significant.

Planet	DS Mie scattering	DS best model
HAT-P-12b	68.68	68.91
HD 189733b	488.17	506.65
WASP-6b	11.65	12.48

TABLE 3.2: For the planets that required the opacity by Mie scattering to explain their spectrum, the Detection Significance of the Mie scattering model (for HD 189733b it represents H_2O+Mie scattering) is compared to that of the best model.

3.3.3 Other species

Evidence for TiO has been found in the spectra of HD 209458b and WASP-12b. With absorption signatures in a similar regime, VO was detected for WASP-52b and WASP-121b. The high temperatures of Hot Jupiters are thought to imply the presence of both species and their signatures are mostly seen in the regime $0.4-1.0\mu m$ (Fortney et al., 2008). The exact shapes of these absorption signatures can be seen in Figure A.18 for TiO and Figure A.28 for VO. In a hydrogen-dominated atmosphere, the extremely high value associated with the VO detection on WASP-121b (log(VO)$=-4.22^{+0.58}_{-2.54}$) might again be seen as implausible from a physical perspective, since equilibrium chemistry would expect at most 10^{-8} for any V-bearing species (Woitke et al., 2018).

Signatures of another oxygen-bearing species were found in the spectra of WASP-43b and WASP-101b, in the form of AlO. The distinctive signatures caused by this molecule can clearly be identified in the spectrum of WASP-43b, as shown in Figure 3.15. The abundances are again rather high and will be further discussed in Section 4.3. Finally, the retrievals conducted here hint towards the first detections of CrH in the atmospheres of WASP-31b and WASP-39b. As can be seen from Figure 3.2b (and for WASP-31b in A.25), this species has multiple features in the range of 0.7 to $1.5\mu m$.
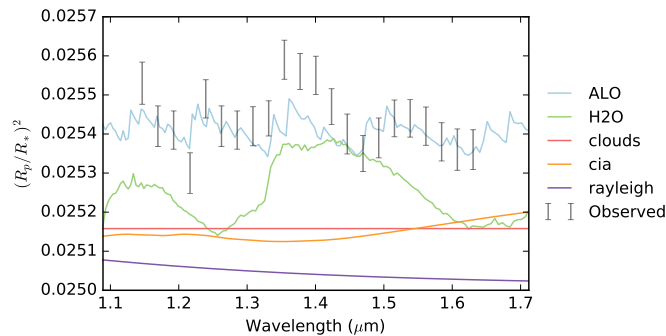

FIGURE 3.15: The opacity contributions for each of the parameters in the highest evidence model for WASP-43b.

Chapter 4

Discussion

This Chapter is initiated by a comparison with earlier retrieved abundances, before investigating the possible existence of chemical trends. These chemical trends are then discussed in light of several disequilibrium processes and the dependence on formation conditions. Afterwards, systematic errors that might influence our retrieval results are discussed. The Chapter is ended by providing prospects for the spectral regime offered by JWST.

4.1 Earlier Detections

It is important to emphasize that the results, as presented in the last chapter, are based on the atmospheric models that turned out to be the best fit to the spectral data of each of the planets. In other words, the best fit out of the model trials performed in this analysis and assuming the simplified atmospheric representation in TauREx. Excluding a particular chemical species from the atmospheric model means that the spectroscopic signature has not been detected on the basis of statistics. This does not necessarily mean that a chemical species is completely absent from the planetary atmosphere probed. Instead, the signatures of a species can also fall outside of the observed spectral range, be too weak to be detected or overlap with other spectral signatures. The signature of water was clearly detected for many of the planets and a comparison with earlier detections can be insightful.

4.1.1 Water

All of the planets in our sample have been analysed before, sometimes using the same observations. This naturally provides us with the opportunity to compare our results to those of earlier studies. Although many studies of individual exoplanets have been conducted (e.g. HD 189733b (Pont et al., 2008), HAT-P-1b (Nikolov et al., 2014), WASP-121b (Evans et al., 2016)), the comparison of the retrieved water abundances from this study has been limited to other comparative studies. The reason for this is twofold: firstly, the majority of our sample was included in these comparative studies and resulted in water detections to compare with. Besides that, the homogeneous retrievals done as part of comparative studies make it more feasible to compare results. Besides the studies used for comparison in the following tables, other comparative studies have been done using WFC3-only spectra (Fisher et al., 2018) and with coverage from the UV to the IR (Barstow et al., 2017; Sing et al., 2016), but these latter two do not explicitly report chemical abundances.

Table 4.1 gives a comparison for the water abundances as retrieved by different studies. It is important to note that T18 (Tsiaras et al., 2018) only made use of the WFC3 spectra in their analysis. As said before, broader coverage may be needed to break degeneracies between gas abundances and planet radius or cloud coverage (Heng et al., 2017), possibly leading to different retrieval results. Nevertheless, we can still compare the results of our WFC3-only planets with those of (Tsiaras et al., 2018) and from this it can be seen that more realistic values are retrieved by Tsiaras et al. (2018) for WASP-121b and XO-1b. For both planets, this can be explained by the fact that their models contain more opacity sources (CH_4, CO, CO_2, NH_3, TiO, H_2O and VO). Our models are limited to the species that have significant detections: H_2O for XO-1b and H_2O and VO for WASP-121b. For XO-1b, the inclusion of for example NH_3 can greatly influence the retrieved water abundance, as it has signatures just rightward of the H_2O peak at 1.4μm. Nevertheless, Figure 3.11 tells us that even though

TABLE 4.1: log(H_2O) of other studies: n/a means planet was not included, - means no significant detection.

Planet	T18	W19	P19	This analysis
HAT-P-1b	-2.68±1.22	$-2.54^{+0.75}_{-0.67}$	$-2.72^{+0.42}_{-0.56}$	$-4.87^{+0.77}_{-1.94}$
HAT-P-12b	-3.61±1.48	$-5.70^{+1.22}_{-3.36}$	-	-
HAT-P-26b	-3.32±1.10	$-1.83^{+0.46}_{-0.57}$	n/a	$-3.10^{+1.19}_{-0.65}$
HD 189733b	-2.51±0.90	$-4.66^{+0.35}_{-0.33}$	$-5.04^{+0.46}_{-0.30}$	$-4.63^{+0.73}_{-0.46}$
HD 209458b	-3.19±0.87	$-4.54^{+0.33}_{-0.27}$	$-4.66^{+0.39}_{-0.30}$	$-4.85^{+0.14}_{-0.15}$
WASP-6b	n/a	-	-	-
WASP-12b	-3.12±0.92	$-3.23^{+1.42}_{-0.80}$	$-3.16^{+0.66}_{-0.69}$	-
WASP-17b	n/a	$-3.84^{+1.27}_{-0.51}$	$-4.04^{+0.91}_{-0.42}$	$-3.99^{+0.28}_{-0.23}$
WASP-19b	n/a	$-3.43^{+0.47}_{-0.52}$	$-3.90^{+0.95}_{-1.16}$	-
WASP-31b	-3.84±1.90	$-4.55^{+1.77}_{-4.33}$	$-3.97^{+1.01}_{-2.27}$	$-5.40^{+0.37}_{-0.42}$
WASP-39b	-5.94±0.61	$-0.65^{+0.14}_{-1.83}$	$-4.07^{+0.72}_{-0.78}$	$-3.48^{+0.25}_{-0.23}$
WASP-52b	-4.09±0.87	n/a	n/a	-
WASP-43b	-4.36±2.10	$-3.68^{+0.92}_{-0.88}$	n/a	$-3.58^{+1.22}_{-1.23}$
WASP-101b	-	n/a	n/a	-
WASP-107b	n/a	$-2.87^{+0.95}_{-0.73}$	n/a	$-2.089^{+1.31}_{-1.76}$
WASP-121b	-3.05±0.87	n/a	n/a	$-1.36^{+0.31}_{-2.59}$
XO-1b	-2.75±1.64	n/a	n/a	$-0.82^{+0.18}_{-0.21}$
Mean	-3.53 ± 0.95	-3.46 ± 1.38	-3.95 ± 0.74	-3.47 ± 1.50

*T*18: WFC3-only spectra, Tsiaras et al. (2018)
*W*19: Welbanks et al. (2019)
*P*19: Pinhas et al. (2019)

there are hints towards the inclusion of NH_3 (or CrH), this inclusion is statistically not yet significant using the current spectral range. Wider coverage might provide proof for this inclusion and will be further discussed in Section 4.6. Signatures of VO and/or TiO are also found in WASP-121b by Tsiaras et al. (2018).

The lower abundance we find for HAT-P-1b is probably caused by the difference in reference radius. As can be seen from the spectrum in Figure 3.4, the lowest transit depth measurements fall somewhat below our best model. The models of Pinhas et al. (2019) and Welbanks et al. (2019) seem to match these low transit depths, consequently resulting in the deduction of stronger signatures and hence higher abundances. For HAT-P-26b, the inclusion of ground-based optical transmission spectra by Welbanks et al. (2019) might explain the different abundances, although the result of this analysis and (Tsiaras et al., 2018) seem more realistic. The lack of a detection of water in WASP-12b here is caused by our analysis of the spectrum from Sing et al. (2013). While this spectrum lacks a clear water signature, more recent WFC3 observations do provide evidence of the water signature (Kreidberg et al., 2015). Besides these clear differences, Table 4.1 also shows several similar results, for example for HD 189733b, HD209458b, WASP-17b and WASP-107b. The non-detection of the water signature in HAT-P-12b is in agreement with Welbanks et al. (2019), while the low abundance of Pinhas et al. (2019) does not necessarily contradict this result. The studies also agree on the non-detection in WASP-6b, mainly explained by a lack of coverage by WFC3 (as is the case for WASP-52b). The bottom row indicates the mean retrieved abundance over this sample for each of the studies and illustrates a remarkable agreement. The results of the remaining planets (WASP-19b, WASP-31b, WASP-39b, WASP-43b, WASP-101b) will be discussed in Section 4.1.3.

4.1.2 Alkali metals

Expanding the comparison towards the alkali metals, Table 4.2 compares the retrieved abundances of the atomic species Na and K. Tsiaras et al. (2018) analyse WFC3-only spectra, which prevents them from detecting the optical signatures of these species and thus also prevents comparison. The first difference that might be noticed from the table is the limited amount of detections made by Pinhas et al. (2019). Although they do not specify the exact source of the line data, usage of different line lists may explain some of the differences in retrievals. Welbanks et al. (2019) use cross-sections based on the same line lists for Na (Allard et al., 2019) and K (Allard et al., 2016).

TABLE 4.2: Comparison to abundances of other studies: n/a means planet was not included, - means no significant detection.

	(A) Sodium (log(Na))			(B) Potassium (log(K))		
Planet	P19	W19	This analysis	P19	W19	This analysis
HAT-P-1b	$-8.44^{+1.45}_{-2.12}$	$-8.58^{+1.20}_{-1.79}$	$-7.65^{+1.18}_{-1.24}$	-	-	-
HAT-P-12b	-	-	-	-	-	$-6.54^{+1.53}_{-1.43}$
HAT-P-26b	n/a	-	-	n/a	-	-
HD 189733b	$-7.77^{+1.64}_{-0.87}$	$-4.19^{+0.67}_{-0.73}$	$-5.40^{+1.51}_{-0.90}$	-	$-5.54^{+0.49}_{-0.44}$	-
HD 209458b	-	$-5.47^{+0.61}_{-0.48}$	$-7.05^{+0.33}_{-0.45}$	-	$-7.00^{+0.59}_{-0.49}$	$-7.93^{+0.31}_{-0.39}$
WASP-6b	-	-	-	$-5.53^{+2.01}_{-1.85}$	$-3.22^{+1.21}_{-3.79}$	$-7.08^{+1.72}_{-1.80}$
WASP-12b	-	$-6.64^{+2.13}_{-2.98}$	-	-	-	-
WASP-17b	-	$-8.65^{+1.76}_{-1.67}$	-	-	-	-
WASP-19b	-	$-5.11^{+1.00}_{-1.05}$	-	-	-	-
WASP-31b	-	-	-	-	$-3.48^{+1.38}_{-2.31}$	$-7.63^{+0.75}_{-0.87}$
WASP-39b	$-3.86^{+1.31}_{-1.36}$	$-3.62^{+1.14}_{-2.69}$	$-6.74^{+0.46}_{-0.49}$	$-4.22^{+1.25}_{-1.12}$	$-5.62^{+2.30}_{-2.05}$	$-8.22^{+0.71}_{-0.98}$
WASP-52b	n/a	n/a	$-7.61^{+1.58}_{-1.27}$	n/a	n/a	-

*W*19: Welbanks et al. (2019)
*P*19: Pinhas et al. (2019)

Looking at Table 4.2, our analysis results in the detection of the K doublets for HAT-P-12b. As described in Section 3.2.7, this is only with a DS=0.23 over a model containing only Mie scattering. In this analysis, it was decided to still quantify such a small DS as significant for Na and K, since the signature of K is evident in HAT-P-12b's spectrum in Figure 3.4. Both Pinhas et al. (2019) and Welbanks et al. (2019) adhere to the 2σ or DS$\geq$1 detection threshold for the inclusion of the alkali lines, explaining the absence of a K detection. The discrepancy in the detection of K in HD 189733b can probably be related to different modelling of the scattering slope at lower wavelengths of the planet's spectrum.

Next up, the differences seen in the retrievals of WASP-12b, WASP-17b and WASP-19b need to be explained separately. Our non-detection of Na and instead the inclusion of TiO in WASP-12b seems to reasonably explain the planet's spectrum in the optical regime. The exclusion of TiO in the analysis of WASP-12b by Welbanks et al. (2019) explains their detection of Na at a small DS of 1.58, as can be seen from our analysis as well in Figure A.16. Regarding the analysis of WASP-19b, Welbanks et al. (2019) use a ground-based transmission spectrum, resulting in a highly improved optical coverage. The limited number of data points that have been used in our analysis does not cover the optical part well enough to detect the alkali metals. Finally, the spectrum of WASP-17b clearly shows an observed absorption peak at the wavelengths expected for Na absorption (see Figure 4.1). Including Na in the retrieval does produce its optical signature around 0.59μm but this is not strong enough to explain the huge increase in transit depth that is observed at this wavelength. Therefore, the addition of Na does not lead to an increase in the Bayesian evidence and, hence, there is no statistical preference for this inclusion. For the sake of consistency the detection has been excluded, even though the abundance corresponding to the model in Figure 4.1 (log(Na)=-8.69) seems to match the result of Welbanks et al. (2019) extremely well.
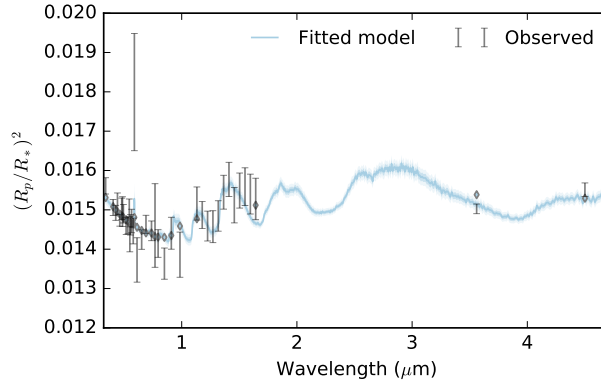
FIGURE 4.1: Transmission spectrum of WASP-17 b and the best fit by the model including H_2O and Na.

There appears to be agreement on the detection of the alkali metals in other planets, albeit with significant differences in retrieved abundances. Besides the different sources of line data, a reason for this is overlap with spectral signatures of other species: many of the species discussed in the next Section show signatures in the same optical regime (such as TiO described above for WASP-12b), leading to possible overlap and, as a consequence, changes in the retrieved abundances.

4.1.3 Other species

Early evidence for the presence of TiO in the atmosphere of HD 209458b was discovered at 10^{-4}–10^{-3} solar abundance by Désert et al. (2008) and our finding of $10^{-3} \times$ stellar abundance agrees well with this. For WASP-12b, our analysis provides evidence for the presence of TiO, whereas earlier dedicated searches ruled out its absorption features (Sing et al., 2013). However, as illustrated by Figure A.16, neither the presence of VO nor Mie scattering due to clouds/hazes can be ruled out statistically in favour of TiO. Besides TiO, another important process providing the opacity of the best fitting model is Rayleigh scattering caused by tiny particles (see Figure A.18). The presence of Rayleigh and/or Mie scattering agrees with the findings of Sing et al. (2013). Evans et al. (2016) also reported evidence for VO (as well as TiO and FeH) in WASP-121b, while Tsiaras et al. (2018) call the presence of VO and TiO in this planet 'suggestive'.

The detection of AlO in the atmosphere of WASP-43b is a confirmation of the discovery of Chubb et al. (2020c). Our retrieved abundance ($\log(AlO)=-5.16^{+1.66}_{-1.56}$; Table 3.1) agrees well with the values of $-5.25^{+2.03}_{-1.87}$ from their retrievals. Moreover, the additional detection of water in our analysis is also consistent with that of Chubb et al. (2020c) (at an abundance of $\log(H_2O)=-3.79^{+1.37}_{-2.74}$) and compared to the other studies in Table 4.1. Hints for the absorption signatures of AlO are also seen in the spectrum of WASP-101b, as described in Section 3.2.4. This planet was already notified as 'scoring highly in terms of potential detections of atmospheric features' by Tsiaras et al. (2018), but quantifying these features turned out to be difficult. The characteristic shape of AlO absorption provides a reasonable fit to the observed spectrum, as is also evident from Figure A.31. Since AlO was not included in earlier retrievals for WASP-101b, the exact abundance can not be compared to earlier results.

WASP-19b seems to be a peculiar case as compared to the retrieval outputs of the other planets, with hints for the detection of OH. As described in Section 3.2.1, the detection of OH only has a small statistical preference over H_2O, which is not surprising given the limited amount of data points covering this planet's spectrum and the similarities in the (low-resolution) spectral behaviour of H_2O and OH around $1.4\mu m$. More measurements in the spectral ranges of STIS and/or WFC3 will probably already tell us a lot more about the exact cause of the opacities. Nevertheless, further distinguishing the two species through wider wavelength coverage will be further discussed in Section 4.6.

Lastly, Table 3.1 shows that the retrievals also result in the detection of CrH for WASP-31b and WASP-39b. As described in Section 3.2.2, the model that includes CrH in the atmosphere of WASP-31b is significant over any other model. For WASP-39b, the model containing H_2O and CrH is slightly preferred over one with H_2O and NH_3. Since earlier retrievals did not include CrH in the analysis, comparing the retrieved abundances to earlier findings is not possible. However, the detections of CrH naturally follow the presence of the molecule in the atmospheres of brown dwarfs (Burrows et al., 2001; Kirkpatrick et al., 1999). Where comparison to earlier detections is not possible, the retrieved abundances can still be compared to predictions from thermochemical equilibrium calculations.

4.2   Chemical trends

With the chemical detections in perspective to other findings, the model providing the highest Bayesian Evidence is then chosen for further analysis, thus including the detections as listed in Table 3.1. Since the majority of the chemical detections concern water, this is naturally the first target to search for possible trends. To be able to quantify the resulting abundances we have to look at the ratios of different species. By definition, the sum of the different chemical components in an atmosphere is equal to 1, or:

$$[H_2] + [He] + \sum[i] = 1 \tag{4.1}$$

The term $\sum[i]$ represents the mixing ratios of all the different gases that might be present in an atmosphere. For Hot Jupiters, we assume an atmosphere that is dominated by Hydrogen and Helium, with a ratio $\frac{[He]}{[H_2]} = \frac{0.15}{0.85} = 0.176$. Hence, Equation 4.1 can be rewritten as:

$$1.176[H_2] = 1 - \sum[i] \tag{4.2}$$

Based on the retrieved abundances in Table 3.1 the contributions by other trace gases can assumed to be negligible, so that we have:

$$[H_2] = \frac{1 - [H_2O]}{1.176} \tag{4.3}$$

Using this, we can define the planetary $[H_2O/H_2]$ abundance ratio:

$$[H_2O/H_2] = \frac{1.176[H_2O]}{1 - [H_2O]} \tag{4.4}$$

4.2.1   Thermochemical

As the first possibility for a trend, the dependence of the planetary $[H_2O/H_2]$ abundance on the planetary temperature may be investigated. To be able to interpret the retrieved abundances, a reference abundance is needed. Assuming a solar initial composition (Asplund et al., 2009), this reference abundance has been calculated as a function of temperatures assuming equilibrium chemistry at a pressure of 1 bar by Woitke et al., 2018. For temperatures below $\sim$1200K, the majority of O is expected to be in H_2O, leading to an expected abundance of $\log(H_2O) \sim -3$. For temperatures above $\sim$1200K, half of O is expected in H_2O (the other half being in CO) and the abundance is expected to be $\log(H_2O) \sim -3.3$ (see also Madhusudhan (2012)). Between these two regimes, there is a transition region, as shown by the decrease in the expected abundance around 1200K. The retrieved exoplanetary abundances can be compared to the predictions from equilibrium chemistry as seen in Figure 4.2.
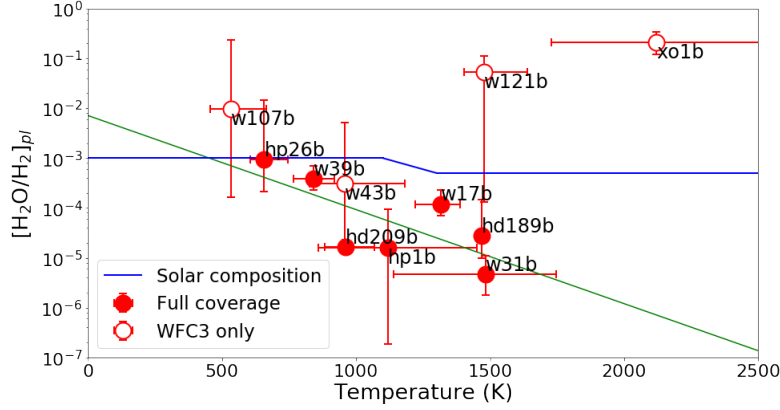
FIGURE 4.2: The retrieved planetary temperature versus the $[H_2O/H_2]$ ratios calculated from the retrievals. Open dots are planets with WFC3-only spectra, the filled dots also have coverage by STIS and Spitzer. The blue line indicates the expectations from equilibrium chemistry using a solar initial elemental composition (Madhusudhan, 2012; Woitke et al., 2018) and the green line shows the best fit to the filled dots.

From this Figure, it can be seen that HAT-P-26b and WASP-39b have a $[H_2O/H_2]$ abundance that is consistent with and slightly lower than the predictions from equilibrium chemistry. The planets with WFC3-only spectra are indicated by the open dots and although they generally seem to indicate an enhanced $[H_2O/H_2]$ abundance, most of them are consistent with any possible outcome. XO-1b is the exception here, but its extremely high water abundance is unlikely from a physical point of view and can be the result of retrieval using WFC3-only coverage (Heng et al., 2017). The rest of the filled dots (HD 209458b, HAT-P-1b, WASP-17b, HD 189733b and WASP-31b in order of increasing temperature) all lie significantly below the predicted values from equilibrium chemistry, which is an indication for the depletion of water in their atmospheres and might be a hint towards disequilibrium processes influencing the atmospheric compositions. Generally, there seems to be a trend of decreasing water abundance with increasing temperature for the filled dots, as indicated by the green line in Figure 4.2. Although this is thermochemically not expected, such a trend may be related to the incoming stellar radiation since this is a huge factor in the determination of the planetary temperature.

4.2.2 Photochemistry

Besides playing a key role in the determination of the temperature, stellar radiation may strongly influence a planet's atmospheric composition by photochemical processes and in this section we will try to quantify this influence, by looking at the irradiance from the host star that is received by the different planets. The derivation of this irradiance is described in Section 2.4.3. As a first step, we need to find a way to distinguish the existence of any possible trend from the fact that the planets may have formed in protoplanetary disks of varying elemental compositions. This can be done using the primary assumption that the protoplanetary disk had the same initial elemental composition as the host star (Madhusudhan, 2019), motivated by the fact that both the star and the disk are expected to be the result of the same collapsing protostellar cloud. Moreover, giant exoplanets are thought to have H_2 and He dominated primary atmospheres which are expected to be good tracers of the initial conditions. Therefore, the retrieved planetary $[H_2O/H_2]$ abundance can be normalized using the host star abundances as presented in Table 2.6. In case of an unknown stellar [O/H] ratio, the [Fe/H] ratio has been used instead. Conversion of the unit dex used for abundance ratios is done via:

$$[Z/H] = 10^{Z/H(dex)} \times [Z/H]_\odot \qquad (4.5)$$

The corresponding propagation of uncertainties in the stellar abundance ratios is calculated using:

$$\delta[Z/H] = 10^{Z/H(dex)} \times [Z/H]_\odot \times \log(10) \times \delta(Z/H(dex)) \tag{4.6}$$

Where $[Z/H]_\odot$ represents the abundance ratio using solar elemental abundances from Asplund et al. (2009), shown in Table 4.3.

Element	Abundance
$[Fe/H]$	3.16×10^{-5}
$[O/H]$	4.90×10^{-4}
$[Na/H]$	1.74×10^{-6}
$[K/H]$	1.07×10^{-7}
$[Al/H]$	2.82×10^{-6}
$[Cr/H]$	4.37×10^{-7}
$[Ti/H]$	8.91×10^{-8}
$[V/H]$	8.51×10^{-9}

TABLE 4.3: Solar abundances of various elements (Asplund et al., 2009).

The normalization of the planetary $[H_2O/H_2]$ allows us to make an approximate comparison between atmospheric abundances that resulted from presumably different formation conditions. To quantify the possible influence of photochemistry, Figure 4.3 shows the normalized $[H_2O/H_2]$ abundance as a function of the irradiance. It can be seen that HAT-P-26b and WASP-39b have a relatively high water abundance and are, at the same time, belonging to the least irradiated planets in our sample. The other planets with observations in both the optical and IR are found to have relatively low abundances. The WFC3-only planets again show the general behaviour of strongly enhanced abundances.
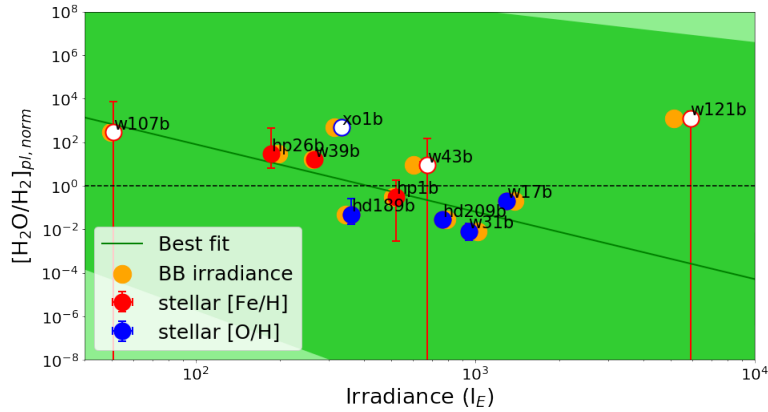

FIGURE 4.3: The irradiance received at the planet's location versus the normalized planetary $[H_2O/H_2]$ ratios from the retrievals. Where possible and indicated by the blue dots, stellar $[O/H]$ ratios have been used for the normalization. Where $[O/H]$ ratios are not available, $[Fe/H]$ has been used instead. Open dots are planets with WFC3-only spectra, the filled dots also have coverage by STIS and Spitzer. The orange points represent the irradiances calculated under the assumption of stellar blackbody radiation based on the effective temperature (see Section 2.4.3). A linear fit to the filled red and blue dots and its corresponding 1σ and 2σ is also shown.

Using both Figures 4.2 and 4.3, it can be seen that planets that are depleted in comparison to equilibrium chemistry expectations are also the planets receiving the highest irradiance. This might be an indication of photochemical processes causing disequilibrium chemistry and it has been attempted to quantify this trend by trying a linear fit on the normalized

[H_2O/H_2] abundance as a function of stellar irradiation. The enhanced but uncertain abundances of WFC3-only spectra make the open dots (especially WASP-121b and XO-1b) extreme outliers, greatly influencing the general behaviour seen in Figure 4.3. To prevent these physically unrealistic results from being the decisive factor in our analysis, it has been decided to exclude the results from WFC3 only spectra in the investigation of possible trends. By doing so, a negative trend can be identified in Figure 4.3, indicating that higher irradiation would lead to a lower [H_2O/H_2] abundance. The resulting best fit to the planets that have observations between 0.3 and 4.5μm is given by:

$$\log([H_2O/H_2]_{norm}) = (-3.09 \pm 1.63) \log(I/I_\oplus) + (8.09 \pm 4.38) \tag{4.7}$$

Despite the indicated negative slope, the linear fit can only provide a limited description of the data, having an R^2 of 0.55, and its 1σ and 2σ regions illustrate the large uncertainty. About half of the variance in the data is not accounted for by this fit and we do not observe a definite trend of the water abundance as a function of stellar irradiation.

Expanding the investigation of the possible photodissociation of water, it would be preferable to look at the planetary irradiance resulting from UV luminosity only: specifically in the FUV regime at 120 to 195nm (Heays et al., 2017). As described in Section 2.4.3, water might be dissociated by photons in this wavelength range via:

$$H_2O + h\nu \longrightarrow OH + H$$

UV measurements are hard to make and therefore also scarcely available for our stars. Therefore, the UV luminosities have been estimated using the stellar blackbody spectra, as shown by the pink contour in the lower wavelength regime of Figure 2.5. To justify this approximation to a certain extent, we can compare the blackbody luminosities with the actual luminosities by having a look at the orange dots in Figure 4.3. At least for the full spectral regime, the stellar output is well-approximated by the assumption of blackbody spectra, as is evident from how well the orange dots match the actual measured stellar outputs (blue and red dots). Figure 4.4 then shows the normalized [H_2O/H_2] abundance as a function of this FUV irradiance.

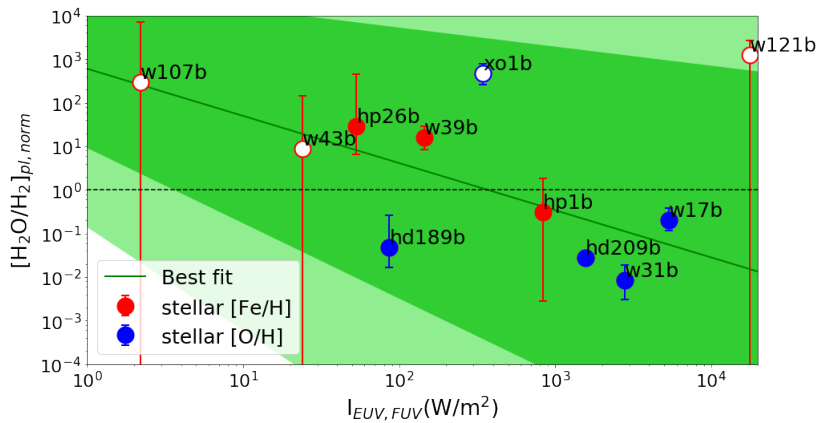FIGURE 4.4: Blackbody FUV irradiance received at the planet's location versus the normalized [H_2O/H_2] abundances from the retrievals. Where possible and indicated by the blue dots, stellar [O/H] ratios have been used for the normalization. Where [O/H] ratios are not available, [Fe/H] has been used instead. Open dots are planets with WFC3-only spectra, the filled dots also have coverage by STIS and Spitzer. A linear fit to the filled dots and its corresponding 1σ and 2σ is also shown.

Again excluding the WFC3-only sample and making the comparison with Figure 4.2, it can be noted that the planets with depleted [H_2O/H_2] abundances tend to receive more blackbody FUV radiation from their host star. HD 189733b is the notable exception here, having a highly substellar water abundance but receiving a relatively small amount of FUV

radiation under the assumption of a blackbody spectrum. A linear fit with the corresponding 1σ and 2σ uncertainty is shown by the green line and shaded regions respectively and results in the following relation:

$$\log([H_2O/H_2]_{norm}) = (-1.11 \pm 0.66)\log(I_{uv}) + (-3.01 \pm 1.95) \tag{4.8}$$

Although tighter constraints on the fit can be seen here, with an R^2 of 0.35 this linear fit is only a limited description of the data.

4.2.3   Mass-metallicity

Another possible trend can be explored using the assumption from equilibrium chemistry that for temperatures below ~ 1200K, the majority of O is found in H_2O and for temperatures above ~ 1200K, the O is more or less equally divided between H_2O and CO (Madhusudhan, 2012; Woitke et al., 2018). Following this, a planetary abundance ratio can be written as:

$$[O/H]_{pl} = \frac{[H_2O]}{[H_2O] + [H_2]} = \frac{[H_2O]}{[H_2O] + \frac{1-[H_2O]}{1.176}} \tag{4.9}$$

For planets hotter than 1200K, this ratio is then multiplied by two to compensate for the assumed abundance of O in CO. The uncertainty in the [O/H] ratio is calculated using the upper and lower bounds on the retrieved H_2O abundance. Using Equation 4.6, the planetary ratios can then be expressed in units of the stellar ratios via:

$$\frac{[Z/H]_{pl}}{[Z/H]_*} \tag{4.10}$$

With an associated uncertainty expressed as:

$$\frac{[Z/H]_{pl}}{[Z/H]_*}\sqrt{(\frac{\delta([Z/H]_{pl})}{[Z/H]_{pl}})^2 + (\frac{\delta([Z/H]_*)}{[Z/H]_*})^2} \tag{4.11}$$

This is equivalent to a normalization of the planetary abundance ratio or metallicity, again based on the primary assumption that the protoplanetary disk in which the planets formed had the same initial elemental composition as the host star (Madhusudhan, 2019). The resulting mass-metallicity relation is shown in Figure 4.5.
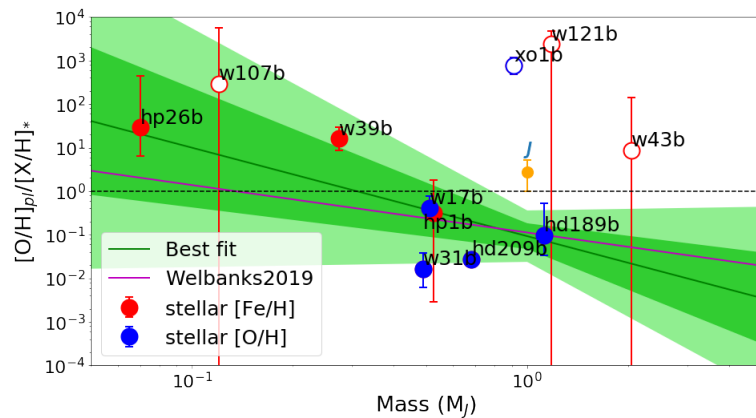

FIGURE 4.5: Mass-metallicity relation, with the planetary ratio in terms of the host star abundance ratio. The blue dots indicate normalization using stellar [O/H] ratios and red dots [Fe/H]. The green line and shaded regions show the linear fit and associated 1σ and 2σ uncertainty, excluding the planets with WFC3-only spectra. The purple line is the best fit found by Welbanks et al. (2019). The orange point represents the recent measured equatorial water abundance of Jupiter (Li et al., 2020).

The measured planetary abundance ratio also seems to decrease for increasing mass. The decreasing trend is seen from fitting the sample both with and without the WFC3-only planets. The green line is the linear fit excluding the WFC3-only planets and is given by:

$$\log([O/H]_{pl}/[O/H]_*) = (-2.03 \pm 1.07)\log(M/M_J) + (-1.03 \pm 0.30) \tag{4.12}$$

With an R^2 of 0.60, this relation appears to give a better description of the data but is still inconclusive. Notably, the retrieved abundances appear to be low compared to Jupiter's equatorial water abundance (Li et al., 2020). Welbanks et al. (2019) compare the relation to the solar mass-metallicity relation for inferences of giant planet [C/H] abundances and also report the exoplanetary trend to be subsolar.

4.2.4 Other species

A few of the planet-hosting stars out of our sample have more extended data on their abundance ratios, on top of the [Fe/H] and [O/H] ratios shown in Table 2.6. Using these stellar abundance ratios, we can make more estimates on enhancement or depletion of planetary abundances as compared to their host star.

Star	[O/H]	[Na/H]	[Ti/H]	[Cr/H]	Reference
HD 189733	0.070	0.040	0.050	0.050	Brewer et al. (2016)
HD 209458	0.090	-0.020	0.070	0.050	Brewer et al. (2016)
WASP-12	0.330	0.180	0.250	0.270	Brewer et al. (2016)
WASP-17	0.080	-0.210	0.010	-0.040	Brewer et al. (2016)
WASP-19	0.180	0.170	0.250	0.210	Brewer et al. (2016)
WASP-31	0.060	-0.170	0.010	-0.080	Brewer et al. (2016)
WASP-39	n/a	-0.04	-0.03	-0.07	Faedi et al. (2011)

TABLE 4.4: Abundance ratios for stars hosting some of the planets in our sample. The [O/H] ratio for WASP-39b was not available. All ratios are given in *dex* (see Equation 4.5).

With the abundance ratios as shown in Table 4.4, Equations 4.10 and 4.11 can be used to calculate the planetary abundance ratios in terms of those of the host star. Doing so, the simplified assumption was made that the species detected in our analysis contains the majority of the element in question. For example, since we only have knowledge of the abundance of CrH in WASP-31b, this is assumed to be the major Cr-bearing species. Equilibrium chemistry calculations predict important contributions from atomic Cr, CrO, CrS and, for high temperature, ionized Cr. For the [O/H] ratio a distinction has been made for temperatures below and above 1200K, as was also done in Section 4.2.3. Again, this allows to make a comparison to the abundance ratios of the host star and the result of this can be seen in Figure 4.6. This method generally seems to suggest the depletion of Oxygen in planets as compared to their host star, although WASP-17b and HD 189733b are more or less consistent with their host star. From the Na detection only, the Na abundance ratios are depleted for lower temperatures and consistent with those of the host stars for higher temperatures. Both chromium ($\sim$0.01 times stellar) and titanium ($\sim(1-6) \times 10^{-3}$ times stellar) seem to be depleted over a wider range of temperatures, according to detections of only CrH and TiO respectively.
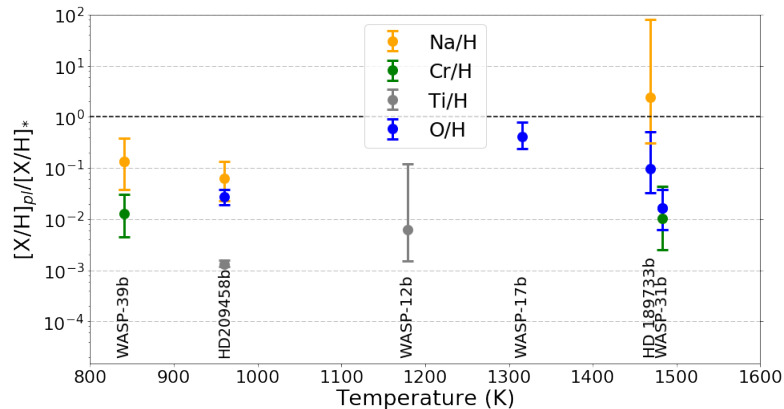
FIGURE 4.6: Planetary abundance ratios for 4 different elements, based on the relevant chemical species detected in this analysis. The ratios have been normalized by the stellar abundance ratios as given in Table 4.4 and the dashed horizontal line represents exact agreement between the ratios of planet and host star.

4.3   (Dis)equilibrium Chemistry

In Section 4.2.1, the retrieved water abundances are compared to the theoretically expected values at pressures of 1 bar, calculated assuming equilibrium chemistry of a gas consisting of Solar initial composition (Asplund et al., 2009). For such a composition and taking condensation into account, the gaseous species hosting a certain element and their expected abundances can be calculated by the minimization of the Gibbs free energy using, for example, the publicly available GGChem code (Woitke et al., 2018). The Gibbs free energy is a measure of the energy stored in a system that can be used to do work at constant temperature and pressure. The equilibrium composition of a system is reached when the free energy reaches a minimum value and there is no driving force behind a chemical reaction. An elaborate discussion of the Gibbs free energy can be found in Atkins et al. (2014). Abundances that deviate from the expectations from equilibrium chemistry indicate disequilibrium processes.

4.3.1   Water

The retrieved water abundances are $4-150$ times lower than the predicted values for the majority of the planets and seem to decrease with increasing temperature, as is seen by the best-fitting green line in Figure 4.2. This is not in agreement with the predictions from equilibrium chemistry, which approximately describes the behaviour as a step function with a transition region around 1200K. With an $R^2=0.52$ about half of the variance in the data is not accounted for by this fit and we do not observe a definite trend of the water abundance as a function of temperature. Nevertheless, the clear discrepancy between theory and observations needs to be explained. Possible causes of disequilibrium chemistry, which is an imbalance in chemical reactions between the forward and reverse direction, were introduced in Section 1.4.1 and may deliver (part of) this explanation (Moses, 2014).

Firstly, photochemical processes can alter the stratospheric composition of an atmosphere by absorption of shortwave radiation, as described in Section 2.4.3, and may be important for the composition at pressures <1 bar (Line et al., 2010), although other studies limit its influence to higher atmospheric layers (pressures <1mbar) (Moses et al., 2011). Since the transmission spectra probe an atmosphere between $\sim 1 - 10^{-3}$bar (see Figure 1.4), the influence of UV radiation on the retrieved chemical abundances may not be relevant. The photodissociation of water in Hot Jupiters has been studied before (e.g. Liang et al., 2003), motivated by the extreme UV fluxes expected to be received by Hot Jupiters. The results in Figure 4.4 do not show a definite trend between the water abundance and UV irradiation but the existence of a negative slope is suggestive for at least some influence. Such a negative

trend would be expected if the photodissociation of water is the main process controlling the water abundances. However, it should be noted that stellar UV outputs can be highly variable (e.g. Bourrier et al. (2020)) and our determination of FUV irradiance is a crude estimate, leaving the existence of this trend as inconclusive. The photolysis products in the form of OH also tend to quickly recycle back into H_2O in an H_2-dominated atmosphere (Moses, 2014), tempering expectations of observing water depletion with higher UV irradiances. Nevertheless, the reported detection of the spectral signatures of OH in WASP-19b, combined with the relatively high estimated EUV/FUV irradiance of $\sim 2500\,W/m^2$, might suggest that this recycling is not dominant here. This could be another interesting indication of water photodissociation in Hot-Jupiter atmospheres.

Another possible cause of disequilibrium abundances is transport-induced quenching. Since Hot Jupiters are expected to be tidally locked, large temperature differences between the day- and nightside can cause strong horizontal winds (Guillot et al., 1996). These winds can transport fluid parcels in chemical equilibrium from the dayside to the nightside, where they rapidly cool and reaction rates are too slow to equilibrate. Both horizontal and vertical transport may be important factors in relating photochemical influences to inferences from transmission spectra (e.g. Cooper et al. (2006), Steinrueck et al. (2019)). Since we do not retrieve any dynamical parameters, the importance of dynamics has not been investigated in this analysis.

As described in Section 2.2.4, the presence of clouds and/or hazes is also expected in Hot Jupiter atmospheres. A consequence of this presence is usually a flattening of spectral features since stellar photons are unable to penetrate below layers of clouds and hazes (e.g. Sing et al., 2013; Deming et al., 2013). This flattening of features may subsequently lead to lower chemical abundances resulting from our retrievals. In this regard, the observed decrease of H_2O abundance with increasing temperature in Figure 4.2 suggests that chances for the emergence of clouds and/or hazes increases with temperature. Looking at the thermochemical origin of clouds, condensation curves would imply this is counter-intuitive since species tend to condense out when temperatures decrease (Lodders, 2010). Alternatively, the presence of high-altitude hazes can explain both low abundances in general and abundances decreasing as a function of temperature since higher temperatures would imply higher (UV) irradiation. Kawashima et al. (2019) show that at least for planets of T<1000K, a higher UV irradiance might lead to enhanced photochemical production of hazes. Thus, the decreasing trend of water abundances with temperature in Figure 4.2 as well as UV irradiation in Figure 4.4 may be (partly) explained by increased production of hazes high up in the atmosphere, leading to an enhanced flattening of spectral features for more strongly irradiated (and thus hotter) planets. Although photochemical disequilibrium is less likely for higher temperatures, it may still be expected for planets of up to T=2000K (Moses, 2014; Moses et al., 2011). The hydrocarbons that might be haze precursors are expected to form from the photolysis of CH_4, which makes the production of hydrocarbons less likely at hotter exoplanets (Moses et al., 2011). Besides that, the strong optical slope that would be a consequence of scattering by haze particles is retrieved for only 3 planets, out of which only HD 189733b has a water detection. Therefore, assuming the parametrization for particle scattering in TauREx, no correlation is seen from the retrievals. Quantifying the possible relation between them would need more planets possessing both a significant water and haze detection.

4.3.2 Other species

The alkali metals found in our analysis seem to agree well with the expectations from equilibrium chemistry. For Na, the models of Woitke et al. (2018) predict most of Na in atomic form for a wide range of temperatures, at an abundance of around 10^{-6}. At temperatures lower than 750K, other Na-bearing species such as NaCl and NaOH become important and the expected abundance of atomic Na rapidly decreases. Most of our retrieved abundances are on the lower side of this prediction but still consistent with it, especially when taking uncertainties in the exact abundance as well as the retrieved temperature into account. HD 189733b stands out with a higher retrieved abundance but is also still consistent with the predictions. For K, similar behaviour is seen: an equilibrium abundance of around 10^{-7}

is expected with a rapid decrease below 750K due to KCl and KOH taking over. The retrieved abundances for HD 209458b and WASP-39b are on the low side but all planets are still consistent with equilibrium predictions.

As noted by Chubb et al. (2020c) for their detection of AlO in WASP-43b, aluminium is expected to be more abundant in a variety of molecules at the temperatures probed. For WASP-43b (957K) and WASP-101b (1141K), the most notable Al-bearing species would be atomic Al, AlOH, Al_2O, AlH, AlF and AlCl (Woitke et al., 2018). Regardless of temperature, the AlO abundance resulting from equilibrium chemistry never exceeds $log(AlO)=-8$, whereas the retrieved values are as high as -5.16 for WASP-43b and -6.23 for WASP-101b. Sources of this high AlO abundance may be the deeper layers of the atmosphere via vertical mixing and/or the evaporation of clouds consisting of Al-bearing species such as Al_2O_3 (Chubb et al., 2020c).

For TiO and VO, Woitke et al. (2018) predict abundances of up to 10^{-7} and 10^{-8} respectively at 1500K, with decreasing abundances for lower and higher temperatures. Both molecules belong to the major element-bearing species at the temperature ranges of Hot Jupiters and the results for HD 209458b, WASP-12b and WASP-52b are on the lower end as compared to the predictions, especially for HD 209458b. This result was found before and explained by the strong day-night temperature gradient causing strong horizontal winds (Parmentier et al., 2013). On the dayside, TiO may be in gaseous phase whereas it might quickly condense out on the nightside due to the lower temperatures. This process can form a cloud base and lead to depletion under the influence of gravitational settling. Parmentier et al. (2013) show that this can lead to a cold trap on the nightside of HD 209458 b, depleting TiO from the atmosphere. Under the influence of these processes, differences between the evening and morning terminator regions can also be expected. The VO-abundance of WASP-121b seems unreasonably high but this might also be related to constraining the VO abundance using a WFC3-only spectrum.

The retrieved abundance of OH in the atmosphere of WASP-19b is also high compared to equilibrium expectations: at WASP-19b's temperature of $\sim$ 1500K, an abundance of up to 10^{-9} is expected. For higher temperatures, this could increase towards 10^{-4}. An extreme combination of vertical mixing and photochemical dissociation of water perhaps results in abundances as high as $10^{-2.37}$. However, the limited spectral coverage of WASP-19b and the resulting similarity between H_2O and OH signatures leave this result as inconclusive but intriguing for follow-up with JWST (see Section 4.6).

Lastly, there is the detection of CrH in the atmospheres of WASP-31b and WASP-39b. Not CrH but atomic chromium is the main Cr-bearing species for the temperatures of these planets, whereas significant fractions are also expected to be in CrO or CrS. Nevertheless, at these temperatures, CrH is expected from equilibrium chemistry at abundances between 10^{-10} and 10^{-9}. The retrieved abundances are relatively high, indicating that processes such as vertical mixing or a source of atomic Hydrogen reacting with atomic chromium may be needed to explain the observed CrH. Since atomic Hydrogen is a product of the photodissociation of water (see Section 4.2.2), this process may contribute to the production of CrH.

4.4 Planet Formation

The stellar ages in Table 2.6 range from 1Gyr to 11Gyr and tell us that the planets in our sample may range from young to ancient exoplanets. This variety in ages may have implications for mass-loss through atmospheric escape (Owen, 2019), whereas atmospheric abundances may also be related to the conditions during the formation of the planets (Öberg et al., 2011). Low H_2O abundances are possible in two ways, relating to these conditions (Madhusudhan et al., 2014). Firstly, the overall planetary abundances may be low, implying that element abundances such as [O/H] are low while ratios between elements are solar (e.g. C/O$\sim$0.5). Alternatively, the overall abundances may be consistent with or superstellar but the C/O ratio is high (Madhusudhan, 2012). As can be seen from Table 2.6, the majority of planet-hosting stars in our sample have supersolar abundances. Following the core accretion scenario for forming giant planets (Pollack et al., 1996), the Hot Jupiters around these stars can also be expected to have high oxygen content and, consequently, high H_2O abundances.

The generally substellar [O/H] ratios seen in Figure 4.5 might then also have some important implications for the formation scenarios of these planets. The main factors determining the atmospheric composition of a Hot Jupiter are the location where it forms in the disk and the relative amounts of gas and solids that are accreted (Brewer et al., 2017). This same study finds evidence for a general trend of high C/O ratios in Hot Jupiters and most prominently HD 209458b. Combined with a substellar [O/H] this suggests the formation of this planet beyond the water snow line from where it subsequently migrated inwards, after the gas in the disk had dissipated and without significant solid accretion.

Figure 4.6 gives an ensemble of retrieved abundance ratios of the planets in terms of that of their host stars, assuming the detected species contains all of the particular element. For HD 209458b, this indicates substellar ratios for [O/H] at 3%, [Na/H] at 6% and [Ti/H] at 0.1%. As described above, the low [Ti/H] might be explained by the presence of Ti in other Ti-bearing species or due to the existence of a cold trap (Parmentier et al., 2013). Correcting for this would probably still result in substellar values and our analysis thus also suggests overall substellar abundances for HD 209458b. Although an estimate of the C/O ratio is not included in our analysis, the substellar abundances, combined with the superstellar C/O ratio of Brewer et al. (2017), is an indication that HD 209458b formed beyond the water snowline and, after the dissipation of the disk, subsequently migrated inwards without accreting a significant amount of solids.

The abundance ratios of WASP-31b and WASP-39b are about 0.1% of the stellar ratios and also hint toward overall low abundances, possibly related to a similar scenario. However, the presence of Cr in other Cr-bearing species might significantly increase the [Cr/H] ratio. Besides that, no evidence for high C/O ratios currently exists: for WASP-39b there is evidence of a low C/O ratio instead (Wakeford et al., 2017b).

HD 189733b seems to have [O/H] and [Na/H] more or less consistent with its stellar values. Combined with the stellar C/O ratio (Brewer et al., 2017), this could be an indication for the formation of this planet close to its host star according to the core accretion scenario. The retrieved presence of Mie scattering due to clouds/hazes, which could cause some obscuration, may explain the [O/H] ratio (and H_2O abundance) being on the low side.

For WASP-12b we report a large substellar [Ti/H] ratio, but this might again be (partially) caused by a cold trap (Parmentier et al., 2013) or the presence of other Ti-bearing species. The lack of other abundance ratios leaves this result as inconclusive.

WASP-17b seems to be in good agreement with the predictions from equilibrium chemistry as well as the host star abundance ratios. This might indicate formation close to its host star (depending on the C/O ratio) as well as clear skies on the planet, as was also reported by Sedaghati et al. (2016). This agreement and the fact that such a clear water signature is seen in its spectrum make WASP-17b an interesting target for further characterisation with the upcoming facilities that will be discussed in Section 4.6.

4.5 Systematic Uncertainties

There are a number of systematic uncertainties influencing the results as presented in this thesis. As a first deficiency, the analysis that is presented in Chapter 3 does not take the bandwidths associated with the spectroscopic observations into account. Especially considering the broadband photometric observations made by Spitzer, these bandwidths are significant and their omission influences the retrieved values for the evidence and the atmospheric parameters. Table 4.5 compares the retrievals with and without bandwidths for WASP-31b (many measurements in the spectral regime) and WASP-19b (sparse coverage). Although small, it can be seen that systematic errors are introduced by this deficiency: the atmospheric signatures show similar behaviour and retrieved abundances show modest variations. The values with and without bandwidths are still consistent with each other in the retrieved uncertainties. Furthermore, taking the bandwidths of observations into account leads to slight decreases in the Bayesian evidence associated with the models. This decrease is not surprising since the inclusion of bandwidths leads to an additional factor of uncertainty for an atmospheric model. The Detection Significance, quantifying the preference of the more complex over the flat model, can also be compared and does not change significantly with the inclusion of the bandwidths. Therefore, our resulting atmospheric detections can still be

seen as valid. Nevertheless, the first improvement in this analysis will be to eliminate this systematic uncertainty. Another consequence of this deficiency is the offsets that are seen for the diamonds in the spectra in Figure 3.4. These diamonds should be located on the model fit at the location of each of the measurements. Not considering the bandwidths leads to offsets for some of these diamonds, as clearly seen for the 3.5μm point of, for example, WASP-31b. This effect is purely visual and is solved by including the bandwidths in our analysis, as shown for WASP-31b in Figure 4.7.

TABLE 4.5: Comparison between results from retrieval with and without bandwidths, considering the highest evidence model from our analysis in Chapter 3.

WASP-19b	log(OH)	T(K)	R_p	P_{cl}	log(E)	DS		
without band widths	$-2.37^{+0.75}_{-0.79}$	1534.07^{+380}_{-253}	$1.38^{+0.00}_{-0.01}$	$4.97^{+0.68}_{-0.57}$	96.51	5.77		
with band widths	$-2.41^{+0.80}_{-0.78}$	1536.17^{+375}_{-261}	$1.38^{+0.00}_{-0.01}$	$4.98^{+0.70}_{-0.57}$	96.43	5.63		
WASP-31b	log(H_2O)	log(CrH)	log(K)	T(K)	R_p	P_{cl}	log(E)	DS
without band widths	$-5.40^{+0.37}_{-0.42}$	$-8.49^{+0.62}_{-0.61}$	$-7.63^{+0.75}_{-0.87}$	1483.08^{+264}_{-344}	$1.48^{+0.02}_{-0.01}$	$3.88^{+0.21}_{-0.21}$	409.50	9.72
with band widths	$-5.41^{+0.38}_{-0.40}$	$-8.49^{+0.62}_{-0.62}$	$-7.60^{+0.68}_{-0.90}$	1489.45^{+256}_{-356}	$1.48^{+0.02}_{-0.01}$	$3.88^{+0.20}_{-0.20}$	409.47	9.81
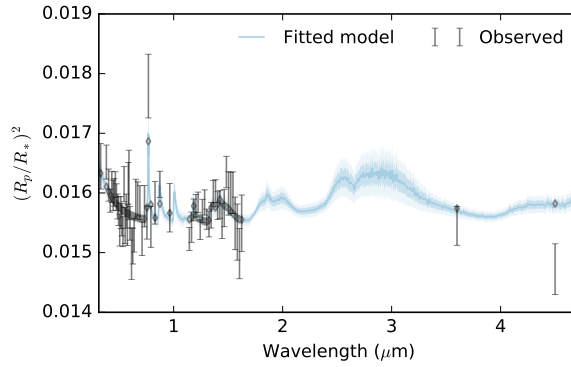
FIGURE 4.7: The transmission spectrum and model fit for WASP-31b, taking into account the bandwidths of the measurements.

The bottom-up approach followed here is valuable in inferring the presence of chemical species in an exoplanet atmosphere. However, this approach may introduce biases in the constraints on retrieved parameters. A non-detection of a particular species on the basis of this purely statistical approach does not necessarily imply the complete absence of this species in an atmosphere. Instead, its non-detection can be caused by an abundance that is too low to be statistically significant, the obscuration of signatures by the presence of clouds/hazes or the overlap with other spectral signatures. The omission of a particular species can then influence the retrieval outcomes since its signatures (even if they are statistically insignificant) have to be explained by the absorption of other species. This may result in unreasonably tight constraints as well as unrealistic values for retrieved abundances. In this way, the retrievals may introduce biases in, for example, the abundances of species that are included in the model.

Thirdly, the normalisation in Section 4.2.2 was done with the purpose of removing the possible dependence of atmospheric abundances on initial conditions in the specific planetary system. Stellar [O/H] ratios were not available for a number of host stars and, therefore, their [Fe/H] ratios were used. As can be seen from Table 4.3, the Sun has an [Fe/O] ratio of 0.05 and for the other stars in our sample a similar [Fe/O] ratio is found (0.05−0.065). Therefore, the normalization of planetary ratios by a combination of stellar [Fe/H] and [O/H] ratios can be expected to lead to another systematic uncertainty. Figure 4.8 shows the resulting mass-metallicity trend by using only [Fe/H] ratios to normalized the retrieved abundances

and it can be seen that with a slope in log-space of -0.49 ± 1.36 the trend is less strong. This illustrates the biases that result from using different abundance ratios for normalization and will also decrease the strength of the trends in Figures 4.3 and 4.4.
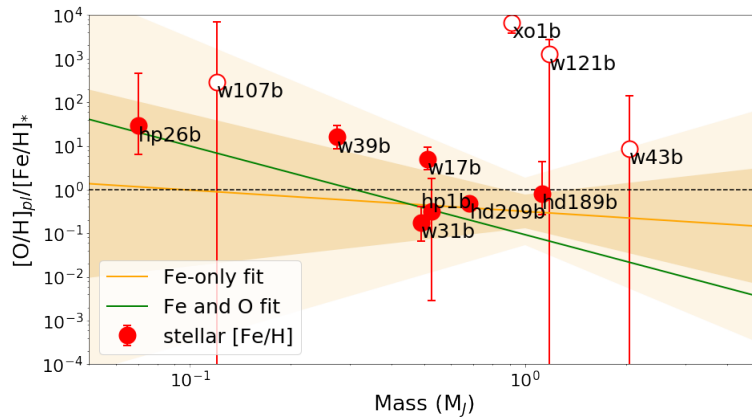

FIGURE 4.8: Same as Figure 4.5: mass-metallicity relation, but now with planetary ratios in terms of the host star [Fe/H] ratio only. The orange line and shaded regions show the linear fit and associated 1σ and 2σ uncertainty, excluding the planets with WFC3-only spectra. The green line is the best fit found by using both [Fe/H] and [O/H] ratios for normalization.

Finally, the 1D retrieval performed here assumes that the averaged terminator properties are representative for the complete atmosphere. In view of the limited data and the computational expenses, 1D retrieval is a reasonable starting point. However, thermal and compositional gradients between the day- and nightside of a planet can significantly influence transmission spectra (Caldas et al., 2019; Pluriel et al., 2020). Hence, analysing the inherently 3D atmospheric structure with 1D retrievals can lead to systematic uncertainties in temperatures and abundances and future work should be aimed at understanding these biases and/or incorporating higher dimensional atmospheric models in the retrieval process.

4.6 Prospects for JWST

The prospects for already near-future space-based exoplanet characterisation are exciting with the planned launch of the James Webb Space Telescope (JWST) in 2021 and ARIEL in 2028 (Tinetti et al., 2018). JWST will offer a wide spectral range from 0.6 to $28\mu m$ (Beichman et al., 2014). The spectral resolution of JWST for the observations of exoplanet atmospheres varies greatly over its four instruments. NIRISS can provide simultaneous wavelength coverage from $1-2.5\mu m$ at R$\sim$700 and NIRCam offers 2 modes at R$\sim$700 for $2.5-3.9\mu m$ and $3.9-5.0\mu m$. Besides that, NIRSpec has medium (R$\sim$1000) and high resolution (R$\sim$2700) spectroscopic modes for 4 separate wavelength regimes in the range $0.7-5.2\mu m$ and a low resolution (R$\sim$100) mode for simultaneously obtaining data in the $0.7-5.2\mu m$ range. MIRI covers the range from $5-12\mu m$ with a low resolution mode (R$\sim$100). Lastly, the medium resolution mode (R$\sim$1550 $-$ 3250) of MIRI can span the full range from $5-28\mu m$ but would need three different visits to the same object. A comprehensive review of the expected outcomes from transits observed by JWST (transmission as well as emission spectra) is provided by Greene et al. (2016). High-quality spectra between 1 to $11\mu m$ will likely be obtained for a variety of exoplanets and for many cases (especially planets with clear skies) already the range of $1-2.5\mu m$ will suffice to constrain the major chemical constituents in an exoplanetary atmosphere (Greene et al., 2016). Nevertheless, measurements of up to four instruments may have to be combined and in doing so, we need to take systematic errors as well as stellar variability into account (Barstow et al., 2015). To complement the analysis done here, the transmission spectra of a selection of our sample can be simulated for the wider JWST range.

As a first example, the results from the highest evidence retrieval model of WASP-39b can be used. Comparing the different atmospheric models in Figure 4.9, it can be seen that CrH only influences the spectrum around $\sim 1\mu$m, which is relatively well-covered already with current instruments. NH$_3$ is a particularly active absorber at longer wavelengths and coverage between 1 and 2.5μm will greatly increase the estimate on its presence. Therefore, JWST will likely provide us with key information to either confirm or rule out the presence of NH$_3$ and/or CrH.
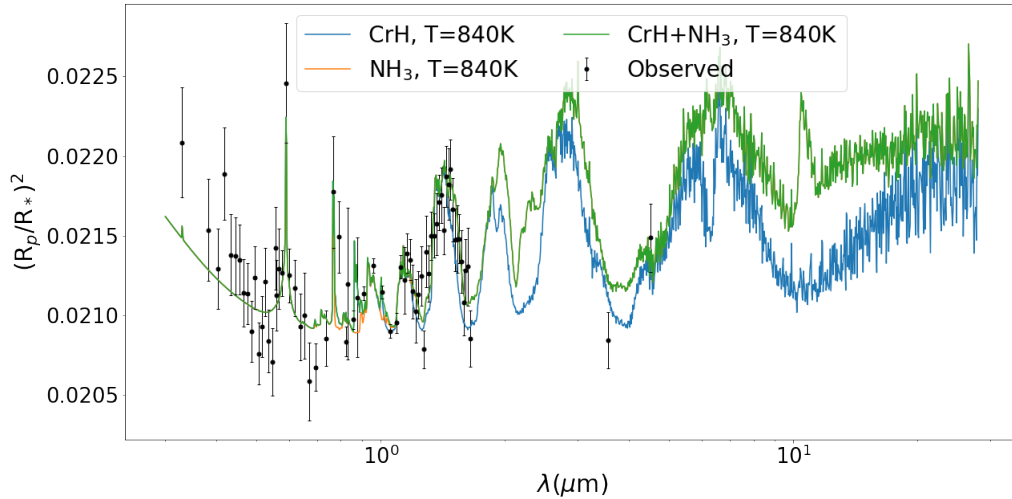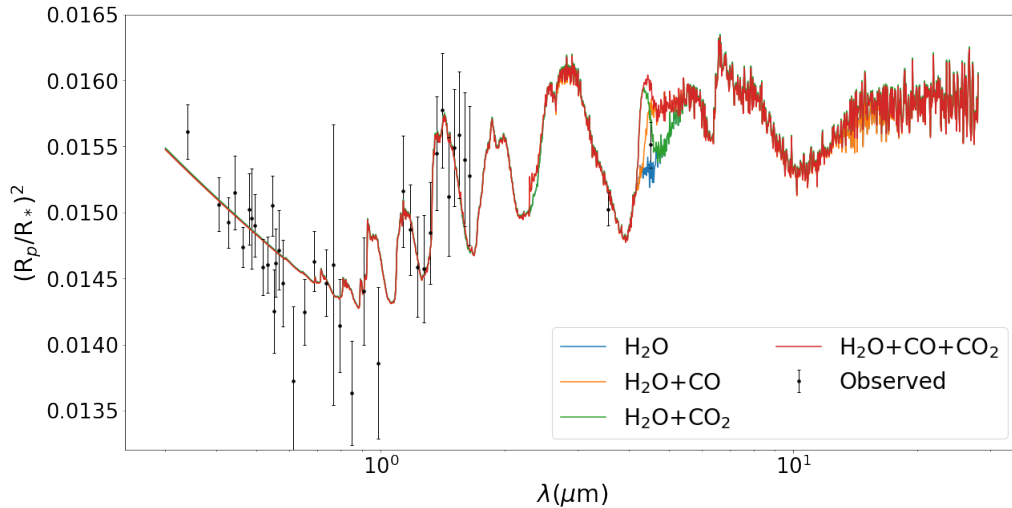

FIGURE 4.9: The expected appearance of the spectrum of WASP-39b in the JWST range, based on the parameters resulting from the highest evidence retrieval model. On top of the presence of H$_2$O, Na and K, the different lines correspond to the inclusion of CrH, NH$_3$ and CrH+NH$_3$, with log(CrH)$=-8.4$ and log(NH$_3$)$=-5$. The current observations are indicated by the black dots and corresponding error bars.

As described in Section 3.2.1, for WASP-19b there are uncertainties in distinguishing between the inclusion of OH and/or H$_2$O to explain its spectrum. For this planet, either the presence of OH at a temperature of 1534K or the presence of H$_2$O at a temperature of 1805K can explain the observed spectrum. Figure 4.10 shows the expected appearance for JWST of different models based on the retrievals of WASP-19b. It can be seen that the different appearances around $\sim$1 and $\sim$2μm only can already provide evidence to confirm or deny the presence of H$_2$O and/or OH to explain the spectrum. This might provide important evidence for possible photochemical processes in Hot Jupiter atmospheres, as described in Section 4.3.
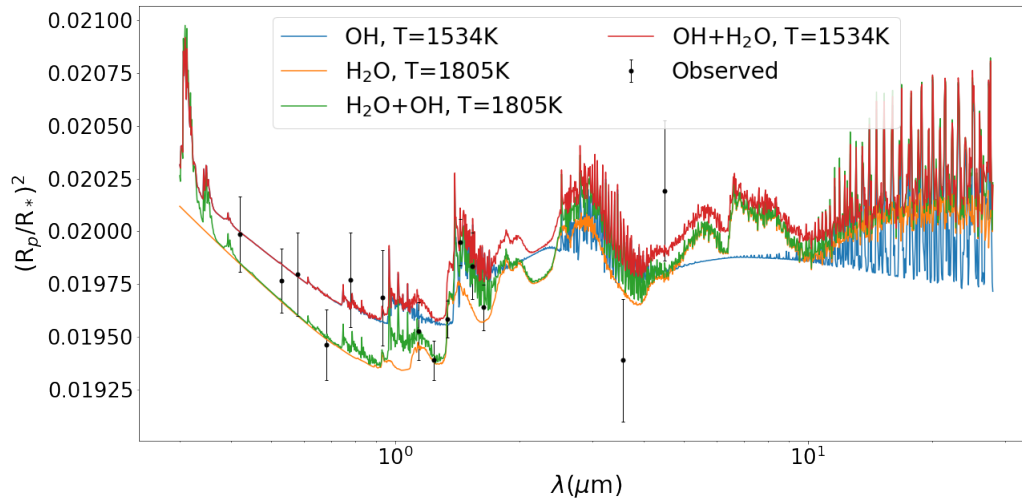
FIGURE 4.10: The expected appearance of the spectrum of WASP-19b in the JWST range, based on the parameters resulting from the highest evidence retrieval models. The blue and orange spectra are based on two models found to have a high evidence by the retrieval, with $\log(H_2O)=-5.6$ and $\log(OH)=-2.4$. The other lines combine these results for the different retrieved temperatures. The observations are indicated by the black dots and corresponding error bars.

Thirdly, the spectrum of WASP-17b[1] can be used to illustrate JWST's capacity to constrain the C/O ratio at high temperatures (Greene et al., 2016) by constraining the molecular abundances of CO and CO_2. Section 4.4 describes the importance of the C/O ratio in determining the planetary formation history, while CO and CO_2 are expected to be the main C-bearing species at high temperatures (Woitke et al., 2018). Figure 4.11 shows that while the spectral appearance of the different models is hardly distinguishable for a wide wavelength range, the absorption signatures seen around 4.5μm should be significant to provide constraints on the presence of CO and/or CO_2.

---

[1]In Guaranteed Time Observation program of JWST: GTO 1353 (https://www.stsci.edu/jwst/observing-programs/approved-gto-programs)

FIGURE 4.11: The expected appearance of the spectrum of WASP-17b in the JWST range, based on the parameters resulting from the highest evidence retrieval model ($\log(H_2O)=-4$) and the inclusion of CO and/or CO_2. The Na absorption peak around 0.6μm is excluded from the models because it does not provide an adequate fit to the data around it (see Section 4.1.2). The current observations are indicated by the black dots and corresponding error bars.

HAT-P-26b[2] is both the smallest and the coldest planet in our sample. At its temperatures, CH_4 is expected to be the main C-bearing species (Woitke et al., 2018). To illustrate the detectability of CH_4, Figure 4.12 shows the spectrum assuming an atmospheric model with (orange) and without (blue) its presence. It can again be seen that the two spectra are clearly distinguishable between 1 and 2.5μm already. In this case, the C/O ratio may be derived based on the constraints on the CH_4 abundance and this might again provide insights into the planet formation history.
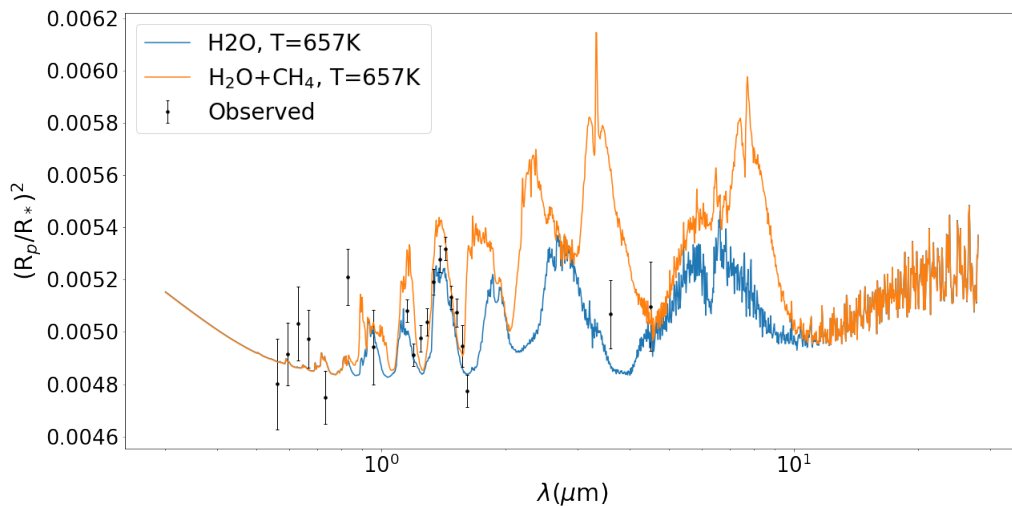
FIGURE 4.12: The expected appearance of the spectrum of HAT-P-26b, based on the parameters resulting from the highest evidence retrieval model ($\log(H_2O)=-3.1$) and the inclusion of CH_4. The observations are indicated by the black dots and corresponding error bars.

Regarding the prospects for the other planets in our sample, it is worth mentioning that WASP-43b, WASP-101b and XO-1b are part of the Early Release Science Program (Bean et al., 2018; Stevenson et al., 2016). Furthermore, the GTO includes transmission spectra of HAT-P-12b (1281), WASP-52b (1201) and WASP-107b (1201, 1224, 1280). The lack of NIR data and the huge difference in optical and Spitzer transit depth make WASP-6b (for the spectrum, see Figure 3.4) another interesting target for further characterisation. The spectra that have been simulated for the JWST range are highly simplified by only including the species that were retrieved and those with implications for the C/O ratio. Actual JWST spectra can be expected to contain many more absorption signatures due to the presence of a wide variety of chemical species and also have the potential to further enhance our knowledge of clouds and/or hazes (e.g. Kempton et al. (2017)). Without a doubt, observing the spectrum of any of the planets with JWST will lead to surprising and insightful results and this makes any planet in our sample an intriguing candidate for further characterisation.

Chapter 5

Conclusions

With the goal of investigating the possible existence of chemical trends, the transmission spectra of 17 exoplanets have been comparatively analysed using the TauREx II retrieval framework. The planets can be classified as Hot Jupiters and 12 of them offer coverage from 0.3 to 4.5μm, whereas the others only have observations available in the NIR (1.1 to 1.7μm).

Under the assumption of the simplified atmospheric model in TauREx and out of the trials that were part of this analysis, the retrievals mainly resulted in the detection of the characteristic absorption signature of water, of which 11 detections were made. Following Jeffreys' scale, the detection significances vary from $\sim$2.3σ for HAT-P-1b to far greater than 5σ for other planets, as compared to a flat model containing no spectral signatures. Furthermore, we confirm the detections of TiO in HD 209458b and WASP-12b, VO in WASP-52b and WASP-121b and AlO in WASP-43b. The presence of signatures of OH in WASP-19b and AlO in WASP-101b are indicated with a significance of $\sim$2.1σ, although it should be noted that alternatively explaining the spectrum of WASP-19b by the presence of water can not be ruled out statistically. The characteristic absorption peaks of the alkali metals Na and K were each detected for 5 of the planets with optical coverage, whereas particle scattering following Mie theory was needed to explain the absorption slopes at UV and optical wavelengths in the spectra of HAT-P-12b, HD 189733b and WASP-52b.

The first indications for the presence of CrH in Hot Jupiter atmospheres have also been found. For WASP-39b, the CrH signature is currently hard to distinguish statistically from a model including NH_3 instead. Nevertheless, the addition of CrH to a model containing only H_2O is preferred at $\sim$3.5σ significance. It has been shown that future observations with JWST may help to solidify the confidence in detecting the signatures of any of these species. For WASP-31b, the preference for the inclusion of CrH is already evident from the current observations. The inclusion of CrH has a significance of $\sim$3.8σ over the flat model, while the additional inclusion of H_2O is prefered with $\sim$2.6σ over the CrH-only model.

The most reliable abundance constraints were retrieved for spectra with coverage by STIS, WFC3 and Spitzer, while abundances that were retrieved using WFC3-only spectra suffer from degeneracies between abundances on the one hand and planet radii or clouds/hazes on the other. With this in mind, only the planets with coverage by the three instruments were used to explore the possible dependence of retrieved abundances on planetary parameters. The retrieved water abundance generally is lower than predictions from equilibrium chemistry, most notably for the planets of higher temperature, and an attempt was made to relate this to disequilibrium processes. Since the temperature of a planet is strongly related to the amount of radiation it receives, the dependence of the water abundances on the estimated FUV irradiation was investigated. While the intuitively correct observation was made that more strongly irradiated planets have lower water abundances, possibly indicating the photodissociation of water, a fit to this trend was not found to be statistically significant. On top of that, it is unsure whether photodissociation is relevant for transmission spectra at all. Instead of photodissociating water, UV irradiation might lead to lower abundances due to the production of photochemical hazes. To further explore the influence of photochemistry, actual measurements of the stellar UV output would be a noteworthy improvement over the blackbody estimation that was made here. It was also shown that the spectral range of JWST may lead to more improved constraints on the signatures and thus abundances of H_2O and its photolysis product OH, possibly providing further insight in exoplanetary photochemistry.

The mass-metallicity relation for O/H abundance ratios resulting from the retrievals agrees within 1σ with earlier findings but suffers from biases due to the normalization by stellar [Fe/H] as well as [O/H] ratios. Further planetary abundance ratios were inferred under the assumption that a particular element is exclusively found in the chemical species that was detected as part of our retrievals. The exception here was oxygen, which is assumed to be equally divided between H_2O and CO for T>1200K. Where stellar data was available, the resulting abundance ratios (Cr/H, Na/H, O/H and Ti/H) were compared to the stellar ratios. Both stellar and substellar (6×10^{-3} to 10^{-1}) abundance ratios are seen. Combined with planetary C/O ratios, if available, this provides a hint towards formation pathways. Substellar ratios and high C/O ratios may be expected when a planet forms outside of the water snowline and subsequently migrates inwards at a low solid accretion rate. In contrast, stellar ratios may be expected for a planet forming close to its host star. For now, a wide variety of formation histories seem plausible based on the abundance ratios.

5.1 Future work

The analysis presented in this thesis can be further improved in its homogeneity by conducting a retrieval on every transmission spectrum including the full set of molecules for which a significant detection was found. Thus, retrieve every planet using a model including AlO, CrH, H_2O, Na, K, OH, TiO and VO plus some of the molecules predicted to be present by equilibrium chemistry, such as CH_4, CO, CO_2 and NH_3. Detections would still only be reported in the case of a sufficient detection significance (DS). As said in Section 4.5, a non-detection does not necessarily imply the absence of a particular species and, therefore, subjecting every planet to the same model complexity can lead to better and more homogeneous estimates on the abundances of species that have a significant detection. The recent upgrade to TauREx III (Al-Refaie et al., 2019) offers support for the high amount of free parameters since it has reduced the time to perform retrieval by a factor of 6.

As another recommendation for this analysis, the sample size can be increased and the wavelength coverage can be improved and extended. For example, the WFC3 observations for WASP-12b used here are of limited quality and an improved observation was made by Kreidberg et al. (2015), clearly indicating the presence of water. Furthermore, recent observations of WASP-52b (Bruno et al., 2018) and WASP-6b (Carter et al., 2020) extend the coverage for those planets into the WFC3 regime as well.

A definite disentanglement of the different processes influencing the atmospheric composition (also including transport-induced quenching) would need indisputable trends. This challenging endeavour will need improvements on many sides: increased homogeneity by a retrieval including all relevant molecules, better understanding of clouds/hazes, better estimates of C-bearing species for C/O ratios, improved stellar UV measurements and more knowledge on the biases induced by conducting 1D retrievals to describe the 3D structure of an atmosphere. The potential of JWST in elucidating ambiguous results and accurately quantifying C/O ratios was illustrated, while JWST might also be a step forward in interpreting clouds/hazes. In the longer term, ARIEL (2028) will lead to a wealth of planetary spectra that can be used for comparative studies and SPICA (2032) will provide high-resolution spectra of transiting exoplanets as well as MIR direct images of far-out exoplanets (Goicoechea et al., 2008). Other proposed missions such as LUVOIR[1] and HabEx[2] aim to take the next leap towards the characterisation of potentially habitable exoplanets (Snellen et al., 2019).

All in all, uncovering the myriad of processes influencing the atmospheric state of an exoplanet may seem to be an intimidating endeavour. Nevertheless, the wealth of knowledge that has already been acquired using instruments that were not necessarily designed to do so, can only leave us fascinated for the potential outcomes of improved and more dedicated facilities.

---

[1] https://asd.gsfc.nasa.gov/luvoir/
[2] https://www.jpl.nasa.gov/habex/

Appendix A

Additional Retrieval Plots

In Chapter 3, the procedure of retrieval and model selection is described in detail for WASP-39b. To support the interpretation of retrieval outcomes, the results for several other planets were also shortly described. Every planet has three plots resulting from the retrieval procedure (spectrum, posterior distributions and individual opacity contributions) and a plot with the model comparison. To preserve readability, many of these plots have not been included in Chapter 3. In what follows, the plots that were not included in the main body of this Thesis are provided per planet.

A.1 HAT-P-1b
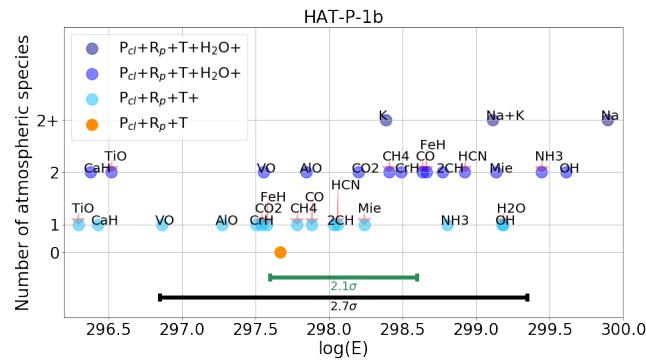
FIGURE A.1: Model comparison for HAT-P-1b using the Bayesian evidence for different atmospheric models. The flat model is shown as the orange dot, while cyan dots indicate more complexity in the form of a chemical species or Mie scattering specifically indicated by the label accompanying each dot. One level higher, blue dots represent H_2O and an additional parameter, again specified by the label accompanying the dot. For the third level the highest evidence model from lower complexities is complemented by Na and/or K. The scale bars indicate the statistical preference for a more complex model over a simpler one and are based on the difference in Bayesian Evidence between models (see Table 2.3).
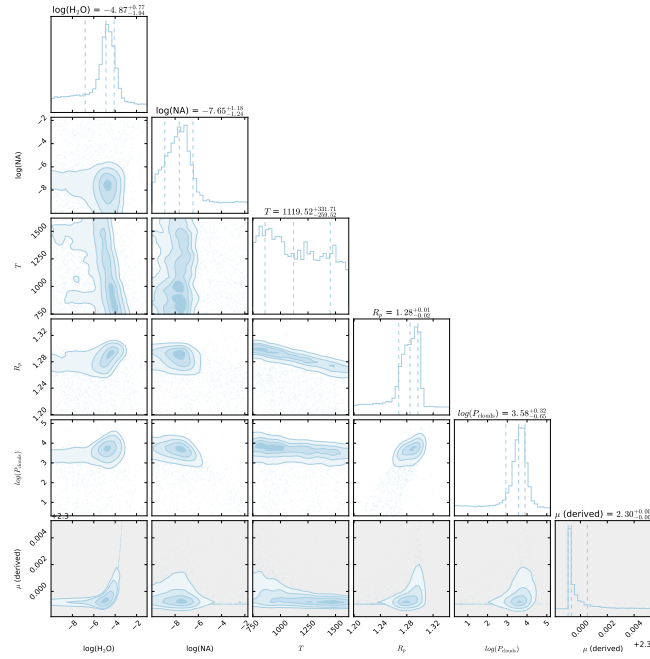
FIGURE A.2: Posterior of the retrieval for HAT-P-1b.
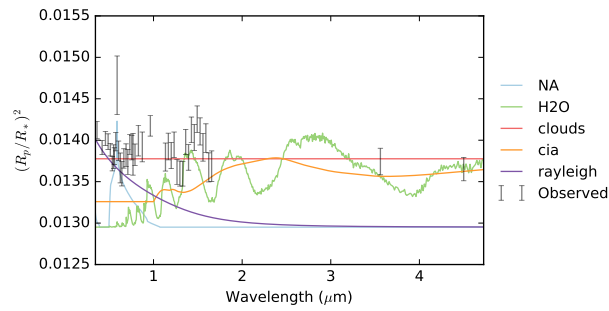
FIGURE A.3: The opacity contributions for each of the parameters in the highest evidence model for HAT-P-1b.
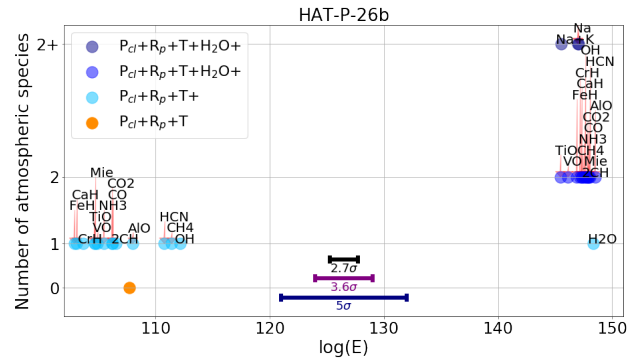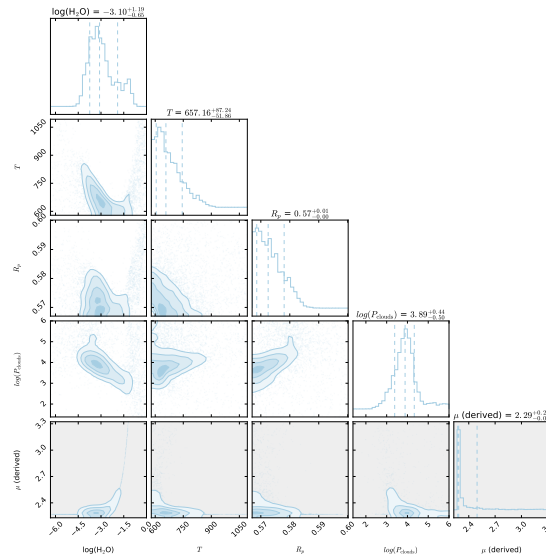
A.2 HAT-P-12b
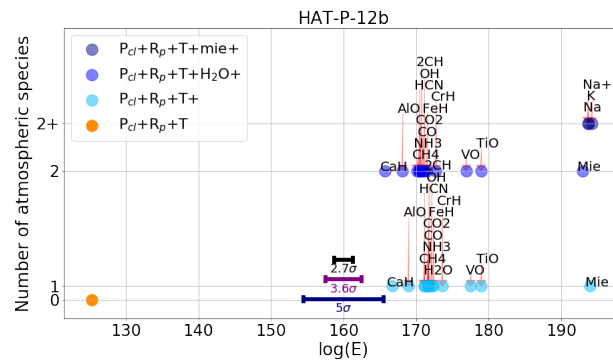
FIGURE A.4: Model comparison HAT-P-12b, see caption of Figure A.1.
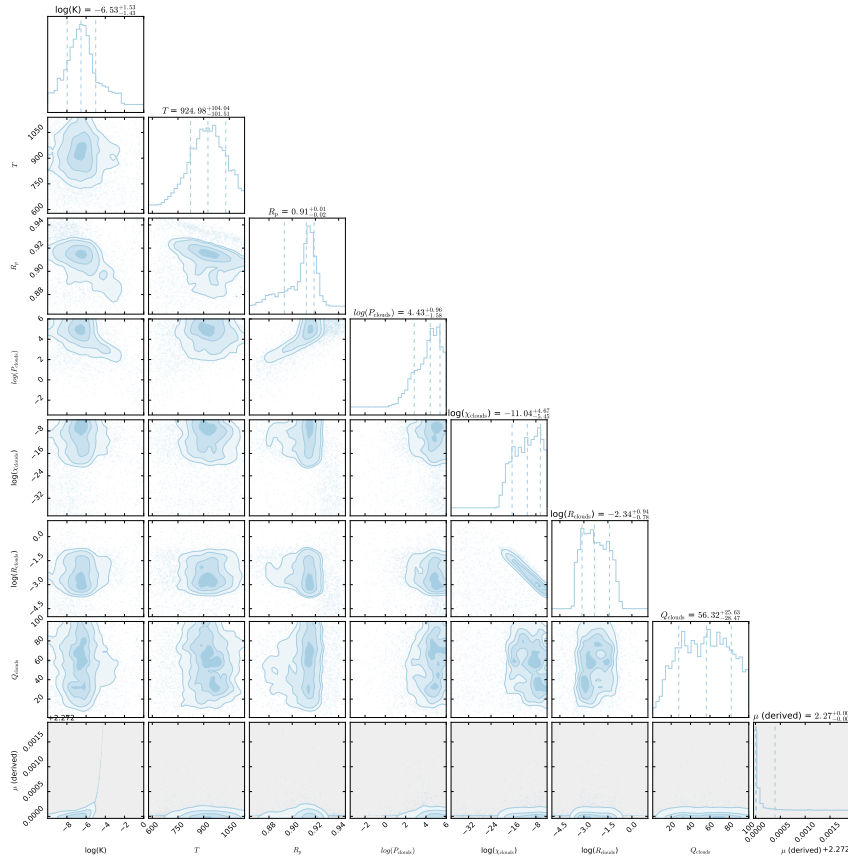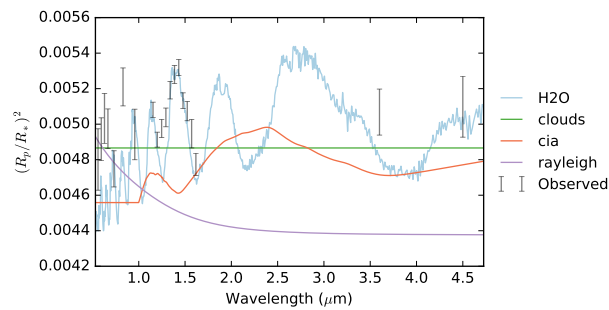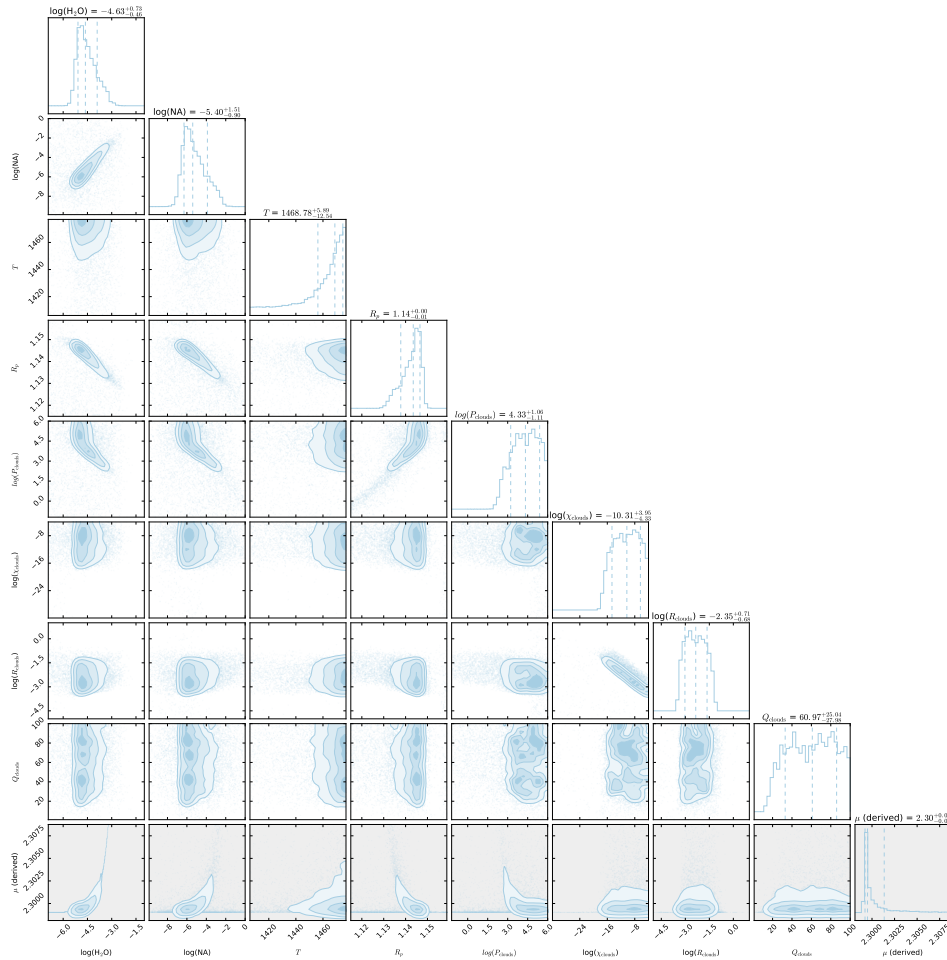
FIGURE A.5: Posterior of the retrieval for HAT-P-12b.
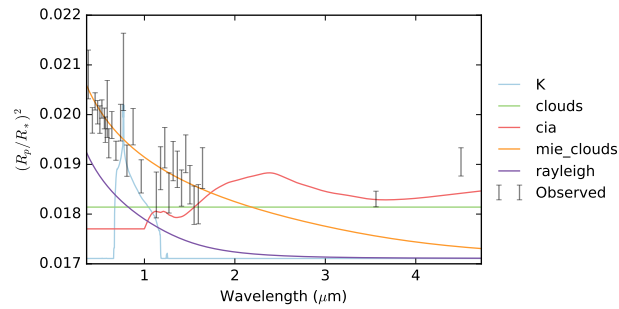
FIGURE A.6: The opacity contributions for each of the parameters in the highest evidence model for HAT-P-12b.
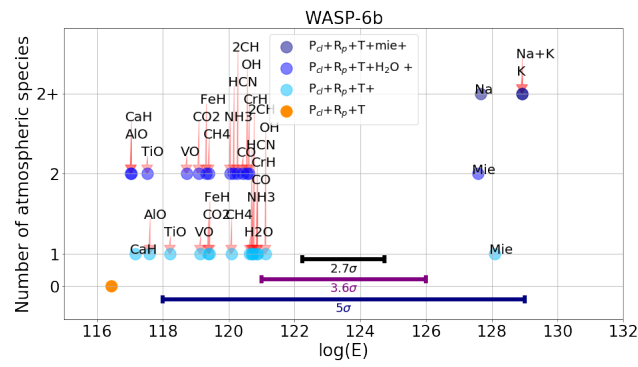
A.3 HAT-P-26b

FIGURE A.7: Model comparison HAT-P-26b, see caption of Figure A.1.

FIGURE A.8: Posterior of the retrieval for HAT-P-26b.

FIGURE A.9: The opacity contributions for each of the parameters in the highest evidence model for HAT-P-26b.

A.4   HD 189733b

FIGURE A.10: Posterior of the retrieval for HD 189733b.

A.5   HD 209458b
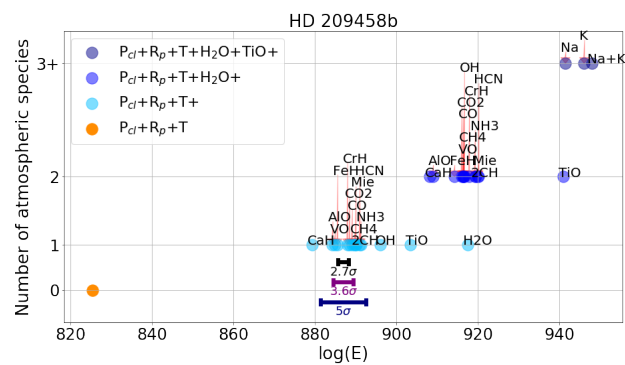
FIGURE A.11: Model comparison HD 209458b, see caption of Figure A.1.
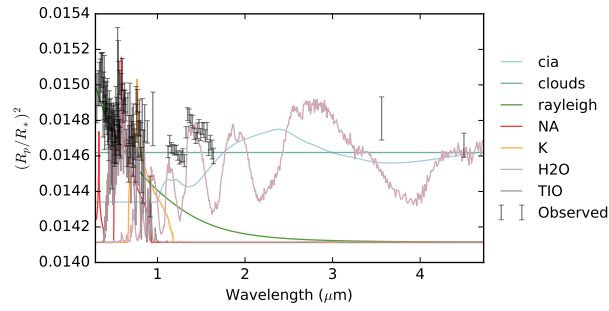
FIGURE A.12: Individual opacity contributions of the different atmospheric
constituents in the highest evidence model of HD 209458b.

A.6   WASP-6b

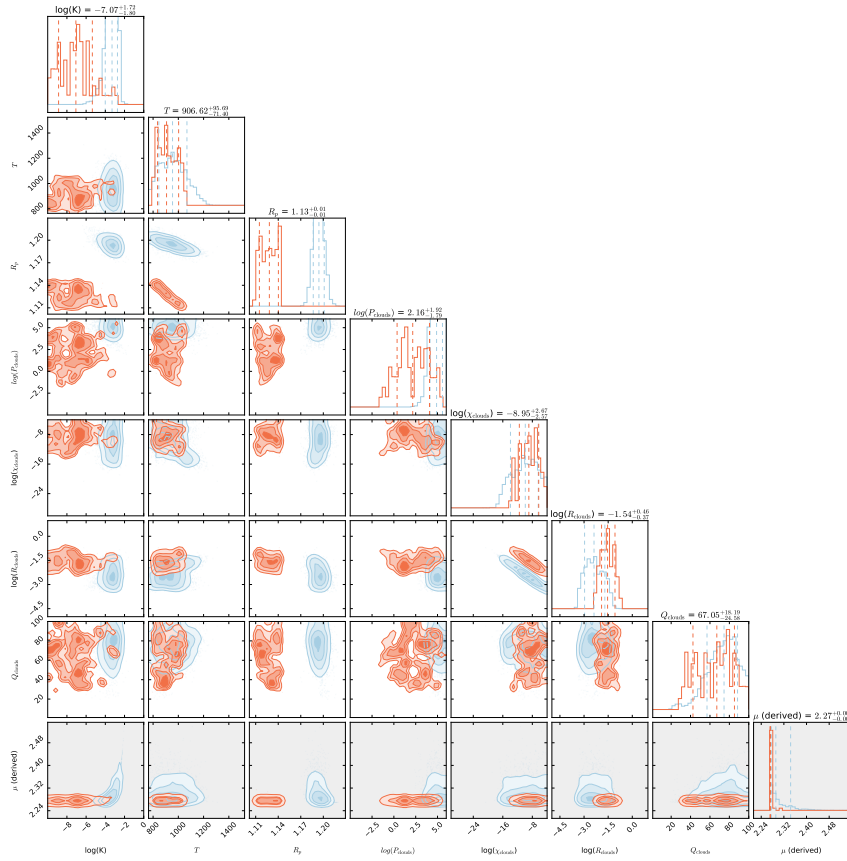FIGURE A.13: Model comparison WASP-6b, see caption of Figure A.1.

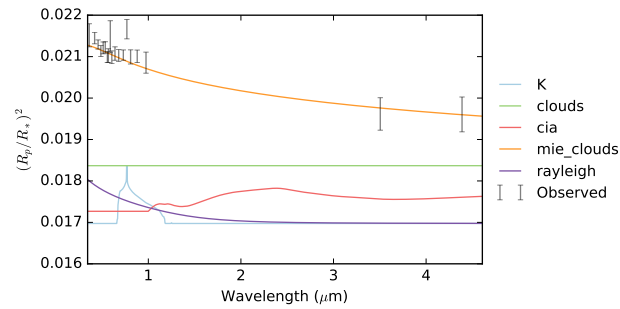FIGURE A.14: Posterior of the retrieval for WASP-6b.

FIGURE A.15: The opacity contributions for each of the parameters in the highest evidence model for WASP-6b.
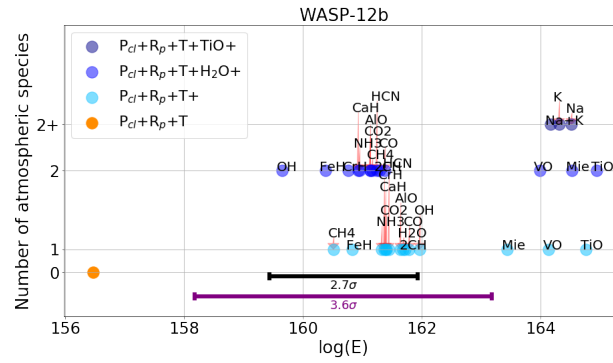
A.7   WASP-12b

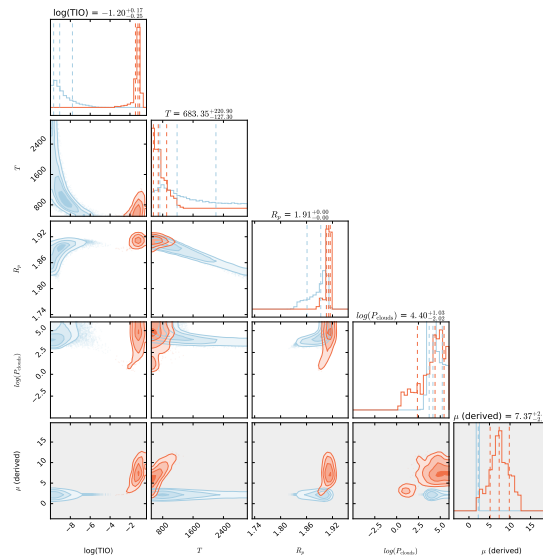FIGURE A.16: Model comparison WASP-12b, see caption of Figure A.1.

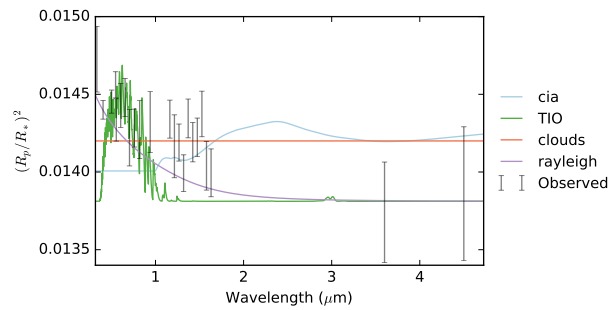FIGURE A.17: Posterior of the retrieval for WASP-12b.

FIGURE A.18: The opacity contributions for each of the parameters in the highest evidence model for WASP-12b.
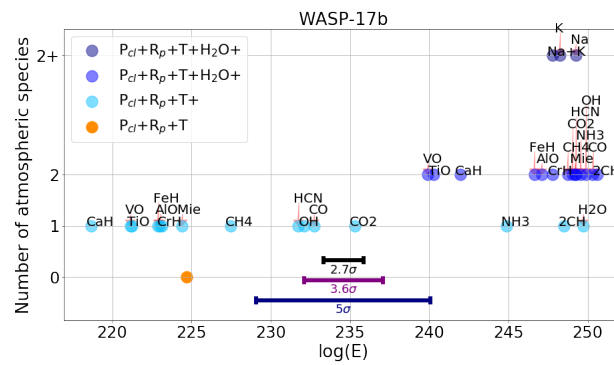
A.8   **WASP-17b**

FIGURE A.19: Model comparison WASP-17b, see caption of Figure A.1.

FIGURE A.20: Posterior of the retrieval for WASP-17b.

FIGURE A.21: The opacity contributions for each of the parameters in the
highest evidence model for WASP-17b.

A.9 WASP-19b

FIGURE A.22: The posterior distributions of the retrieved parameters for the highest evidence model for WASP-19b.

FIGURE A.23: The opacity contributions for each of the parameters in the highest evidence model for WASP-19b.

A.10   WASP-31b

FIGURE A.24: The posterior distributions of the retrieved parameters for the highest evidence model for WASP-31b.

FIGURE A.25: The opacity contributions for each of the parameters in the highest evidence model for WASP-31b.

A.11   WASP-52b

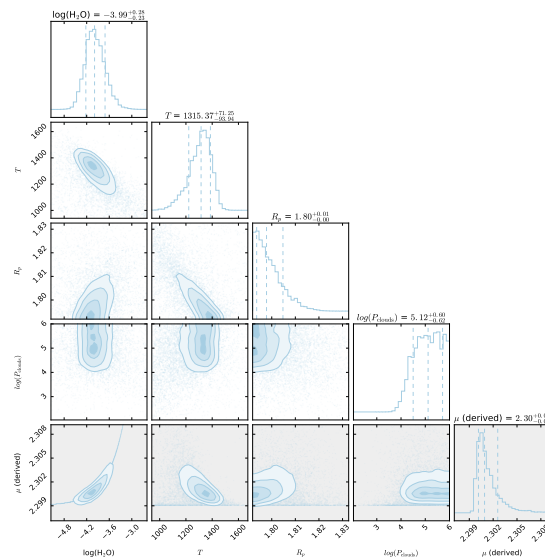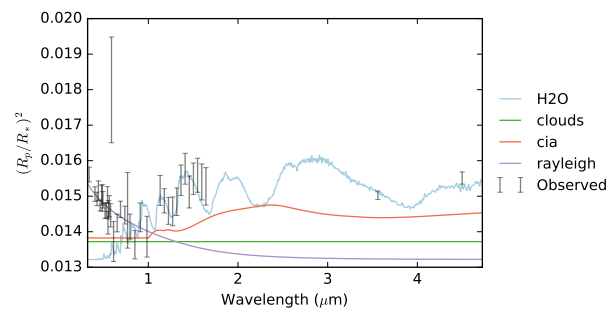FIGURE A.26: Model comparison WASP-52b, see caption of Figure A.1.

FIGURE A.27: Posterior of the retrieval for WASP-52b.

FIGURE A.28: The opacity contributions for each of the parameters in the highest evidence model for WASP-52b.

A.12 WASP-43b

FIGURE A.29: The posterior distributions of the retrieved parameters for the highest evidence model for WASP-43b.
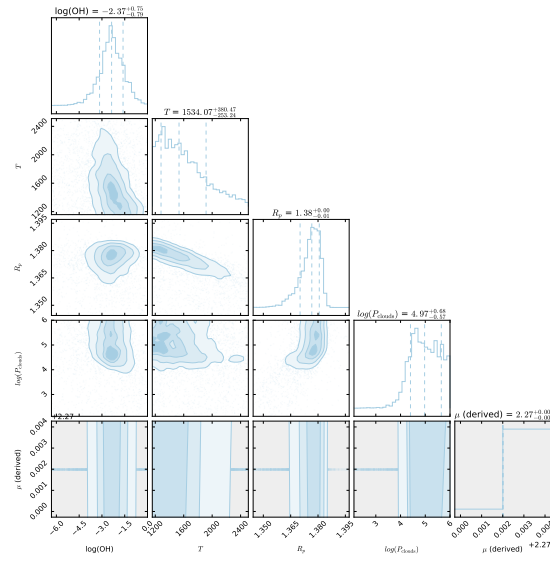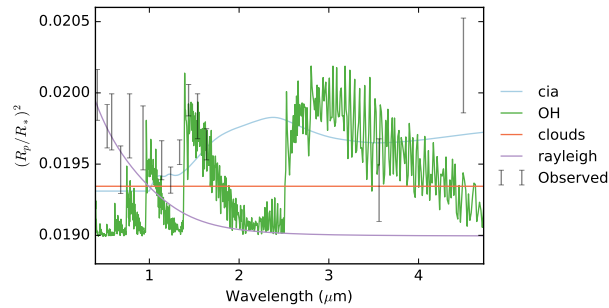
A.13 WASP-101b

FIGURE A.30: The posterior distributions of the retrieved parameters for the highest evidence model for WASP-101b.

FIGURE A.31: The opacity contributions for each of the parameters in the highest evidence model for WASP-101b.

A.14 WASP-107b

FIGURE A.32: Model comparison WASP-107b, see caption of Figure A.1. Note that the retrievals including Na and K are absent, since this planet lacks optical coverage.
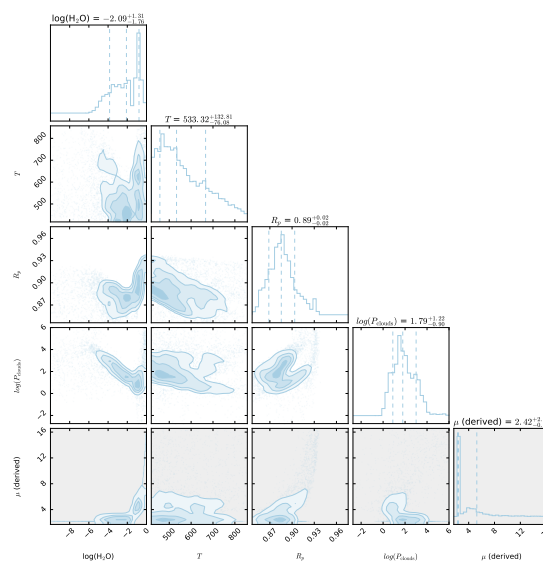
FIGURE A.33: Posterior of the retrieval for WASP-107b.
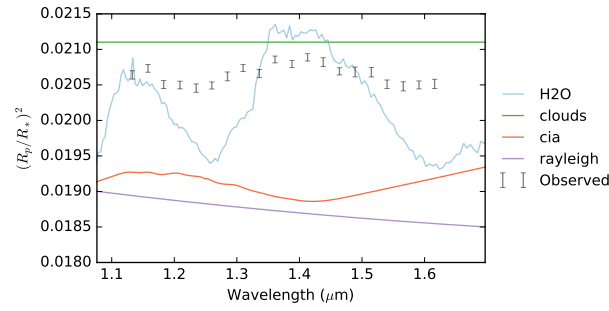
FIGURE A.34: The opacity contributions for each of the parameters in the
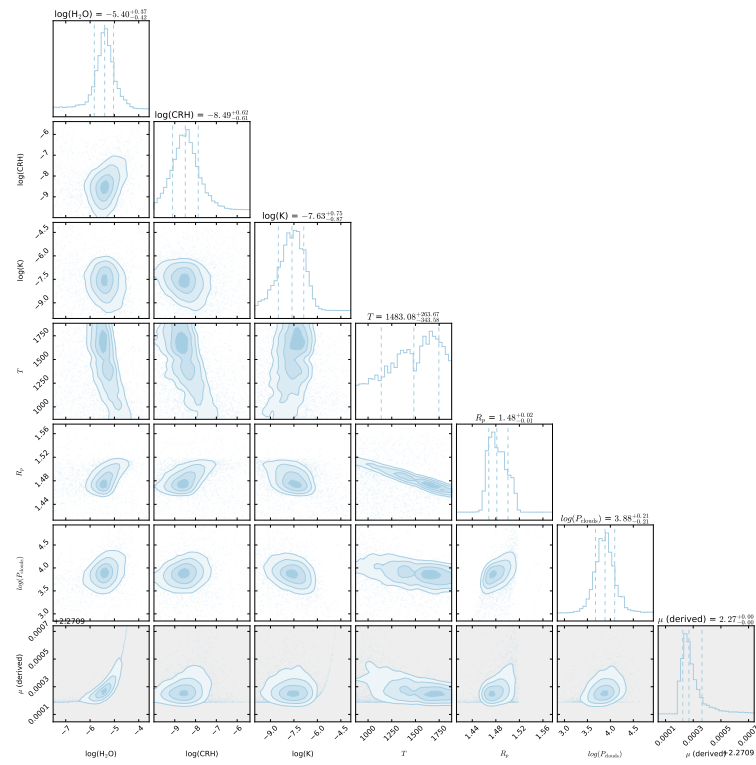highest evidence model for WASP-107b.

A.15   WASP-121b
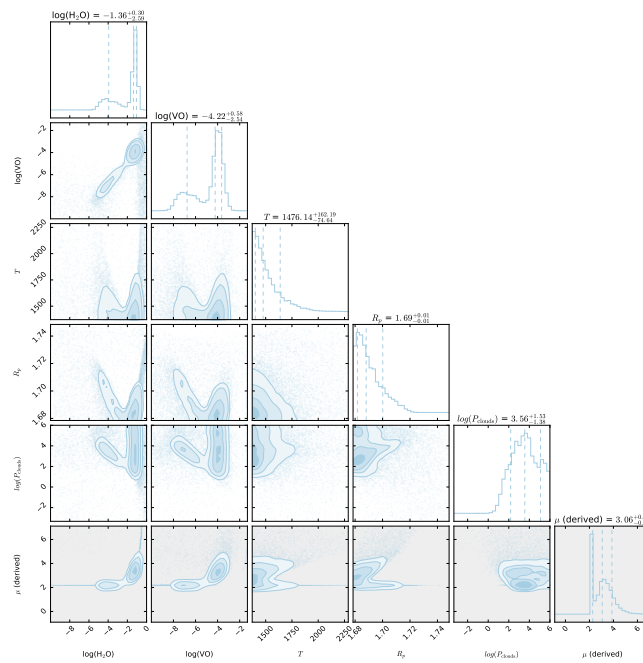
FIGURE A.35: The posterior distributions of the retrieved parameters for the
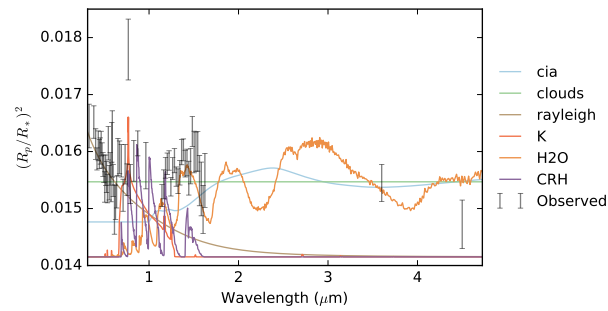highest evidence model for WASP-121b.
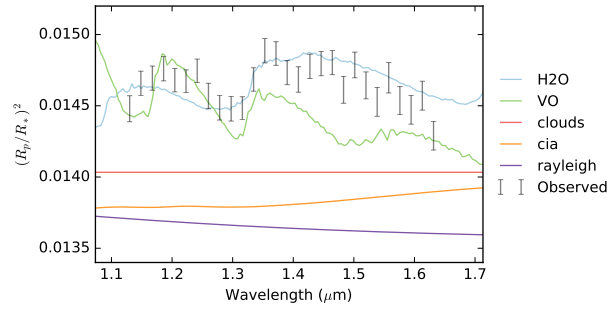
FIGURE A.36: The opacity contributions for each of the parameters in the highest evidence model for WASP-121b.
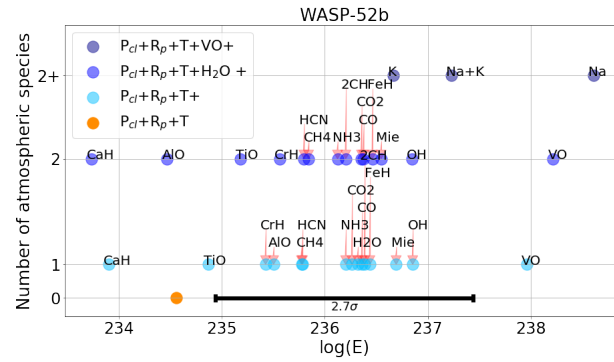
A.16 XO-1b
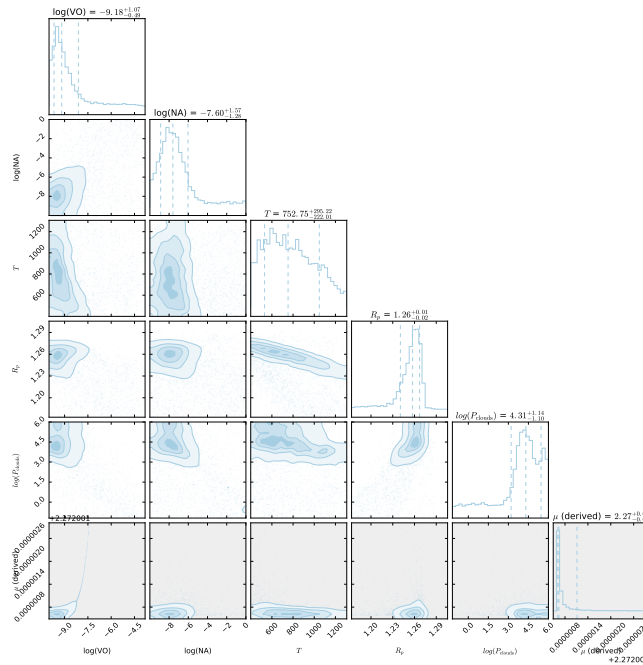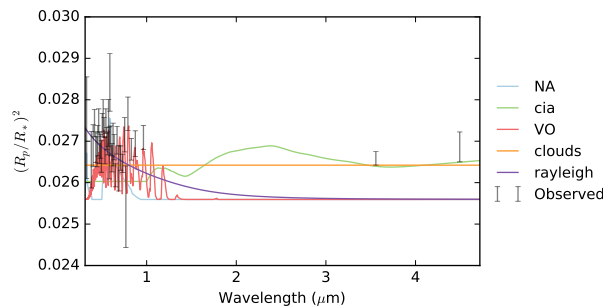

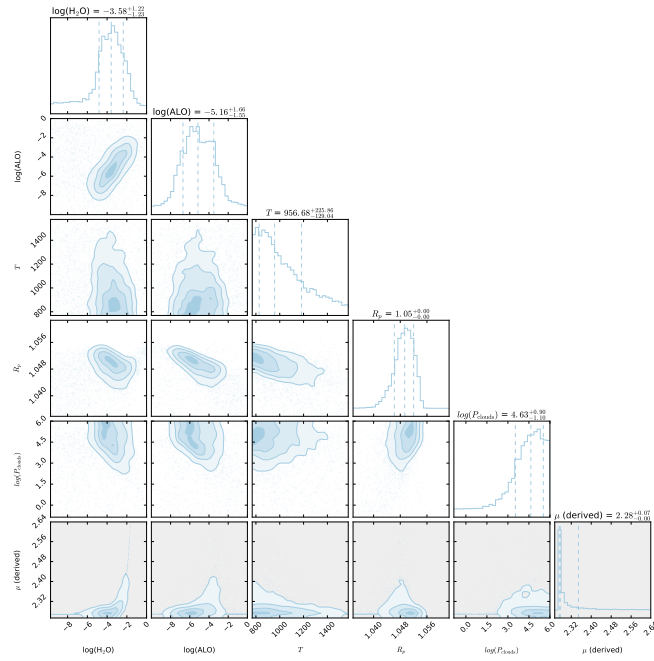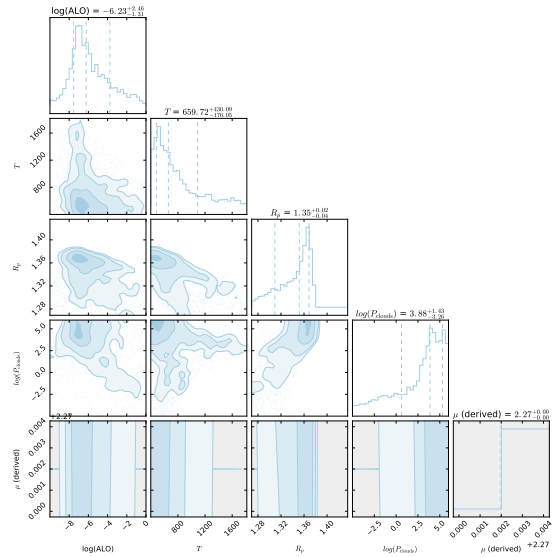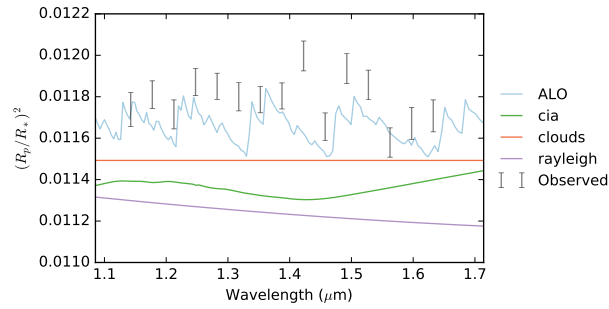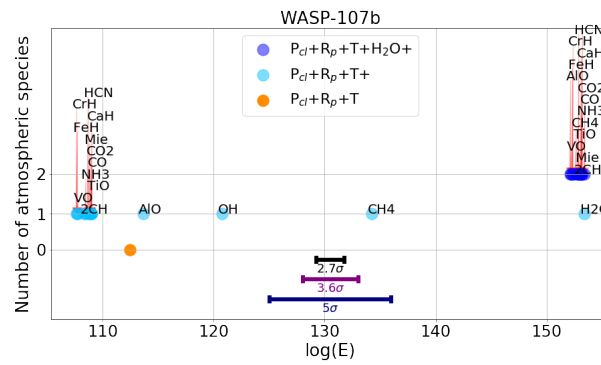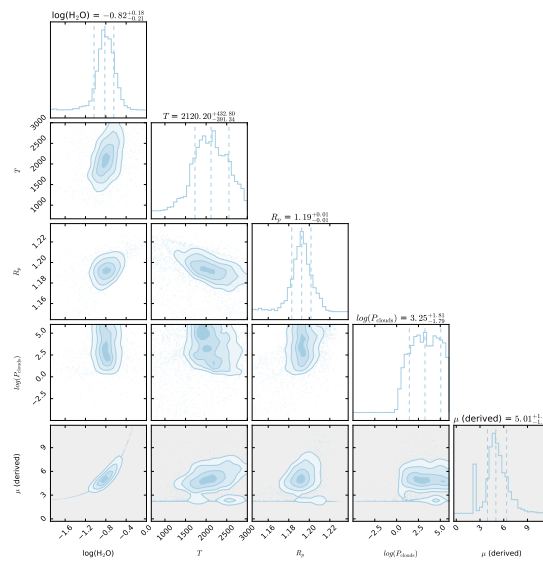FIGURE A.37: Posterior of the retrieval for XO-1b.
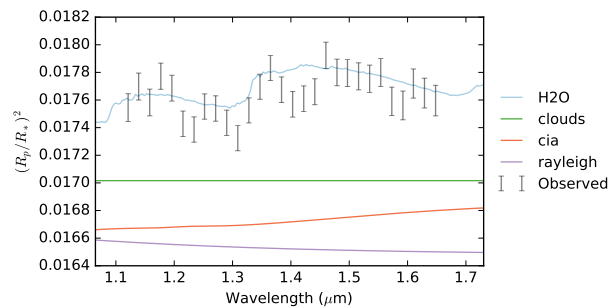
FIGURE A.38: The opacity contributions for each of the parameters in the highest evidence model for XO-1b.

Appendix B

Theory

B.1 Equilibrium temperatures

A first-order approximation of planetary temperatures can be made through the concept of equilibrium temperature. This is the surface blackbody temperature that is derived by balancing the incoming stellar flux by the atmospheric absorption and outgoing thermal re-radiation. Using the Stefan-Boltzmann law for re-radiation and ignoring other heat sources (greenhouse effect, internal heating, etc.) it can be written as:

$$T_{eq} = \frac{L_*(1-A)}{16\pi a^2 f \sigma} \tag{B.1}$$

Where f is the heat redistribution factor describing the effectiveness of atmospheric circulation and heat transfer. It is generally assumed that $f = 1$ for isotropic planetary emission and $f = 0.5$ if only the planet day-side re-radiates the energy, which would be the case for a tidally-locked planet without heat redistribution. A is the Bond albedo, which gives the fraction of energy re-emitted relative to the amount received integrated over all wavelengths. The lower bound for the planetary temperatures has been calculated assuming isotropic planetary emission and a Bond albedo of 0.9, which is high compared to the Solar System (highest value is 0.77 for Venus). The upper bound is calculated using Mercury's Bond albedo of 0.12 and planetary emission only from the day-side hemisphere. The prior isothermal atmospheric temperature has been calculated assuming isotropic planetary emission and Jupiter's Bond albedo of 0.34. The resulting values are shown in Table 2.4.

Bibliography

Adel, A. (1937). A Determination of the amount of Carbon Dioxide above the Reflecting Layer in the Atmosphere of the Planet Venus. ApJ, *85*, 345. https://doi.org/10.1086/143832

Adel, A., & Slipher, V. M. (1934). The Constitution of the Atmospheres of the Giant Planets. *Physical Review*, *46*(10), 902–906. https://doi.org/10.1103/PhysRev.46.902

Alam, M. K., Nikolov, N., López-Morales, M., Sing, D. K., Goyal, J. M., Henry, G. W., Sanz-Forcada, J., Williamson, M. H., Evans, T. M., Wakeford, H. R., Bruno, G., Ballester, G. E., Stevenson, K. B., Lewis, N. K., Barstow, J. K., Bourrier, V., Buchhave, L. A., Ehrenreich, D., & Garcıa Muñoz, A. (2018). The HST PanCET Program: Hints of Na I and Evidence of a Cloudy Atmosphere for the Inflated Hot Jupiter WASP-52b. AJ, *156*(6), arXiv 1811.00935, 298. https://doi.org/10.3847/1538-3881/aaee89

Allard, N. F., Spiegelman, F., & Kielkopf, J. F. (2016). K-H_2 line shapes for the spectra of cool brown dwarfs. *A&A*, *589*, A21. https://doi.org/10.1051/0004-6361/201628270

Allard, N. F., Spiegelman, F., Leininger, T., & Mollière, P. (2019). New study of the line profiles of sodium perturbed by H_2. *A&A*, *628*, A120. https://doi.org/10.1051/0004-6361/201935593

Al-Refaie, A. F., Changeat, Q., Waldmann, I. P., & Tinetti, G. (2019). TauREx III: A fast, dynamic and extendable framework for retrievals. *arXiv e-prints*, arXiv 1912.07759, arXiv:1912.07759.

Anderson, D. R., Collier Cameron, A., Delrez, L., Doyle, A. P., Gillon, M., Hellier, C., Jehin, E., Lendl, M., Maxted, P. F. L., Madhusudhan, N., Pepe, F., Pollacco, D., Queloz, D., Ségransan, D., Smalley, B., Smith, A. M. S., Triaud, A. H. M. J., Turner, O. D., Udry, S., & West, R. G. (2017). The discoveries of WASP-91b, WASP-105b and WASP-107b: Two warm Jupiters and a planet in the transition region between ice giants and gas giants. A&A, *604*arXiv 1701.03776, A110. https://doi.org/10.1051/0004-6361/201730439

Asplund, M., Grevesse, N., Sauval, A. J., & Scott, P. (2009). The Chemical Composition of the Sun. ARA&A, *47*(1), arXiv 0909.0948, 481–522. https://doi.org/10.1146/annurev.astro.46.060407.145222

Atkins, P., & De Paula, J. (2014). *Physical chemistry*. Oxford University Press.

Atreya, S. K., & Wong, A.-S. (2005). Coupled Clouds and Chemistry of the Giant Planets— A Case for Multiprobes. Space Sci. Rev., *116*(1-2), 121–136. https://doi.org/10.1007/s11214-005-1951-5

Barber, R. J., Strange, J. K., Hill, C., Polyansky, O. L., Mellau, G. C., Yurchenko, S. N., & Tennyson, J. (2014). ExoMol line lists – III. An improved hot rotation-vibration line list for HCN and HNC. MNRAS, *437*, 1828–1835. https://doi.org/10.1093/mnras/stt2011

Barstow, J. K., Aigrain, S., Irwin, P. G. J., Kendrew, S., & Fletcher, L. N. (2015). Transit spectroscopy with James Webb Space Telescope: systematics, starspots and stitching. MNRAS, *448*(3), arXiv 1501.06349, 2546–2561. https://doi.org/10.1093/mnras/stv186

Barstow, J. K., Aigrain, S., Irwin, P. G. J., & Sing, D. K. (2017). A Consistent Retrieval Analysis of 10 Hot Jupiters Observed in Transmission. ApJ, *834*(1), arXiv 1610.01841, 50. https://doi.org/10.3847/1538-4357/834/1/50

Bean, J. L., Stevenson, K. B., Batalha, N. M., Berta-Thompson, Z., Kreidberg, L., Crouzet, N., Benneke, B., Line, M. R., Sing, D. K., Wakeford, H. R., Knutson, H. A., Kempton, E. M. .-.-R., Désert, J.-M., Crossfield, I., Batalha, N. E., de Wit, J., Parmentier, V., Harrington, J., Moses, J. I., . . . Zingales, T. (2018). The Transiting Exoplanet Community

Early Release Science Program for JWST. PASP, *130*(993), arXiv 1803.04985, 114402. https://doi.org/10.1088/1538-3873/aadbf3

Beichman, C., Benneke, B., Knutson, H., Smith, R., Lagage, P.-O., Dressing, C., Latham, D., Lunine, J., Birkmann, S., Ferruit, P., Giardino, G., Kempton, E., Carey, S., Krick, J., Deroo, P. D., Mand ell, A., Ressler, M. E., Shporer, A., Swain, M., . . . Sing, D. (2014). Observations of Transiting Exoplanets with the James Webb Space Telescope (JWST). PASP, *126*(946), 1134. https://doi.org/10.1086/679566

Benneke, B., & Seager, S. (2012). Atmospheric Retrieval for Super-Earths: Uniquely Constraining the Atmospheric Composition with Transmission Spectroscopy. ApJ, *753*(2), arXiv 1203.4018, 100. https://doi.org/10.1088/0004-637X/753/2/100

Bernath, P. F. (2020). MoLLIST: Molecular line lists, intensities and spectra. *J. Quant. Spectrosc. Radiat. Transf.*, *240*, 106687. https://doi.org/10.1016/j.jqsrt.2019.106687

Bonomo, A. S., Desidera, S., Benatti, S., Borsa, F., Crespi, S., Damasso, M., Lanza, A. F., Sozzetti, A., Lodato, G., Marzari, F., Boccato, C., Claudi, R. U., Cosentino, R., Covino, E., Gratton, R., Maggio, A., Micela, G., Molinari, E., Pagano, I., . . . Scand ariato, G. (2017). The GAPS Programme with HARPS-N at TNG . XIV. Investigating giant planet migration history via improved eccentricity and mass determination for 231 transiting planets. A&A, *602*arXiv 1704.00373, A107. https://doi.org/10.1051/0004-6361/201629882

Borucki, W. J., Koch, D. G., Basri, G., Batalha, N., Brown, T. M., Bryson, S. T., Caldwell, D., Christensen-Dalsgaard, J., Cochran, W. D., DeVore, E., Dunham, E. W., Gautier, I., Thomas N., Geary, J. C., Gilliland, R., Gould, A., Howell, S. B., Jenkins, J. M., Latham, D. W., Lissauer, J. J., . . . Still, M. (2011). Characteristics of Planetary Candidates Observed by Kepler. II. Analysis of the First Four Months of Data. ApJ, *736*(1), arXiv 1102.0541, 19. https://doi.org/10.1088/0004-637X/736/1/19

Borysow, A. (2002). Collision-induced absorption coefficients of H_2 pairs at temperatures from 60 K to 1000 K. A&A, *390*, 779–782. https://doi.org/10.1051/0004-6361:20020555

Bourrier, V., Wheatley, P. J., Lecavelier des Etangs, A., King, G., Louden, T., Ehrenreich, D., Fares, R., Helling, C., Llama, J., Jardine, M. M., & Vidotto, A. A. (2020). MOVES III. Simultaneous X-ray and ultraviolet observations unveiling the variable environment of the hot Jupiter HD 189733b. MNRAS, *493*(1), arXiv 2001.11048, 559–579. https://doi.org/10.1093/mnras/staa256

Brewer, J. M., Fischer, D. A., Valenti, J. A., & Piskunov, N. (2016). Spectral Properties of Cool Stars: Extended Abundance Analysis of 1,617 Planet-search Stars. ApJS, *225*(2), arXiv 1606.07929, 32. https://doi.org/10.3847/0067-0049/225/2/32

Brewer, J. M., Fischer, D. A., & Madhusudhan, N. (2017). C/O and O/H Ratios Suggest Some Hot Jupiters Originate Beyond the Snow Line. AJ, *153*(2), arXiv 1612.04372, 83. https://doi.org/10.3847/1538-3881/153/2/83

Bruno, G., Lewis, N. K., Stevenson, K. B., Filippazzo, J., Hill, M., Fraine, J. D., Wakeford, H. R., Deming, D., López-Morales, M., & Alam, M. K. (2018). Starspot Occultations in Infrared Transit Spectroscopy: The Case of WASP-52b. AJ, *156*(3), arXiv 1808.09514, 124. https://doi.org/10.3847/1538-3881/aac6db

Burrows, A., Hubbard, W. B., Lunine, J. I., & Liebert, J. (2001). The theory of brown dwarfs and extrasolar giant planets. *Reviews of Modern Physics*, *73*(3), arXiv astro-ph/0103383, 719–765. https://doi.org/10.1103/RevModPhys.73.719

Burrows, A., Ram, R. S., Bernath, P., Sharp, C. M., & Milsom, J. A. (2002). New CrH opacities for the study of l and brown dwarf atmospheres. *Astrophys. J.*, *577*(2), 986–992. https://doi.org/10.1086/342242

Caldas, A., Leconte, J., Selsis, F., Waldmann, I. P., Bordé, P., Rocchetto, M., & Charnay, B. (2019). Effects of a fully 3D atmospheric structure on exoplanet transmission spectra: retrieval biases due to day-night temperature gradients. A&A, *623*arXiv 1901.09932, A161. https://doi.org/10.1051/0004-6361/201834384

Carter, A. L., Nikolov, N., Sing, D. K., Alam, M. K., Goyal, J. M., Mikal-Evans, T., Wakeford, H. R., Henry, G. W., Morrell, S., López-Morales, M., Smalley, B., Lavvas, P., Barstow, J. K., Garcıa Muñoz, A., Gibson, N. P., & Wilson, P. A. (2020). Detection of Na, K, and H_2O in the hazy atmosphere of WASP-6b. MNRAS, *494*(4), arXiv 1911.12628, 5449–5472. https://doi.org/10.1093/mnras/staa1078

Chapman, S. (1930). Xxxv. on ozone and atomic oxygen in the upper atmosphere. *The London, Edinburgh, and Dublin Philosophical Magazine and Journal of Science*, *10*(64), 369–383.

Charbonneau, D., Brown, T. M., Noyes, R. W., & Gilliland, R. L. (2002). Detection of an Extrasolar Planet Atmosphere. ApJ, *568*(1), arXiv astro-ph/0111544, 377–384. https://doi.org/10.1086/338770

Chubb, K. L., Rocchetto, M., Al-Refaie, A. F., Waldmann, I., Min, M., Barstow, J., Molliére, P., Phillips, M., Tennyson, J., & Yurchenko, S. N. (2020a). *(In prep.)*

Chubb, K. L., Tennyson, J., & Yurchenko, S. N. (2020b). Exomol molecular line lists - xxxvii: Spectra of acetylene. MNRAS, *493*(2), 1531–1545. https://doi.org/10.1093/mnras/staa229

Chubb, K. L., Min, M., Kawashima, Y., Helling, C., & Waldmann, I. (2020c). Aluminium oxide in the atmosphere of hot Jupiter WASP-43b. *arXiv e-prints*, arXiv 2004.13679, arXiv:2004.13679.

Clanton, C., & Gaudi, B. S. (2014). Synthesizing Exoplanet Demographics from Radial Velocity and Microlensing Surveys. II. The Frequency of Planets Orbiting M Dwarfs. ApJ, *791*(2), arXiv 1404.7500, 91. https://doi.org/10.1088/0004-637X/791/2/91

Coles, P. A., Yurchenko, S. N., & Tennyson, J. (2019). ExoMol molecular line lists - XXXV. A rotation-vibration line list for hot ammonia. MNRAS, *490*(4), arXiv 1911.10369, 4638–4647. https://doi.org/10.1093/mnras/stz2778

Cooper, C. S., & Showman, A. P. (2006). Dynamics and Disequilibrium Carbon Chemistry in Hot Jupiter Atmospheres, with Application to HD 209458b. ApJ, *649*(2), arXiv astro-ph/0602477, 1048–1063. https://doi.org/10.1086/506312

Crossfield, I. J. M. (2015). Observations of Exoplanet Atmospheres. PASP, *127*(956), arXiv 1507.03966, 941. https://doi.org/10.1086/683115

De Pater, I., & Lissauer, J. J. (2015). *Planetary sciences*. Cambridge University Press.

Delrez, L., Santerne, A., Almenara, J. .-.-M., Anderson, D. R., Collier-Cameron, A., Dıaz, R. F., Gillon, M., Hellier, C., Jehin, E., Lendl, M., Maxted, P. F. L., Neveu-VanMalle, M., Pepe, F., Pollacco, D., Queloz, D., Ségransan, D., Smalley, B., Smith, A. M. S., Triaud, A. H. M. J., . . . West, R. G. (2016). WASP-121 b: a hot Jupiter close to tidal disruption transiting an active F star. MNRAS, *458*(4), arXiv 1506.02471, 4025–4043. https://doi.org/10.1093/mnras/stw522

Deming, D., Harrington, J., Seager, S., & Richardson, L. J. (2006). Strong Infrared Emission from the Extrasolar Planet HD 189733b. ApJ, *644*(1), arXiv astro-ph/0602443, 560–564. https://doi.org/10.1086/503358

Deming, D., Wilkins, A., McCullough, P., Burrows, A., Fortney, J. J., Agol, E., Dobbs-Dixon, I., Madhusudhan, N., Crouzet, N., Desert, J.-M., Gilliland, R. L., Haynes, K., Knutson, H. A., Line, M., Magic, Z., Mand ell, A. M., Ranjan, S., Charbonneau, D., Clampin, M., . . . Showman, A. P. (2013). Infrared Transmission Spectroscopy of the Exoplanets HD 209458b and XO-1b Using the Wide Field Camera-3 on the Hubble Space Telescope. ApJ, *774*(2), arXiv 1302.1141, 95. https://doi.org/10.1088/0004-637X/774/2/95

Désert, J., Vidal-Madjar, A., Lecavelier Des Etangs, A., Sing, D., Ehrenreich, D., Hébrard, G., & Ferlet, R. (2008). TiO and VO broad band absorption features in the optical spectrum of the atmosphere of the hot-Jupiter <ASTROBJ>HD 209458b</ASTROBJ>. A&A, *492*(2), arXiv 0809.1865, 585–592. https://doi.org/10.1051/0004-6361:200810355

Evans, T. M., Sing, D. K., Wakeford, H. R., Nikolov, N., Ballester, G. E., Drummond, B., Kataria, T., Gibson, N. P., Amundsen, D. S., & Spake, J. (2016). Detection of H_2O and Evidence for TiO/VO in an Ultra-hot Exoplanet Atmosphere. ApJ, *822*(1), arXiv 1604.02310, L4. https://doi.org/10.3847/2041-8205/822/1/L4

Evans, T. M., Sing, D. K., Kataria, T., Goyal, J., Nikolov, N., Wakeford, H. R., Deming, D., Marley, M. S., Amundsen, D. S., Ballester, G. E., Barstow, J. K., Ben-Jaffel, L., Bourrier, V., Buchhave, L. A., Cohen, O., Ehrenreich, D., Garcıa Muñoz, A., Henry, G. W., Knutson, H., . . . Lupu, R. (2017). An ultrahot gas-giant exoplanet with a stratosphere. Nature, *548*(7665), arXiv 1708.01076, 58–61. https://doi.org/10.1038/nature23266

Faedi, F., Barros, S. C. C., Anderson, D. R., Brown, D. J. A., Collier Cameron, A., Pollacco, D., Boisse, I., Hébrard, G., Lendl, M., Lister, T. A., Smalley, B., Street, R. A., Triaud, A. H. M. J., Bento, J., Bouchy, F., Butters, O. W., Enoch, B., Haswell, C. A., Hellier, C.,

... Wheatley, P. J. (2011). WASP-39b: a highly inflated Saturn-mass planet orbiting a late G-type star. A&A, *531*arXiv 1102.1375, A40. https://doi.org/10.1051/0004-6361/201116671

Feroz, F., & Hobson, M. P. (2008). Multimodal nested sampling: an efficient and robust alternative to Markov Chain Monte Carlo methods for astronomical data analyses. MNRAS, *384*(2), arXiv 0704.3704, 449–463. https://doi.org/10.1111/j.1365-2966.2007.12353.x

Feroz, F., Hobson, M. P., & Bridges, M. (2009). MULTINEST: an efficient and robust Bayesian inference tool for cosmology and particle physics. MNRAS, *398*(4), arXiv 0809.3437, 1601–1614. https://doi.org/10.1111/j.1365-2966.2009.14548.x

Fischer, D. A., Howard, A. W., Laughlin, G. P., Macintosh, B., Mahadevan, S., Sahlmann, J., & Yee, J. C. (2014). Exoplanet Detection Techniques (H. Beuther, R. S. Klessen, C. P. Dullemond, & T. Henning, Eds.). In H. Beuther, R. S. Klessen, C. P. Dullemond, & T. Henning (Eds.), *Protostars and planets vi*. https://doi.org/10.2458/azu_uapress_9780816531240-ch031

Fisher, C., & Heng, K. (2018). Retrieval analysis of 38 WFC3 transmission spectra and resolution of the normalization degeneracy. MNRAS, *481*(4), arXiv 1809.06894, 4698–4727. https://doi.org/10.1093/mnras/sty2550

Fortney, J. J., Lodders, K., Marley, M. S., & Freedman, R. S. (2008). A Unified Theory for the Atmospheres of the Hot and Very Hot Jupiters: Two Classes of Irradiated Atmospheres. ApJ, *678*(2), arXiv 0710.2558, 1419–1435. https://doi.org/10.1086/528370

Gaia Collaboration, Brown, A. G. A., Vallenari, A., Prusti, T., de Bruijne, J. H. J., Babusiaux, C., Bailer-Jones, C. A. L., Biermann, M., Evans, D. W., Eyer, L., Jansen, F., Jordi, C., Klioner, S. A., Lammers, U., Lindegren, L., Luri, X., Mignard, F., Panem, C., Pourbaix, D., ... Zwitter, T. (2018). Gaia Data Release 2. Summary of the contents and survey properties. A&A, *616*arXiv 1804.09365, A1. https://doi.org/10.1051/0004-6361/201833051

Gaudi, B. S., Seager, S., & Mallen-Ornelas, G. (2005). On the Period Distribution of Close-in Extrasolar Giant Planets. ApJ, *623*(1), arXiv astro-ph/0409443, 472–481. https://doi.org/10.1086/428478

Gladstone, G. R., Stern, S. A., Ennico, K., Olkin, C. B., Weaver, H. A., Young, L. A., Summers, M. E., Strobel, D. F., Hinson, D. P., Kammer, J. A., Parker, A. H., Steffl, A. J., Linscott, I. R., Parker, J. W., Cheng, A. F., Slater, D. C., Versteeg, M. H., Greathouse, T. K., Retherford, K. D., ... Zirnstein, E. (2016). The atmosphere of Pluto as observed by New Horizons. *Science*, *351*(6279), arXiv 1604.05356, aad8866. https://doi.org/10.1126/science.aad8866

Goicoechea, J. R., Swinyard, B., Tinetti, G., Nakagawa, T., Enya, K., Tamura, M., Ferlet, M., Isaak, K. G., Wyatt, M., Aylward, A. D., Barlow, M., Beaulieu, J. P., Boccaletti, A., Cernicharo, J., Cho, J., Claudi, R., Jones, H., Lammer, H., Leger, A., ... White, G. (2008). Using SPICA Space Telescope to characterize Exoplanets. *arXiv e-prints*, arXiv 0809.0242, arXiv:0809.0242.

Greene, T. P., Line, M. R., Montero, C., Fortney, J. J., Lustig-Yaeger, J., & Luther, K. (2016). Characterizing Transiting Exoplanet Atmospheres with JWST. ApJ, *817*(1), arXiv 1511.05528, 17. https://doi.org/10.3847/0004-637X/817/1/17

Griffith, C. A. (2014). Disentangling degenerate solutions from primary transit and secondary eclipse spectroscopy of exoplanets. *Philosophical Transactions of the Royal Society of London Series A*, *372*(2014), arXiv 1312.3988, 20130086–20130086. https://doi.org/10.1098/rsta.2013.0086

Guillot, T., Burrows, A., Hubbard, W. B., Lunine, J. I., & Saumon, D. (1996). Giant Planets at Small Orbital Distances. ApJ, *459*arXiv astro-ph/9511109, L35. https://doi.org/10.1086/309935

Heays, A. N., Bosman, A. D., & van Dishoeck, E. F. (2017). Photodissociation and photoionisation of atoms and molecules of astrophysical interest. A&A, *602*arXiv 1701.04459, A105. https://doi.org/10.1051/0004-6361/201628742

Helling, C. (2019). Exoplanet Clouds. *Annual Review of Earth and Planetary Sciences*, *47*arXiv 1812.03793, 583–606. https://doi.org/10.1146/annurev-earth-053018-060401

Heng, K., & Showman, A. P. (2015). Atmospheric Dynamics of Hot Exoplanets. *Annual Review of Earth and Planetary Sciences*, *43*arXiv 1407.4150, 509–540. https://doi.org/10.1146/annurev-earth-060614-105146

Heng, K., & Kitzmann, D. (2017). The theory of transmission spectra revisited: a semi-analytical method for interpreting WFC3 data and an unresolved challenge. MNRAS, *470*(3), arXiv 1702.02051, 2972–2981. https://doi.org/10.1093/mnras/stx1453

Hollis, M. D. J., Tessenyi, M., & Tinetti, G. (2013). TAU: A 1D radiative transfer code for transmission spectroscopy of extrasolar planet atmospheres. *Computer Physics Communications*, *184*(10), 2351–2361. https://doi.org/10.1016/j.cpc.2013.05.011

Huitson, C. M., Sing, D. K., Pont, F., Fortney, J. J., Burrows, A. S., Wilson, P. A., Ballester, G. E., Nikolov, N., Gibson, N. P., Deming, D., Aigrain, S., Evans, T. M., Henry, G. W., Lecavelier des Etangs, A., Showman, A. P., Vidal-Madjar, A., & Zahnle, K. (2013). An HST optical-to-near-IR transmission spectrum of the hot Jupiter WASP-19b: detection of atmospheric water and likely absence of TiO. MNRAS, *434*(4), arXiv 1307.2083, 3252–3274. https://doi.org/10.1093/mnras/stt1243

Irwin, P. G. J., Teanby, N. A., de Kok, R., Fletcher, L. N., Howett, C. J. A., Tsang, C. C. C., Wilson, C. F., Calcutt, S. B., Nixon, C. A., & Parrish, P. D. (2008). The NEMESIS planetary atmosphere radiative transfer and retrieval tool. J. Quant. Spec. Radiat. Transf., *109*, 1136–1150. https://doi.org/10.1016/j.jqsrt.2007.11.006

Jeffreys, H. (1998). *The theory of probability*. Oxford University Press.

Kass, R., & Raftery, A. (1995). Bayes factors. *Journal of the american statistical association*, *430*(90). https://www.tandfonline.com/doi/abs/10.1080/01621459.1995.10476572

Kawashima, Y., & Ikoma, M. (2019). Theoretical Transmission Spectra of Exoplanet Atmospheres with Hydrocarbon Haze: Effect of Creation, Growth, and Settling of Haze Particles. II. Dependence on UV Irradiation Intensity, Metallicity, C/O Ratio, Eddy Diffusion Coefficient, and Temperature. ApJ, *877*(2), 109. https://doi.org/10.3847/1538-4357/ab1b1d

Kempton, E. M. .-.-R., Bean, J. L., & Parmentier, V. (2017). An Observational Diagnostic for Distinguishing between Clouds and Haze in Hot Exoplanet Atmospheres. ApJ, *845*(2), arXiv 1705.05847, L20. https://doi.org/10.3847/2041-8213/aa84ac

Kirkpatrick, J. D., Allard, F., Bida, T., Zuckerman, B., Becklin, E. E., Chabrier, G., & Baraffe, I. (1999). An Improved Optical Spectrum and New Model FITS of the Likely Brown Dwarf GD 165B. ApJ, *519*(2), 834–843. https://doi.org/10.1086/307380

Knutson, H. A., Charbonneau, D., Allen, L. E., Fortney, J. J., Agol, E., Cowan, N. B., Showman, A. P., Cooper, C. S., & Megeath, S. T. (2007). A map of the day-night contrast of the extrasolar planet HD 189733b. Nature, *447*(7141), arXiv 0705.0993, 183–186. https://doi.org/10.1038/nature05782

Kramida, A., Ralchenko, Y., & Reader, J. (2013). NIST atomic spectra database – version 5 [http://www.nist.gov/pml/data/asd.cfm]. https://doi.org/10.18434/T4W30F

Kreidberg, L., Bean, J. L., Désert, J.-M., Line, M. R., Fortney, J. J., Madhusudhan, N., Stevenson, K. B., Showman, A. P., Charbonneau, D., McCullough, P. R., Seager, S., Burrows, A., Henry, G. W., Williamson, M., Kataria, T., & Homeier, D. (2014). A Precise Water Abundance Measurement for the Hot Jupiter WASP-43b. ApJ, *793*(2), arXiv 1410.2255, L27. https://doi.org/10.1088/2041-8205/793/2/L27

Kreidberg, L., Line, M. R., Bean, J. L., Stevenson, K. B., Désert, J.-M., Madhusudhan, N., Fortney, J. J., Barstow, J. K., Henry, G. W., Williamson, M. H., & Showman, A. P. (2015). A Detection of Water in the Transmission Spectrum of the Hot Jupiter WASP-12b and Implications for Its Atmospheric Composition. ApJ, *814*(1), arXiv 1504.05586, 66. https://doi.org/10.1088/0004-637X/814/1/66

Kreidberg, L., Line, M. R., Thorngren, D., Morley, C. V., & Stevenson, K. B. (2018). Water, High-altitude Condensates, and Possible Methane Depletion in the Atmosphere of the Warm Super-Neptune WASP-107b. ApJ, *858*(1), arXiv 1709.08635, L6. https://doi.org/10.3847/2041-8213/aabfce

Kuiper, G. P. (1944). Titan: a Satellite with an Atmosphere. ApJ, *100*, 378. https://doi.org/10.1086/144679

Lecavelier Des Etangs, A., Pont, F., Vidal-Madjar, A., & Sing, D. (2008a). Rayleigh scattering in the transit spectrum of HD 189733b. A&A, *481*(2), arXiv 0802.3228, L83–L86. https://doi.org/10.1051/0004-6361:200809388

Lecavelier Des Etangs, A., Pont, F., Vidal-Madjar, A., & Sing, D. (2008b). Rayleigh scattering in the transit spectrum of HD 189733b. A&A, *481*(2), arXiv 0802.3228, L83–L86. https://doi.org/10.1051/0004-6361:200809388

Lee, J.-M., Heng, K., & Irwin, P. G. J. (2013). Atmospheric Retrieval Analysis of the Directly Imaged Exoplanet HR 8799b. ApJ, *778*(2), arXiv 1307.1404, 97. https://doi.org/10.1088/0004-637X/778/2/97

Li, C., Ingersoll, A., Bolton, S., Levin, S., Janssen, M., Atreya, S., Lunine, J., Steffes, P., Brown, S., Guillot, T., Allison, M., Arballo, J., Bellotti, A., Adumitroaie, V., Gulkis, S., Hodges, A., Li, L., Misra, S., Orton, G., . . . Zhang, Z. (2020). The water abundance in Jupiter's equatorial zone. *Nature Astronomy*. https://doi.org/10.1038/s41550-020-1009-3

Li, G., Harrison, J. J., Ram, R. S., Western, C. M., & Bernath, P. F. (2012). Einstein A coefficients and absolute line intensities for the E $^2\Pi$ - X $^2\Sigma^+$ transition of CaH. *J. Quant. Spectrosc. Radiat. Transf.*, *113*, 67–74. https://doi.org/10.1016/j.jqsrt.2011.09.010

Li, G., Gordon, I. E., Rothman, L. S., Tan, Y., Hu, S.-M., Kassi, S., Campargue, A., & Medvedev, E. S. (2015). Rovibrational line lists for nine isotopologues of the co molecule in the x $^1\Sigma^+$ ground electronic state. *Astrophys. J. Suppl.*, *216*, 15. https://doi.org/10.1088/0067-0049/216/1/15

Liang, M., Parkinson, C. D., Lee, A. Y. .-.-T., Yung, Y. L., & Seager, S. (2003). Source of Atomic Hydrogen in the Atmosphere of HD 209458b. ApJ, *596*(2), arXiv astro-ph/0307037, L247–L250. https://doi.org/10.1086/379314

Line, M. R., Liang, M. C., & Yung, Y. L. (2010). High-temperature Photochemistry in the Atmosphere of HD 189733b. ApJ, *717*(1), arXiv 1004.4029, 496–502. https://doi.org/10.1088/0004-637X/717/1/496

Liou, K. (2002). *An introduction to atmospheric radiation*. Elsevier.

Lodders, K. (2010). Exoplanet Chemistry. In *Formation and evolution of exoplanets* (p. 157). https://doi.org/10.1002/9783527629763.ch8

Madhusudhan, N. (2012). C/O Ratio as a Dimension for Characterizing Exoplanetary Atmospheres. ApJ, *758*(1), arXiv 1209.2412, 36. https://doi.org/10.1088/0004-637X/758/1/36

Madhusudhan, N. (2019). Exoplanetary Atmospheres: Key Insights, Challenges, and Prospects. ARA&A, *57*arXiv 1904.03190, 617–663. https://doi.org/10.1146/annurev-astro-081817-051846

Madhusudhan, N., Crouzet, N., McCullough, P. R., Deming, D., & Hedges, C. (2014). H_2O Abundances in the Atmospheres of Three Hot Jupiters. ApJ, *791*(1), arXiv 1407.6054, L9. https://doi.org/10.1088/2041-8205/791/1/L9

Madhusudhan, N., & Seager, S. (2009). A Temperature and Abundance Retrieval Method for Exoplanet Atmospheres. ApJ, *707*(1), arXiv 0910.1347, 24–39. https://doi.org/10.1088/0004-637X/707/1/24

Mallonn, M., Nascimbeni, V., Weingrill, J., von Essen, C., Strassmeier, K. G., Piotto, G., Pagano, I., Scandariato, G., Csizmadia, S., Herrero, E., Sada, P. V., Dhillon, V. S., Marsh, T. R., Künstler, A., Bernt, I., & Granzer, T. (2015). Broad-band spectrophotometry of the hot Jupiter HAT-P-12b from the near-UV to the near-IR. A&A, *583*arXiv 1509.05272, A138. https://doi.org/10.1051/0004-6361/201425395

Mayor, M., & Queloz, D. (1995). A Jupiter-mass companion to a solar-type star. Nature, *378*(6555), 355–359. https://doi.org/10.1038/378355a0

McKemmish, L. K., Yurchenko, S. N., & Tennyson, J. (2016). ExoMol Molecular linelists – XVIII. The spectrum of Vanadium Oxide. MNRAS, *463*, 771–793. https://doi.org/10.1093/mnras/stw1969

McKemmish, L. K., Masseron, T., Hoeijmakers, H. J., Pérez-Mesa, V., Grimm, S. L., Yurchenko, S. N., & Tennyson, J. (2019). ExoMol molecular line lists – XXXIII. The spectrum of Titanium Oxide. MNRAS, *488*(2), 2836–2854. https://doi.org/10.1093/mnras/stz1818

Moses, J. I. (2014). Chemical kinetics on extrasolar planets. *Philosophical Transactions of the Royal Society of London Series A*, *372*(2014), arXiv 1307.5450, 20130073–20130073. https://doi.org/10.1098/rsta.2013.0073

Moses, J. I., Visscher, C., Fortney, J. J., Showman, A. P., Lewis, N. K., Griffith, C. A., Klippenstein, S. J., Shabram, M., Friedson, A. J., Marley, M. S., & Freedman, R. S. (2011). Disequilibrium Carbon, Oxygen, and Nitrogen Chemistry in the Atmospheres of

HD 189733b and HD 209458b. ApJ, *737*(1), arXiv 1102.0063, 15. https://doi.org/10.1088/0004-637X/737/1/15

Nikolov, N., Sing, D. K., Pont, F., Burrows, A. S., Fortney, J. J., Ballester, G. E., Evans, T. M., Huitson, C. M., Wakeford, H. R., Wilson, P. A., Aigrain, S., Deming, D., Gibson, N. P., Henry, G. W., Knutson, H., Lecavelier des Etangs, A., Showman, A. P., Vidal-Madjar, A., & Zahnle, K. (2014). Hubble Space Telescope hot Jupiter transmission spectral survey: a detection of Na and strong optical absorption in HAT-P-1b. MN-RAS, *437*(1), arXiv 1310.0083, 46–66. https://doi.org/10.1093/mnras/stt1859

Nikolov, N., Sing, D. K., Burrows, A. S., Fortney, J. J., Henry, G. W., Pont, F., Ballester, G. E., Aigrain, S., Wilson, P. A., Huitson, C. M., Gibson, N. P., Désert, J. .-.-M., Lecavelier Des Etangs, A., Showman, A. P., Vidal-Madjar, A., Wakeford, H. R., & Zahnle, K. (2015). HST hot-Jupiter transmission spectral survey: haze in the atmosphere of WASP-6b. MNRAS, *447*(1), arXiv 1411.4567, 463–478. https://doi.org/10.1093/mnras/stu2433

Öberg, K. I., Murray-Clay, R., & Bergin, E. A. (2011). The Effects of Snowlines on C/O in Planetary Atmospheres. ApJ, *743*(1), arXiv 1110.5567, L16. https://doi.org/10.1088/2041-8205/743/1/L16

Owen, J. E. (2019). Atmospheric Escape and the Evolution of Close-In Exoplanets. *Annual Review of Earth and Planetary Sciences*, *47*arXiv 1807.07609, 67–90. https://doi.org/10.1146/annurev-earth-053018-060246

Parmentier, V., Showman, A. P., & Lian, Y. (2013). 3D mixing in hot Jupiters atmospheres. I. Application to the day/night cold trap in HD 209458b. A&A, *558*arXiv 1301.4522, A91. https://doi.org/10.1051/0004-6361/201321132

Patrascu, A. T., Tennyson, J., & Yurchenko, S. N. (2015). ExoMol molecular linelists: VII: The spectrum of AlO. MNRAS, *449*, 3613–3619. https://doi.org/10.1093/mnras/stv507

Pinhas, A., Madhusudhan, N., Gandhi, S., & MacDonald, R. (2019). H_2O abundances and cloud properties in ten hot giant exoplanets. MNRAS, *482*(2), arXiv 1811.00011, 1485–1498. https://doi.org/10.1093/mnras/sty2544

Pluriel, W., Zingales, T., Leconte, J., & Parmentier, V. (2020). Strong biases in retrieved atmospheric composition caused by day-night chemical heterogeneities. A&A, *636*arXiv 2003.05943, A66. https://doi.org/10.1051/0004-6361/202037678

Pollack, J. B., Hubickyj, O., Bodenheimer, P., Lissauer, J. J., Podolak, M., & Greenzweig, Y. (1996). Formation of the Giant Planets by Concurrent Accretion of Solids and Gas. Icarus, *124*(1), 62–85. https://doi.org/10.1006/icar.1996.0190

Polyansky, O. L., Kyuberis, A. A., Zobov, N. F., Tennyson, J., Yurchenko, S. N., & Lodi, L. (2018). ExoMol molecular line lists XXX: a complete high-accuracy line list for water. MNRAS, *480*, 2597–2608. https://doi.org/10.1093/mnras/sty1877

Pont, F., Knutson, H., Gilliland, R. L., Moutou, C., & Charbonneau, D. (2008). Detection of atmospheric haze on an extrasolar planet: the 0.55-1.05 μm transmission spectrum of HD 189733b with the HubbleSpaceTelescope. MNRAS, *385*(1), arXiv 0712.1374, 109–118. https://doi.org/10.1111/j.1365-2966.2008.12852.x

Prinn, R. G., & Barshay, S. S. (1977). Carbon Monoxide on Jupiter and Implications for Atmospheric Convection. *Science*, *198*(4321), 1031–1034. https://doi.org/10.1126/science.198.4321.1031

Quanz, S. P., Crossfield, I., Meyer, M. R., Schmalzl, E., & Held, J. (2015). Direct detection of exoplanets in the 3-10 μm range with E-ELT/METIS. *International Journal of Astrobiology*, *14*(2), arXiv 1404.0831, 279–289. https://doi.org/10.1017/S1473550414000135

Richard, C., Gordon, I. E., Rothman, L. S., Abel, M., Frommhold, L., Gustafsson, M., Hartmann, J. .-.-M., Hermans, C., Lafferty, W. J., Orton, G. S., Smith, K. M., & Tran, H. (2012). New section of the HITRAN database: Collision-induced absorption (CIA). J. Quant. Spec. Radiat. Transf., *113*(11), 1276–1285. https://doi.org/10.1016/j.jqsrt.2011.11.004

Rothman, L. S., Gordon, I. E., Barber, R. J., Dothe, H., Gamache, R. R., Goldman, A., Perevalov, V. I., Tashkun, S. A., & Tennyson, J. (2010). HITEMP, the High-Temperature Molecular Spectroscopic Database. *J. Quant. Spectrosc. Radiat. Transf.*, *111*, 2139–2150.

Santos, N. C., Sousa, S. G., Mortier, A., Neves, V., Adibekyan, V., Tsantaki, M., Delgado Mena, E., Bonfils, X., Israelian, G., Mayor, M., & Udry, S. (2013). SWEET-Cat: A catalogue of parameters for Stars With ExoplanETs. I. New atmospheric parameters and masses

for 48 stars with planets. A&A, *556*arXiv 1307.0354, A150. https://doi.org/10.1051/0004-6361/201321286

Seager, S., & Deming, D. (2010). Exoplanet Atmospheres. ARA&A, *48*arXiv 1005.4037, 631–672. https://doi.org/10.1146/annurev-astro-081309-130837

Seager, S., & Sasselov, D. D. (2000). Theoretical Transmission Spectra during Extrasolar Giant Planet Transits. ApJ, *537*(2), arXiv astro-ph/9912241, 916–921. https://doi.org/10.1086/309088

Seager, S., Deming, D., & Valenti, J. A. (2009). Transiting Exoplanets with JWST. *Astrophysics and Space Science Proceedings*, *10*arXiv 0808.1913, 123. https://doi.org/10.1007/978-1-4020-9457-6_5

Sedaghati, E., Boffin, H. M. J., Jeřabková, T., Garcıa Muñoz, A., Grenfell, J. L., Smette, A., Ivanov, V. D., Csizmadia, S., Cabrera, J., Kabath, P., Rocchetto, M., & Rauer, H. (2016). Potassium detection in the clear atmosphere of a hot-Jupiter. FORS2 transmission spectroscopy of WASP-17b. A&A, *596*arXiv 1609.03906, A47. https://doi.org/10.1051/0004-6361/201629090

Seinfeld, J., & Pandis, S. (1998). *Atmospheric chemistry and physics : From air pollution to climate change*. Wiley.

Shiltsev, V. (2014). The 1761 discovery of Venus' atmosphere: Lomonosov and others. *Journal of Astronomical History and Heritage*, *17*(1), 85–112.

Showman, A. P., & Polvani, L. M. (2011). Equatorial Superrotation on Tidally Locked Exoplanets. ApJ, *738*(1), arXiv 1103.3101, 71. https://doi.org/10.1088/0004-637X/738/1/71

Sing, D. K., Lecavelier des Etangs, A., Fortney, J. J., Burrows, A. S., Pont, F., Wakeford, H. R., Ballester, G. E., Nikolov, N., Henry, G. W., Aigrain, S., Deming, D., Evans, T. M., Gibson, N. P., Huitson, C. M., Knutson, H., Showman, A. P., Vidal-Madjar, A., Wilson, P. A., Williamson, M. H., & Zahnle, K. (2013). HST hot-Jupiter transmission spectral survey: evidence for aerosols and lack of TiO in the atmosphere of WASP-12b. MN-RAS, *436*(4), arXiv 1309.5261, 2956–2973. https://doi.org/10.1093/mnras/stt1782

Sing, D. K., Wakeford, H. R., Showman, A. P., Nikolov, N., Fortney, J. J., Burrows, A. S., Ballester, G. E., Deming, D., Aigrain, S., Désert, J. .-.-M., Gibson, N. P., Henry, G. W., Knutson, H., Lecavelier des Etangs, A., Pont, F., Vidal-Madjar, A., Williamson, M. W., & Wilson, P. A. (2015). HST hot-Jupiter transmission spectral survey: detection of potassium in WASP-31b along with a cloud deck and Rayleigh scattering. MNRAS, *446*(3), arXiv 1410.7611, 2428–2443. https://doi.org/10.1093/mnras/stu2279

Sing, D. K. (2018). Observational Techniques With Transiting Exoplanetary Atmospheres. *arXiv e-prints*, arXiv 1804.07357, arXiv:1804.07357.

Sing, D. K., Fortney, J. J., Nikolov, N., Wakeford, H. R., Kataria, T., Evans, T. M., Aigrain, S., Ballester, G. E., Burrows, A. S., Deming, D., Désert, J.-M., Gibson, N. P., Henry, G. W., Huitson, C. M., Knutson, H. A., Lecavelier Des Etangs, A., Pont, F., Showman, A. P., Vidal-Madjar, A., . . . Wilson, P. A. (2016). A continuum from clear to cloudy hot-Jupiter exoplanets without primordial water depletion. Nature, *529*(7584), arXiv 1512.04341, 59–62. https://doi.org/10.1038/nature16068

Skilling, J. (2004). Nested Sampling (R. Fischer, R. Preuss, & U. V. Toussaint, Eds.). In R. Fischer, R. Preuss, & U. V. Toussaint (Eds.), *American institute of physics conference series*. https://doi.org/10.1063/1.1835238

Snellen, I., Albrecht, S., Anglada-Escude, G., Baraffe, I., Baudoz, P., Benz, W., Beuzit, J.-L., Biller, B., Birkby, J., Boccaletti, A., van Boekel, R., de Boer, J., Brogi, M., Buchhave, L., Carone, L., Claire, M., Claudi, R., Demory, B.-O., Desert, J.-M., . . . de Visser, P. (2019). ESA Voyage 2050 White Paper: Detecting life outside our solar system with a large high-contrast-imaging mission. *arXiv e-prints*, arXiv 1908.01803, arXiv:1908.01803.

Snellen, I., de Kok, R., Birkby, J. L., Brandl, B., Brogi, M., Keller, C., Kenworthy, M., Schwarz, H., & Stuik, R. (2015). Combining high-dispersion spectroscopy with high contrast imaging: Probing rocky planets around our nearest neighbors. A&A, *576*arXiv 1503.01136, A59. https://doi.org/10.1051/0004-6361/201425018

Stassun, K. G., Collins, K. A., & Gaudi, B. S. (2017). Accurate Empirical Radii and Masses of Planets and Their Host Stars with Gaia Parallaxes. AJ, *153*(3), arXiv 1609.04389, 136. https://doi.org/10.3847/1538-3881/aa5df3

Steinrueck, M. E., Parmentier, V., Showman, A. P., Lothringer, J. D., & Lupu, R. E. (2019). The Effect of 3D Transport-induced Disequilibrium Carbon Chemistry on the Atmospheric Structure, Phase Curves, and Emission Spectra of Hot Jupiter HD 189733b. ApJ, *880*(1), arXiv 1808.02011, 14. https://doi.org/10.3847/1538-4357/ab2598

Stevenson, K. B., Lewis, N. K., Bean, J. L., Beichman, C., Fraine, J., Kilpatrick, B. M., Krick, J. E., Lothringer, J. D., Mandell, A. M., Valenti, J. A., Agol, E., Angerhausen, D., Barstow, J. K., Birkmann, S. M., Burrows, A., Charbonneau, D., Cowan, N. B., Crouzet, N., Cubillos, P. E., . . . Wakeford, H. R. (2016). Transiting Exoplanet Studies and Community Targets for JWST's Early Release Science Program. PASP, *128*(967), arXiv 1602.08389, 094401. https://doi.org/10.1088/1538-3873/128/967/094401

Tennyson, J., & Yurchenko, S. N. (2012). ExoMol: molecular line lists for exoplanet and other atmospheres. MNRAS, *425*(1), arXiv 1204.0124, 21–33. https://doi.org/10.1111/j.1365-2966.2012.21440.x

Tennyson, J., Yurchenko, S. N., Al-Refaie, A. F., Barton, E. J., Chubb, K. L., Coles, P. A., Diamantopoulou, S., Gorman, M. N., Hill, C., Lam, A. Z., Lodi, L., McKemmish, L. K., Na, Y., Owens, A., Polyansky, O. L., Rivlin, T., Sousa-Silva, C., Underwood, D. S., Yachmenev, A., & Zak, E. (2016). The ExoMol database: molecular line lists for exoplanet and other hot atmospheres. *J. Mol. Spectrosc.*, *327*, 73–94. https://doi.org/10.1016/j.jms.2016.05.002

Tinetti, G., Drossart, P., Eccleston, P., Hartogh, P., Heske, A., Leconte, J., Micela, G., Ollivier, M., Pilbratt, G., Puig, L., Turrini, D., Vandenbussche, B., Wolkenberg, P., Beaulieu, J.-P., Buchave, L. A., Ferus, M., Griffin, M., Guedel, M., Justtanont, K., . . . Zwart, F. (2018). A chemical survey of exoplanets with ARIEL. *Experimental Astronomy*, *46*(1), 135–209. https://doi.org/10.1007/s10686-018-9598-x

Trotta, R. (2008). Bayes in the sky: Bayesian inference and model selection in cosmology. *Contemporary Physics*, *49*(2), arXiv 0803.4089, 71–104. https://doi.org/10.1080/00107510802066753

Tsiaras, A., Waldmann, I. P., Tinetti, G., Tennyson, J., & Yurchenko, S. N. (2019). Water vapour in the atmosphere of the habitable-zone eight-Earth-mass planet K2-18 b. *Nature Astronomy*, *3*arXiv 1909.05218, 1086–1091. https://doi.org/10.1038/s41550-019-0878-9

Tsiaras, A., Waldmann, I. P., Zingales, T., Rocchetto, M., Morello, G., Damiano, M., Karpouzas, K., Tinetti, G., McKemmish, L. K., Tennyson, J., & Yurchenko, S. N. (2018). A Population Study of Gaseous Exoplanets. AJ, *155*(4), arXiv 1704.05413, 156. https://doi.org/10.3847/1538-3881/aaaf75

Wakeford, H. R., Stevenson, K. B., Lewis, N. K., Sing, D. K., López-Morales, M., Marley, M., Kataria, T., Mandell, A., Ballester, G. E., Barstow, J., Ben-Jaffel, L., Bourrier, V., Buchhave, L. A., Ehrenreich, D., Evans, T., García Muñoz, A., Henry, G., Knutson, H., Lavvas, P., . . . Sanz-Forcada, J. (2017a). HST PanCET program: A Cloudy Atmosphere for the Promising JWST Target WASP-101b. ApJ, *835*(1), arXiv 1701.00843, L12. https://doi.org/10.3847/2041-8213/835/1/L12

Wakeford, H. R., Sing, D. K., Deming, D., Lewis, N. K., Goyal, J., Wilson, T. J., Barstow, J., Kataria, T., Drummond, B., Evans, T. M., Carter, A. L., Nikolov, N., Knutson, H. A., Ballester, G. E., & Mand ell, A. M. (2018). The Complete Transmission Spectrum of WASP-39b with a Precise Water Constraint. AJ, *155*(1), arXiv 1711.10529, 29. https://doi.org/10.3847/1538-3881/aa9e4e

Wakeford, H. R., Sing, D. K., Kataria, T., Deming, D., Nikolov, N., Lopez, E. D., Tremblin, P., Amundsen, D. S., Lewis, N. K., Mandell, A. M., Fortney, J. J., Knutson, H., Benneke, B., & Evans, T. M. (2017b). HAT-P-26b: A Neptune-mass exoplanet with a well-constrained heavy element abundance. *Science*, *356*(6338), arXiv 1705.04354, 628–631. https://doi.org/10.1126/science.aah4668

Waldmann, I. P., Tinetti, G., Rocchetto, M., Barton, E. J., Yurchenko, S. N., & Tennyson, J. (2015). Tau-REx I: A Next Generation Retrieval Code for Exoplanetary Atmospheres. ApJ, *802*(2), arXiv 1409.2312, 107. https://doi.org/10.1088/0004-637X/802/2/107

Webster, C. R., Mahaffy, P. R., Atreya, S. K., Moores, J. E., Flesch, G. J., Malespin, C., McKay, C. P., Martinez, G., Smith, C. L., Martin-Torres, J., Gomez-Elvira, J., Zorzano, M.-P., Wong, M. H., Trainer, M. G., Steele, A., Archer, D., Sutter, B., Coll, P. J., Freissinet, C., . . . Vasavada, A. R. (2018). Background levels of methane in Mars' atmosphere show

strong seasonal variations. *Science*, *360*(6393), 1093–1096. https://doi.org/10.1126/science.aaq0131

Welbanks, L., Madhusudhan, N., Allard, N. F., Hubeny, I., Spiegelman, F., & Leininger, T. (2019). MassMetallicity Trends in Transiting Exoplanets from Atmospheric Abundances of H_2O, Na, and K. ApJ, *887*(1), arXiv 1912.04904, L20. https://doi.org/10.3847/2041-8213/ab5a89

Wende, S., Reiners, A., Seifahrt, A., & Bernath, P. F. (2010). Crires spectroscopy and empirical line-by-line identification of feh molecular absorption in an m dwarf. *A&A*, *523*, A58. https://doi.org/10.1051/0004-6361/201015220

Woitke, P., Helling, C., Hunter, G. H., Millard, J. D., Turner, G. E., Worters, M., Blecic, J., & Stock, J. W. (2018). Equilibrium chemistry down to 100 K. Impact of silicates and phyllosilicates on the carbon to oxygen ratio. A&A, *614*arXiv 1712.01010, A1. https://doi.org/10.1051/0004-6361/201732193

Wong, I., Knutson, H. A., Kataria, T., Lewis, N. K., Burrows, A., Fortney, J. J., Schwartz, J., Shporer, A., Agol, E., Cowan, N. B., Deming, D., Désert, J.-M., Fulton, B. J., Howard, A. W., Langton, J., Laughlin, G., Showman, A. P., & Todorov, K. (2016). 3.6 and 4.5 μm Spitzer Phase Curves of the Highly Irradiated Hot Jupiters WASP-19b and HAT-P-7b. ApJ, *823*(2), arXiv 1512.09342, 122. https://doi.org/10.3847/0004-637X/823/2/122

Young, A. T. (1973). Are the Clouds of Venus Sulfuric Acid? Icarus, *18*(4), 564–582. https://doi.org/10.1016/0019-1035(73)90059-6

Yousefi, M., Bernath, P. F., Hodges, J., & Masseron, T. (2018). A new line list for the $A^2\Sigma^+ - X^2\Pi$ electronic transition of OH. *J. Quant. Spectrosc. Radiat. Transf.*, *217*, 416–424. https://doi.org/10.1016/j.jqsrt.2018.06.016

Yurchenko, S. N., Amundsen, D. S., Tennyson, J., & Waldmann, I. P. (2017). A hybrid line list for CH_4 and hot methane continuum. *A&A*, *605*, A95. https://doi.org/10.1051/0004-6361/201731026